Low Platinum Loading Electrospun Electrodes for Proton Exchange Membrane Fuel Cells

by

Simcha Lev Singer

B.S., Mechanical Engineering (2004)
Northwestern University

SUBMITTED TO THE DEPARTMENT OF MECHANICAL ENGINEERING
IN PARTIAL FULFILLMENT OF THE REQUIREMENTS FOR THE DEGREE OF

MASTER OF SCIENCE IN MECHANICAL ENGINEERING
AT THE
MASSACHUSETTS INSTITUTE OF TECHNOLOGY

September 2006

Signature of Author: .....
.....
Department of Mechanical Engineering
August 11, 2006

Certified by: .....
.....
Yang Shao-Horn
Assistant Professor of Mechanical Engineering
Thesis Supervisor

Accepted by: .....
.....
.....
Lallit Anand
Professor of Mechanical Engineering
Chairman, Department Graduate Committee

Low Platinum Loading Electrospun Electrodes for Proton Exchange Membrane Fuel

by

Simcha Lev Singer

Submitted to the Department of Mechanical Engineering
on August 11, 2006 in Partial Fulfillment of the
Requirements for the Degree of Master of Science in
Mechanical Engineering

ABSTRACT

An experimental study was performed to evaluate the utility of electrospun carbon nanofiber supports for sputtered platinum catalyst in proton exchange membrane fuel cells. The performance of the sputtered nanofiber supports was similar to that of sputtered commercial gas diffusion layers in single cell fuel cell tests. However, sputtered platinum electrodes performed significantly worse than commercial thin film electrodes due to high activation and concentration voltage losses.

Cyclic voltammetry and rotating disc electrode experiments were performed in order to evaluate the influence of platinum loading and particle size on the electrochemical active area and oxygen reduction performance of the sputtered platinum. Active area per weight catalyst decreased with sputtering time, and the oxygen reduction activity slightly increases with increasing sputtering time. Both of these effects are thought to be due to increasing platinum particle size as sputtering time is increased.

Thesis Supervisor: Yang Shao-Horn
Title: Assistant Professor of Mechanical Engineering

Acknowledgements

The author would like to thank the Office of Naval Research for funding this project.

I would like to thank Prof. Shao-Horn for her guidance, for the opportunity, and for securing funding for this research.

I would also like to thank J.P. Kurpiewski for training me with the electrospinning apparatus and the rotating disc electrode technique.

I would like to thank all the members of the Electrochemical Energy Lab for their help with various testing equipment, as well as Kurt Broderick for help with the sputtering, Patrick Boisvert for help with EDAX and gaseous mode imaging in the SEM, and Dr. Anthony Garratt-Reed for imaging one sample with the JEOL 2010 TEM.

Table of Contents

List of Figures

1. Introduction

1.1 Motivation

The production and availability of energy is a key issue facing the U.S. and the world in the 21st century. Crude oil and gasoline prices have risen sharply since 2004, increasing from around $34 per barrel of light sweet crude to over $70 per barrel in August 2006 [1]. This has been caused by increasing demand from developing countries and supply constraints caused by inadequate investment as well as supply disruptions (natural and political). Figure 1 plots the historic and projected energy consumption in the U.S. in quadrillion Btu, which reveals that the transportation sector is the largest consumer of energy.

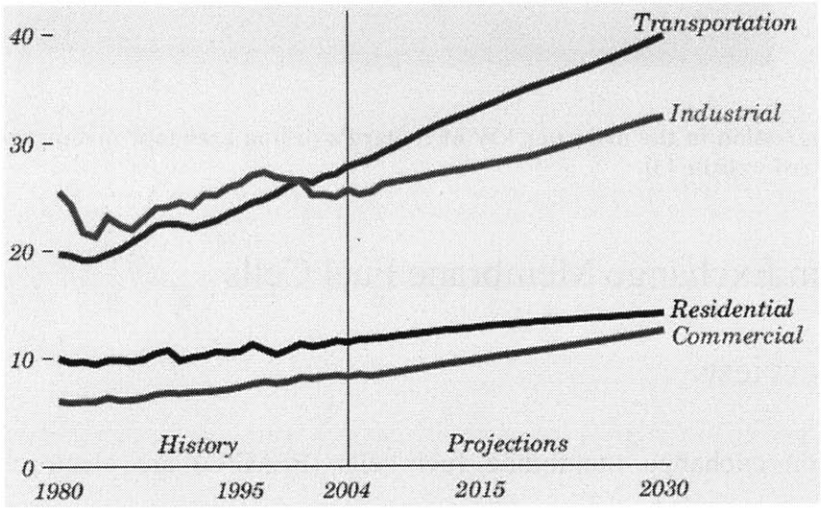

Figure 1. Delivered energy consumption by sector (quadrillion Btu) 1980-2030 [2].

With the rise in gasoline prices, hybrids and more fuel efficient vehicles have been gaining market share, and there has been an increased interest in fuel cells as a potential long term competitor for energy conversion in transportation and other industries. To be competitive in the marketplace, fuel cells must compete with the

internal combustion engine. To this end, the Department of Energy has set a goal for transportation oriented fuel cells of $30 per kW by the year 2010. Ballard Power Systems, a leader in proton exchange membrane fuel cells, reports PEMFC costs of $73/kW in 2005, and Figure 2 shows the price progression since 2002 [3].

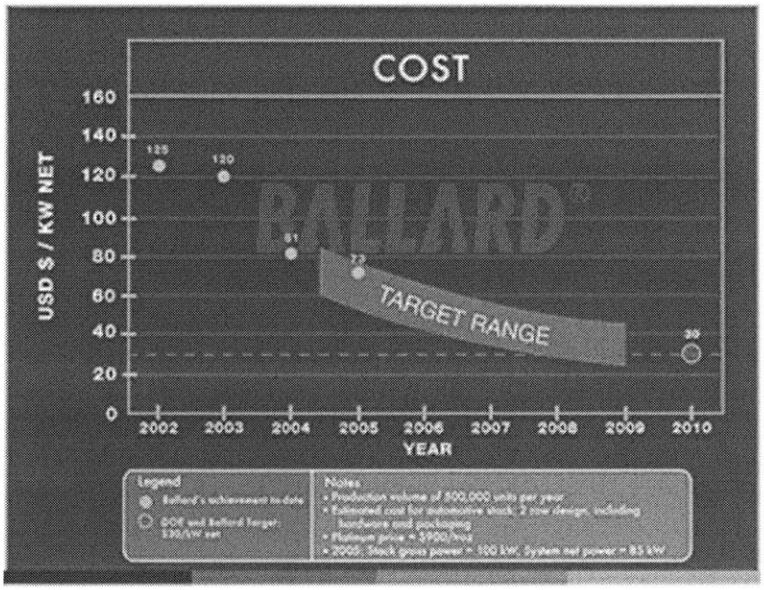

Figure 2. Progression in the price per kW of Ballard's proton exchange membrane fuel cells, taken from the Ballard website [3].

1.2 Proton Exchange Membrane Fuel Cells

1.2.1 Overview

Proton exchange membrane fuel cells (PEMFC) are electrochemical energy conversion devices that convert chemical energy directly to electrical energy. They were first developed in the 1960s, but research on PEMFCs has greatly accelerated since the late 1980s when new fabrication methods allowed for a significant reduction in their cost [4]. PEMFCs derive their name from the electrolyte, which is a solid proton conducting polymer, the most popular of which is Nafion™, which is manufactured by Dupont®.

PEMFCs are attractive power sources for applications ranging from mobile electronics to combined heat and power generation, due to their scalability from several watts to hundreds of kilowatts [5]. They are especially attractive for transportation applications, due to their high power density, quick start-up time and low operating temperatures. PEMFCs offer a high efficiency, low emissions alternative to fossil fuels. They are quiet, simple and have no moving parts. However, they are still relatively expensive and durability is a major concern. Additionally, obtaining and distributing the required hydrogen fuel on a large scale may be the greatest hurdle to commercialization that PEMFCs face.

The heart of a PEMFC is the membrane electrode assembly (MEA), which consists of the two electrodes, the anode where hydrogen is fed, and the cathode where the oxidant is fed, bonded to either side of the proton conducting membrane. The electrodes typically consist of a catalyst layer and a supporting layer to distribute the reactant gases, called a gas diffusion layer (GDL). This "sandwich" of the GDLs, catalyst layers and membrane is then hot pressed in order to assemble the cell and to ensure intimate contact between the platinum reaction sites and the proton conducting membrane. The whole MEA is then sandwiched between the bipolar plates, which serve as current collectors and contain flow channels for the distribution of the reactant gases. It is possible to stack several membrane electrode assemblies in electrical series in order to increase the cell's voltage. A schematic of a single cell PEMFC is shown in Figure 3.

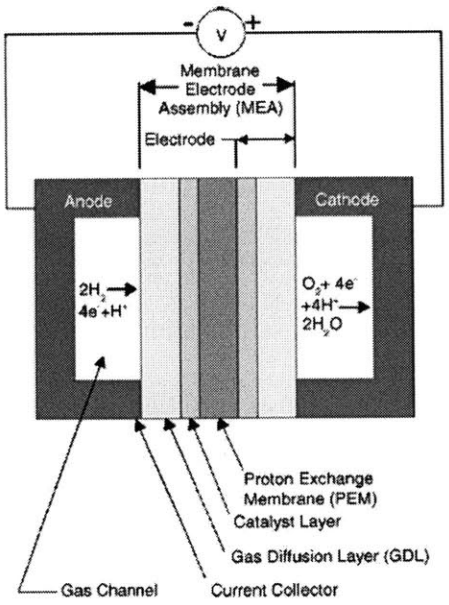

Figure 3. PEMFC schematic showing the MEA and the current collectors [4].

The catalyst layer of both the anode and cathode is typically made of conducting carbon particles on the order of 50 nm that are decorated with platinum catalyst particles roughly 3 nm in diameter. These platinum-decorated carbon particles are mixed with a Nafion ionomer solution as a binding material, and this slurry is then applied to either the gas diffusion layers or to both sides of the membrane. Figure 4 shows a schematic of an idealized catalyst layer.

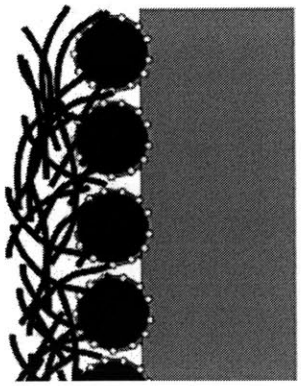

Figure 4. Schematic of a catalyst layer. Black is carbon support, gray is ionomer and white is platinum catalyst particles [5].

1.2.2 Basic PEMFC Operation

The overall reaction in a PEM fuel cell combines hydrogen and oxygen to form water. There is no combustion and no formation of CO_2. At the anode hydrogen is oxidized to protons according to:

$$2H_2 \rightarrow 4H^+ + 4e^-. \quad (1.1)$$

The thermodynamic potential of this half reaction is 0 V vs. the normal hydrogen electrode (NHE) [6]. At the cathode, oxygen is reduced to water according to:

$$O_2 + 4e^- + 4H^+ \rightarrow 2H_2O, \quad (1.2)$$

which has a standard electrode potential of 1.229 V vs. NHE at room temperature and pressure [7]. Thus the overall cell reaction is:

$$2H_2 + O_2 \rightarrow 2H_2O, \quad (1.3)$$

and the theoretical cell voltage at open circuit and at standard temperature and pressure is 1.229 V.

While the thermodynamic voltage of a PEMFC is 1.229 V, the actual voltage during cell operation is significantly less, and depends on several factors, especially the current density. This voltage loss is referred to as overpotential. There are three main overpotentials associated with PEM fuel cells: activation, ohmic, and concentration. Activation overpotentials are caused by the finite reaction rates of the hydrogen oxidation and oxygen reduction reactions, and cause the largest voltage losses. Ohmic overpotentials are caused by the electrical resistance in the cell outside the membrane, and the ionic resistance to proton flow of the membrane and ionomer solution. Concentration overpotentials are due to limited reactant gas supply at the reaction sites and become prominent at high current densities. A typical polarization curve showing

hydrogen/air fuel cell performance and the overpotentials at different current densities is shown in Figure 5.

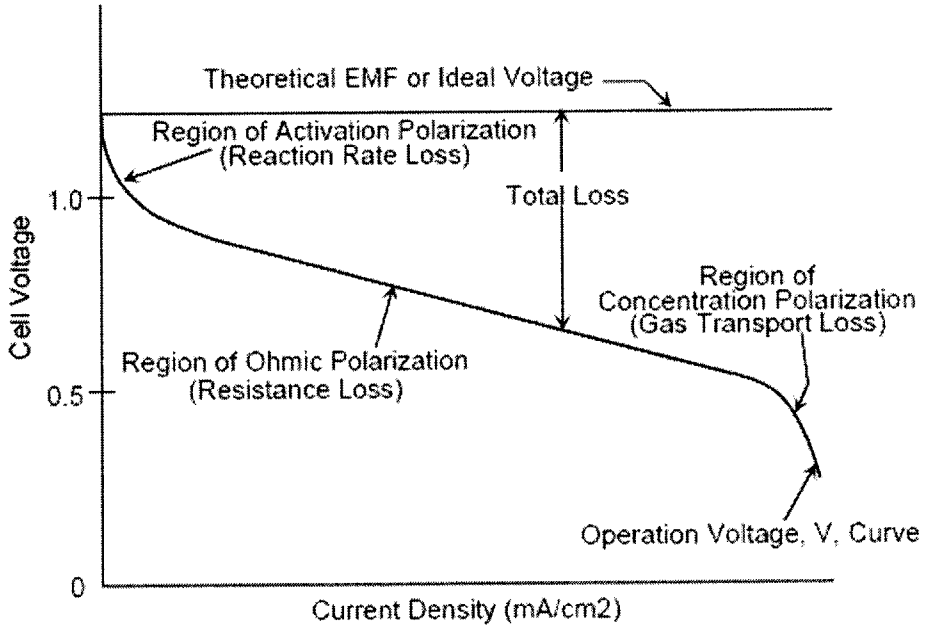

Figure 5. Typical polarization curve showing the various overpotentials [8].

The reduction of oxygen is a much slower reaction than the oxidation of hydrogen, and thus most of the research in PEMFC electrodes is concentrated on the cathode. In fact, the exchange current density, i_0, which measures the bidirectional current at equilibrium, is estimated to be $\sim 10^{-9}$ A/cm^2_{Pt} for the oxygen reduction reaction on platinum, roughly six orders of magnitude slower than the i_0 for hydrogen oxidation on platinum [9], [10]. Because hydrogen oxidation is so much faster than oxygen reduction, it is assumed in most analyses that the entire activation overpotential is due to the cathode reaction. Since the oxygen reduction reaction (ORR) is the cause of so much voltage loss in PEMFCs, the search for more active, better structured, and cheaper cathodes is a very active research area.

In a similar vein, the concentration overpotential of the anode is also assumed to be negligible when using pure hydrogen on the anode and air on the cathode [11]. This is due to the fact that hydrogen is a significantly smaller molecule than oxygen, and oxygen only makes up roughly one-fifth of the molecules in an air feed, while the hydrogen feed is typically pure.

The ohmic loss originates mainly from the resistance to proton motion within the membrane and the ionomer in the catalyst layer. Additionally, there is a contribution from the electronic resistance of the catalyst layer, the gas diffusion media, the bipolar plates and all contact resistances. These are typically small, however, when compared to the resistance to proton transport through the membrane [12]. In recent years, the ohmic losses of PEMFCs have been significantly reduced as membrane technology has improved and membrane thickness has decreased from 75 μm to 25 μm. Nonetheless, membrane research is quite active, since the proton conductivity of Nafion is very sensitive to its relative humidity, and this is what limits the operating temperature of PEMFCs.

1.3 Electrospinning

Electrospinning is a method of producing continuous, one dimensional nanostructures that has gained in popularity and versatility in recent years. The electrospinning process utilizes a syringe pump to slowly pump a high molecular weight solution, usually a polymer, through a nozzle, and a high voltage power supply is connected between the nozzle and a grounded collector plate. The applied electric field induces uniformly distributed charges on the surface of the solution protruding from the

nozzle, and under the influence of the applied field and the charge repulsions, the drop forms a conical shape referred to as a Taylor cone [13]. When the external field is large enough to overcome the surface tension, a charged jet of solution issues from the Taylor cone and travels toward the grounded collector plate. The initially straight jet then experiences a whipping instability wherein the polymer is subjected to large shear forces as the jet is stretched and its diameter is drastically reduced by the rapid whipping motion and by the evaporation of the solvent [14]. When the fibers reach the collector plate most of the solvent has been evaporated and the result is a solidified mat of thin, randomly oriented fibers. A schematic of the electrospinning process is shown in Figure 6.

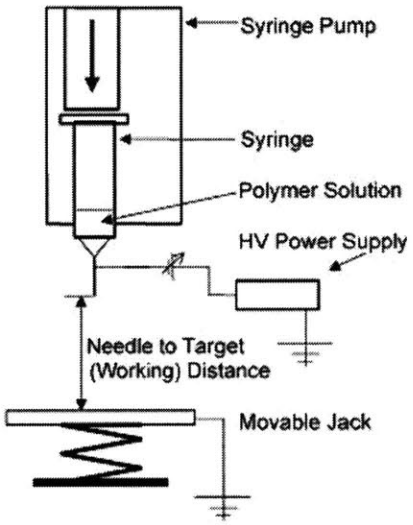

Figure 6. Schematic of the electrospinning setup [15].

There are many modifications that can be made to the electrospinning solution and/or equipment which can allow for the encapsulation of nanoparticles in the electrospun fibers, the formation of core and sheath fiber structures, and the formation of ceramic fibers using the sol-gel technique [16-20]. For applications such as filtration devices, catalyst support structures and electrode materials, the large surface area to

volume ratio and highly porous random orientation of electrospun fibers is desirable. Recently there have been demonstrations of a method of controlling the alignment of electrospun fibers as they are collected, which is important for the development of nanoscale electronic devices and is also advantageous for nanofiber reinforced composites [21,22]. Clearly, the electrospinning process is highly versatile and has many potential applications.

One of the many applications of electrospinning is the production of carbon nanofibers, which can then be used as supports for nanoparticles. Although carbon itself cannot be "spun," it is possible to carbonize various polymers through different heat treatments, including polyacrylonitrile (PAN). PAN is usually electrospun with N,N, dimethylformamide (DMF) as the spinning solvent. PAN has the chemical formula

$$CH_2\text{-}CH{\equiv}CN. \tag{1.4}$$

To form conducting carbon fibers from PAN, two heat treatments are required, which will be described in a later section.

1.4 Carbon Nanofiber Based Electrodes for Fuel Cells

Several works have investigated the use of carbon nanofibers as supports for catalyst particles in fuel cells [23] [24] [25]. Gangeri et al. used chemical vapor deposition to grow carbon nanofibers on felt and cloth carbon supports (GDLs), and then deposited platinum on these mats by the incipient wetness impregnation method [23]. The platinum particles' average diameter was 10 nm. The performance of these electrode (apparently used for the anodes only, although it is unclear) at room temperature and pressure (it is also not stated whether air or oxygen is fed to the cathode) achieves a

maximum power density of 22.72 mW/cm^2, and at 0.423 V, the current density is 10 mA/cm^2. The performance is compared to an MEA made from E-TEK electrodes as anode and cathode, which achieves a maximum current density of only 60 mA/cm^2, clearly far below its potential [23]. Bessel et al. used dispersed graphite nanofibers as supports for platinum particles and tested their methanol oxidation performance with cyclic voltammetry [24]. They concluded that 5% platinum on graphite nanofibers had an increase in methanol oxidation current of 400% when compared to 5% platinum on standard Vulcan carbon, and they attribute this to a decrease in catalyst decomposition for the platinum on the graphite nanofibers compared to the standard carbon support. Many studies use *dispersed* carbon nanotubes as supports for platinum catalysts because their surface areas are typically much larger than carbon nanofibers' [25]. A recent study has grown carbon nanotubes on carbon cloth substrates and then deposited platinum on the nanotubes by a sputtering method [26]. Using microwave assisted chemical vapor deposition, they were able to grow multi-walled carbon nanotubes with diameters of 20 nm, and by sputtering these supports for 30s, they were able to deposit platinum particles with a mean diameter of 2 nm. Using cyclic voltammetry, they concluded that the performance of the carbon cloth with nanotubes performs better than carbon cloth without nanotubes, but it is unclear whether the CVs are for samples with or without sputtered platinum, and no quantitative information is given.

1.5 Commercial Goals for PEMFC Cathodes

In order to drive the oxygen reduction reaction at the required rate, a significant amount of platinum catalyst is needed. Platinum is one of the most expensive precious metals (trading at roughly $1250 per ounce), and therefore it is necessary to minimize the amount of platinum used in PEM fuel cell electrodes. Typical anode and cathode loadings are currently 0.3-0.4 mg Pt/cm^2, and for an 85 kW fuel cell stack that would be needed to power a small car, this equates to 72-94 g Pt, or 0.85-1.1 g_{Pt}/kW [27]. The target set in a review paper by GM's fuel cell group, however, is to reduce the platinum specific power density to <0.2 g_{Pt}/kW at cell voltages $\geq$ 0.65 V. This goal can be achieved by:

(a) eliminating 50% of current mass-transport voltage losses (which they say they have been able to do at a research level by better water handling), and

(b) reducing anode loadings to 0.05 mg Pt/cm^2 without losing any performance, which has been shown experimentally [10], and

(c) reducing cathode loadings to 0.15 mg Pt/cm^2, while still maintaining power densities of ~0.9 W/cm^2 [27].

To realize (b) and (c) they say it will be necessary to implement Pt-alloy catalysts, which have a higher specific activity for oxygen reduction than pure Pt. Simply reducing the amount of platinum for MEAs that have no increase in concentration overpotential as Pt loading is reduced, will reduce the cell voltage as follows:

$$\frac{\partial E}{\partial \log Lca} = -b, \tag{1.5}$$

where E is cell voltage, L_{Ca} is the cathode loading and b is the Tafel slope, which is usually between 60 and 70 mV/decade of current density. So by reducing the platinum loading from 0.4 to 0.1 mg/cm^2, the cell's voltage would fall by 42 mV at all current densities, and would yield 0.22 g_{Pt}/kW at cell voltages of 0.65 V. However, this option is rejected because the power density would then be too low (0.68 W/cm^2), and they therefore conclude that in the future, Pt-alloy catalysts, which may have quadruple the mass activity, will be required on the cathode [27].

1.6 Sputter Deposition for PEMFC Cathodes

Several works have investigated sputter deposition of platinum catalyst on GDLs and on Nafion membranes as methods to decrease the platinum loading of PEM fuel cells. A study examining sputtered platinum films on ETEK-GDLs achieved maximum power densities of ~124 mW/cm^2 for loadings of 0.005 mg/cm^2 and 203 mW/cm^2 for loadings of 0.107 mg/cm^2, both on H_2/O_2 operation at ambient temperature and pressure, and using a GDL sputtered with a loading of 0.08 mg/cm^2, they achieved 500 mA/cm^2 at 0.4 V [28]. A little beyond ~0.1 mg/cm^2, they found that performance began to decrease due to the filling of the micropores in the microporous layer of the GDL [28]. Another study achieved 1000 mA/cm^2 at 0.4 V, giving a maximum power density of 400 mW/cm^2, by using a sputtered GDL with a loading of 0.08 mg/cm^2, also apparently with H_2/O_2 operation, although it is not stated explicitly [29]. Below 500 mA/cm^2 the performance was only slightly worse than an E-TEK electrode with a loading of 0.35 mg/cm^2, although the performance begins to diverge rapidly from the commercial electrode at higher current densities, which they speculate could be caused by blocked pores due to

sputtering. The platinum particles were thought to be roughly 3.5 nm sized clusters [29]. Another study compared sputtering platinum on GDLs versus sputtering on the membrane and concluded that sputtering on the GDL yielded superior performance, achieving 147 mA/cm^2 at 0.6 V for a loading of 0.084 mg/cm^2 using an H_2/air feed [30]. Doubling the loading to about 0.17 mg/cm^2 caused the performance to increase to about 250 mA/cm^2 at 0.6 V, but further increasing the loading up to 0.5 mg/cm^2 showed little effect. The fact that sputtered GDLs outperformed sputtered membranes could possibly be due to increased concentration losses when the platinum is in such intimate contact with the Nafion membrane. Groups have also attempted alternating layers of sputtered platinum and various inks comprised of Nafion ionomer and/or carbon particles with a slight increase in the performance compared to the equivalent single platinum layer [30], [31]. O'Hayre et al. sputtered 0.04 mg/cm^2 on both sides of a Nafion membrane and the cell's maximum power was 60% of that of a standard 0.4 mg/cm^2 MEA [32]. However, it seems that their setup was not optimal, given that the maximum power density of the standard 0.4 mg/cm^2 MEA was only 50 mW/cm^2. Much of the literature on sputtered MEAs performs the fuel cell testing at different temperatures, pressures and gas feeds, making comparisons between various works difficult. Table 1 summarizes these results.

Table 1. Summary of previous studies on sputtered platinum for PEMFCs

Support	Pt Loading [mg/cm^2]	Power@0.4V [mW/cm^2]	Oxidant Gas/Temp	Ref.
GDL	0.005	120	O_2 (20°C)	[28]
GDL	0.107	203	O_2 (20°C)	[28]
GDL	0.08	400	O_2? (20°C?)	[29]
GDL	0.084	144	Air (70°C)	[30]
GDL	0.5	230	Air (70°C)	[30]
Membrane	0.04	32	O_2 (20°C)	[32]

1.7 Platinum Performance as an ORR catalyst

Typical platinum particles in commercial fuel cell catalyst layers are around 2-4 nm in diameter and have electrochemical active areas between 60 and 120 m^2/g_{Pt} before being cycled during operation, after which they may agglomerate, which decreases the electrochemical active area [33]. Using rotating disc electrode measurements at 1600 rpm and at potentials of 0.9 V vs. RHE (the potential where it is standard practice to evaluate platinum's oxygen reduction activity), values for specific activity range from 240-320 $\mu A/cm^2_{Pt}$ in non-adsorbing perchloric acid electrolyte [27]. In sulfuric acid, specific activities are significantly lower due to the adsorption of anions that block catalytic sites. Generally, as the electrochemical active area increases, the mass activity (current per mass platinum) will increase. But as platinum particles size decreases and electrochemical active area increases, the specific activity is believed to decrease

(although there has been much discussion of this in the literature, summarized in [9]). This is what is referred to as the "particle size effect," describing the observation that increasing the electrochemical area by reducing particle size below ~3nm will not result in an increase in mass activity since the increasing electrochemical active area is offset by the decreasing specific activity.

In addition to the specific activity, platinum supported on carbon black is also characterized by its Tafel slope, which is the slope of the voltage vs. log current density curve. Tafel slopes at low overpotentials, whether measured in RDE (above 0.87 V vs. RHE) or in a fuel cell (at current densities below 100 mA/cm^2) are typically linear and have values at or near the theoretical value of 70 mV/decade (at 80°C). The Tafel slope is based on the Butler-Volmer equation of electrode kinetics:

$$i = i_o e^{-\alpha nF\eta / RT} - e^{(1-\alpha)nF\eta / RT} \quad (1.6)$$

The current density is i, i_o is the aforementioned exchange current density, α is the transfer coefficient which represents the symmetry of the activation barrier, n is the number of electrons transferred in the reaction step, η is the activation overpotential, R is the universal gas constant, T is the temperature in Kelvin, and F is Faraday's constant. When the activation overpotential, η, is large, this can be reformulated as:

$$\eta = -\frac{RT}{\alpha nF}\ln i_o + \frac{RT}{\alpha nF}\ln i. \quad (1.7)$$

When we replace the natural logarithm with log-based 10, we get an equation of the form:

$$\eta = a + b\log i \quad (1.8)$$

where the Tafel slope is given by [6]:

$$b=\frac{-2.3RT}{\alpha F}. \tag{1.9}$$

An experimental Tafel slope greater than the theoretical slope of ~70 mV/decade is indicative of concentration overpotential in the electrode layer, and this is a useful diagnostic tool [12], [34].

1.8 Thin Film RDE

The utility of the rotating disc electrode technique lies in the fact that by rotating the working electrode, the mass transport within the solution has been solved analytically. This allows one to modify the measured current density to account for mass transport effects, which gives what is termed the kinetic current density. The measured current, i, is related to the kinetic (i_k) and mass transport (diffusion), (i_d) limited current densities, according to the equation:

$$\frac{1}{i}=\frac{1}{i_k}+\frac{1}{i_d} \tag{1.10}$$

The Levich equation expresses the diffusion limited current as

$$i_d = 0.62nFD^{2/3}\nu^{-1/6}c_o\omega^{1/2} = B\omega^{1/2}, \tag{1.11}$$

where D is the diffusion coefficient of the reactant in the electrolyte, ν is the kinematic viscosity of the electrolyte and ω is the rotation rate in radians per second. All the terms in this equation are constant and ω is an experimental parameter. For 0.5 M H_2SO_4 at 25° C, the value of B is roughly 0.065 mA/cm^2 [35]. This equation assumes that the only mass transport loss is that associated with the electrolytic solution. If there are additional mass transport losses associated with the diffusion of reactant through the film used to

glue the electrode to the surface, then the above equation must be modified according to the following:

$$\frac{1}{i} = \frac{1}{i_k} + \frac{1}{i_d} + \frac{1}{i_f} \tag{1.12}$$

where i_f is the film diffusion limited current density. This i_f term can be neglected provided the Nafion film used as a glue to stick the catalyst to the rotating shaft is less than ~0.2-0.3 μm thick [35]. This has been satisfied for the samples tested in this work by using just 10 μL of a very dilute ionomer solution (see Section 2.4).

Based on the above assumption and using equations (1.10) and (1.11), plots of 1/i vs. $1/\omega^{1/2}$, called Koutecky-Levich plots, should yield straight lines with slopes equal to 1/B and y-intercepts equal to $1/i_k$.

1.9 Approach of This Work

In order to lower the cost of PEMFCs, a new fabrication technique for the electrodes based on electrospinning is being investigated. If one were able to simultaneously create the carbon support and the catalyst particles in such a way that the performance was on par with current wet chemistry platinum deposition methods (small Pt catalyst particles, good dispersion) it would be considerably cheaper and less time-consuming since it would be a continuous manufacturing process. Even without such a revolutionary approach, it may be beneficial to replace the current carbon black catalyst supports with a continuous web of carbon nanofibers in order to eliminate the possible electrical isolation of carbon particles, and to simplify the catalyst preparation process. Additionally, the different structure of catalyst layers based on carbon nanofiber mats

could possibly improve the performance of the fuel cell since the catalyst layer is no longer based on a dense mixture of carbon and ionomer (alternatively, it could diminish the performance).

In a previous work, electrospinning was carried out with a palladium metal salt (palladium acetate) in the spinning solution [36]. This was a quasi-one-step method (it had to be followed by two heat treatments) of producing the entire electrode (carbon support and catalyst particles). The palladium metal precipitated during the heat treatments, and the Pd nanoparticle diameters ranged from roughly 10 to 100nm, with average diameters always above 30 nm. Furthermore, when the particles were relatively small (<10nm), as they must be for catalysis purposes, they tended to be embedded within the carbon fibers, and when the particles were able to emerge to the surface of the roughly 200 nm fibers, they were almost always very large (>100nm) [36]. Another major obstacle to this method was the fact that electrospinning platinum salts (platinum chloride and platinum pentanedionate) proved to be extremely difficult, and palladium is not a suitable catalyst for the oxygen reduction reaction for PEMFCs.

Because of these two problems, we were unable to evaluate whether electrospinning was in fact suitable for fuel cell catalyst layers in the first place. To that end, this work aims to evaluate the feasibility of using electrospun carbon nanofiber supports for platinum catalyst particles in PEMFC applications. This was achieved by electrospinning plain PAN without a noble metal salt solution, carbonizing the fibers using heat treatments, and subsequently depositing the platinum catalyst by sputtering platinum on the surface of these carbon nanofibers. These catalyst layers were examined using electron microscopy and then tested electrochemically and compared to standard

supports with the same platinum deposition technique and amount. With this knowledge, we can then evaluate whether electrospinning passes the first test as a suitable method for manufacturing PEMFCs catalyst layers. We were also able to evaluate the sputtering process as a platinum deposition method for PEMFCs using the same electrochemical and electron microscopy methods.

2. Experimental

2.1 Electrospinning

Electrospinning solutions were prepared by dissolving polyacrylonitrile in N,N dimethylformamide. The typical weight percentage of PAN in the solution was between 8% and 10%. The PAN was dissolved in the DMF overnight while mixing on a magnetic stir plate (without heating). After the PAN appeared sufficiently dissolved (few chunks visible), it was placed in an oven at 80°C for roughly 15 minutes. Electrospinning was carried out using the setup shown in Figure 7.

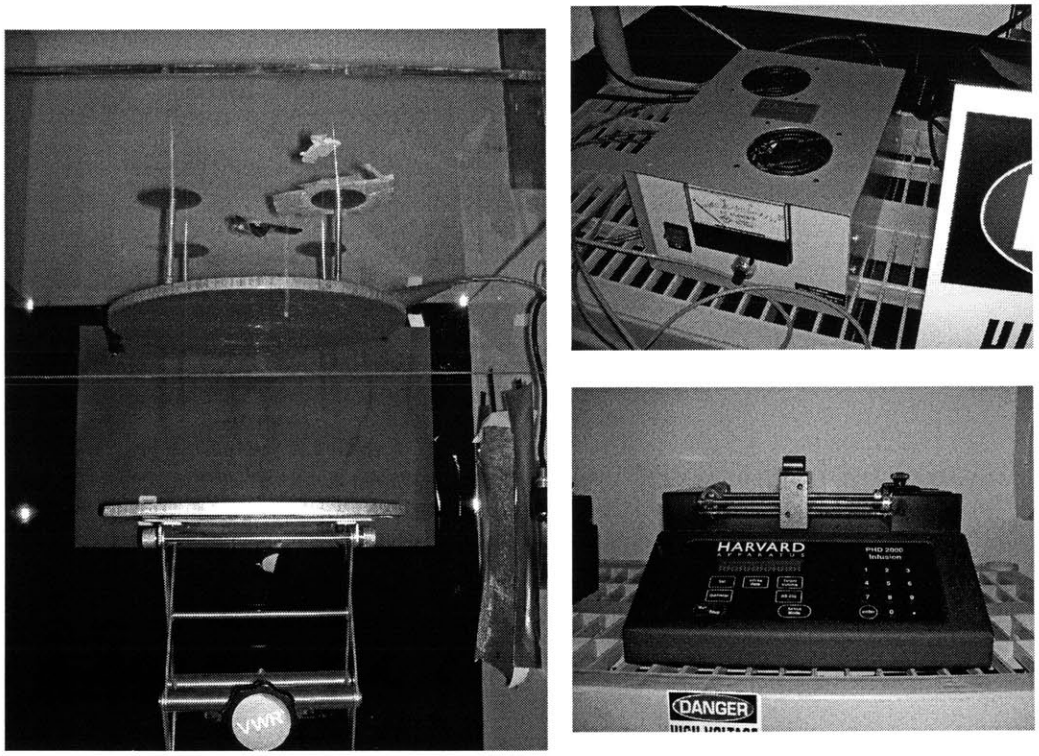

Figure 7. The electrospinning setup used in the EEL. The nozzle protrudes through the top plate, and the bottom collector plate is on an adjustable jack. The whole system is in a plexiglass enclosure with a local exhaust line. The high voltage power supply is shown on the top right and the infusion pump on the bottom right.

The polymer solution was placed in a 6 mL syringe and mounted in a Harvard Apparatus PhD 2000 Infusion pump. Teflon tubing carried the solution from the syringe to a nozzle protruding between two plates. The plate-to-plate distance was varied between 15 and 25 cm, and the nozzle typically protruded 5-6 cm from the top plate. The nozzle had an inner diameter of 0.040 inches. The pump was programmed to deliver solution at a flow rate of between 0.4 and 1.0 mL/hr. A high voltage, typically between 12-20 kV (depending on plate-to-plate distance) was applied between the top plate and the grounded lower plate. Nanofibers were collected on the bottom plate after spinning different amounts of solution. The resulting wet fiber mats were scraped off of non-stick aluminum foil covering the grounded collector plate and placed on a nickel mesh for the stabilization heat treatment.

All the carbon nanofiber samples tested electrochemically in this study were made from the same electrospinning solution and were spun on the same day. This run produced 16 samples, each spun from a volume of solution equal to 0.04 mL. The voltage used in the spinning was between 13.5 and 14.5 kV, and was chosen solely to maintain a stable jet without drops. The spinning solution used for these samples was 9.25% PAN by weight, and was mixed for 36 days. This mixing time was unusually long, and was unintentional. The flow rate was between 0.43 and 0.45 mL/hr. The plate to plate spacing was between 20 and 22 cm and the nozzle protruded from the upper plate approximately 5.5 cm. The diameter of the as-spun samples on the collector plate was always about 7 cm. Additionally, there were no problems removing the samples from the non-stick aluminum foil, and the entire thickness of the samples was removed (as opposed to just a top layer).

2.2 Heat Treatments

The first heat treatment is a stabilization step which oxidizes the PAN and stabilizes the polymer to allow for further heat treatments. The stabilization step occurred in a Fischer Scientific muffle oven in an air atmosphere and consisted of raising the temperature to 50°C at 3°C per minute and holding for two hours, bringing the temperature to 280°C at 1°C per minute and holding for two hours, and finally lowering the temperature to 35°C at 5°C per minute.

The carbonization step was performed in a Lindberg Blue/M tube furnace under argon flow. The furnace was first purged with argon for at least 20 minutes. The temperature was ramped to 900°C at a rate of 40°C per minute and was held at that temperature for 15 minutes. During the carbonization heat treatment it was necessary to have the samples covered with pieces of high-alumina ceramic sheets (0.04 inches thick), or else they would burn away. In fact, whatever area of the stabilized sample that protruded from the ceramic sheets was lost. The heat treatments were done several samples at a time, each sample being surrounded on top and bottom by a piece of ceramic.

2.3 RF Sputtering

Sputtering was performed in the Microsystems Technology Lab using an Argon flow of 60 sccm, a Pt target, and at a power of 100 W. Based on previous users' estimates, the RF sputtering chamber typically deposits 23 nm of Pt in 4 minutes, which is equivalent to ~0.05 mg Pt/cm^2 (or ~0.0125 mg Pt/cm^2 per minute) by using the density of Pt and assuming a continuous flat layer. Control experiments indicated that the

platinum deposition rate was 0.014 mg Pt/cm^2 per minute, close to the amount which was expected.

2.4 Rotating Disc Electrode Testing

Circular samples 5 mm in diameter were punched from the sputtered electrodes to use in RDE tests. A solution of 200:1 (by volume) of isoproponol: Nafion 5% was used as "glue" to stick the electrode to the glassy carbon disk. Typically, the nanofiber electrode was placed on the glassy carbon disk and 10 μL of this solution was pipetted on top of it. The solution would seep through and thus cause the nanofiber electrode to stick to the glassy carbon disk. Alternatively, sometimes it was beneficial to put ~2 of the 10 μL directly on the disk and then place the nanofiber electrode on top. Problems with static occurred frequently and often the electrodes would not stick to the disk. The electrochemical cell used for testing had five compartments. The working electrode protrudes into the cell from the top, while the reference electrode (saturated calomel) and the counter electrode (platinum wire) are inserted in side compartments. The other two compartments are for gas inlet and exit. The cell was filled with 0.5 M H_2SO_4, and was saturated with either oxygen or nitrogen. For the oxygen experiments, the working electrode was rotated using the Pine Instruments rotator. Data is collected, and potentials are applied using a bipotentiostat (also from Pine).

2.5 MEA Preparation

Membrane electrode assemblies for all samples were prepared using 2 mil (51 μm) thick Nafion 112 as the proton conducting membrane and E-TEK gas diffusion

electrodes with Pt loadings of 0.5 mg Pt/cm^2 as the anodes. The cathode was the only component that was changed between the different experiments, and there were three different variations: Pt-sputtered electrospun layers on top of E-TEK gas diffusion layers, Pt-sputtered gas diffusion layers, and one standard E-TEK gas diffusion electrode with a Pt loading of 0.5 mg Pt/cm^2 (the same electrode that was used for the anodes). Silicon gaskets on either side (10 mil thick) were used to prevent reactant gas leakage. The gas diffusion electrode, gas diffusion layer and electrospun layer were all punched with a 12 mm diameter circular punch (area of 1.13 cm^2) and this circle was used as the active area. The silicon gaskets were cut to a 3 inch by 3 inch square to fit the graphite bipolar plates, and were also punched, to leave a square with a circle in the middle. The punch was used to ensure that the holes in the gaskets lined up with each other, and that the anode and cathode were the same size, directly across from each other and not covered by the gasket. This method allows us to know precisely, and to utilize, the full active area. 30 μL of Nafion 5% solution, corresponding to 1.35 mg Nafion/cm^2, was added on the catalyst sides of the anode GDE, while for the electrospun membrane/GDL combinations, different amounts were attempted and tested. For all the results mentioned in this study, the cathodes contained 15 μL of Nafion 5% solution (0.67 mg Nafion/cm^2), since this amount seemed to work the best, and has been suggested elsewhere as the loading that maximizes the electrochemical active area [37]. The electrodes were dried for several hours in the drying oven at 50°C. The MEAs were then assembled and hot pressed in a hydraulic press for 4.5 minutes at a pressure of ~444 psi and a temperature of ~145°C. Like the amount of Nafion ionomer that was added to the electrodes, the pressure and time of hot-pressing were also varied until an effectual value was found. The

temperature was chosen to be close to, but not above, the glass transition temperature of Nafion (~150 °C) in order for the ionomer to flow and form good contact with the platinum while avoiding the degradation that would occur above the glass transition temperature [38]. Upon removal from the press, the MEA was inserted between the graphite bipolar plates and the fuel cell was connected to the test station.

2.6 Fuel Cell Testing

Fuel cell testing was performed with a University Model Fuel Cell Testing Station from Fuel Cell Technologies, Inc. Because the resolution of that instrument was only 14 mA, the load was supplied by battery testers; Solartron Analytical 1470s running the Cell Test software. Data was collected using constant current holds of four minutes in length, with the data points (voltage) coming from the average of the last minute. The experiments were run until the voltage fell below 0.1 V. Solartron 1260 Impedance/Gain Phase Analyzers were used to collect impedance data. Before an I-V curve was attempted, a large range frequency sweep with DC perturbation of 10mV was performed in order to gage at which frequency the response was purely resistive (ie. to determine at which frequency the high frequency intercept occurred). An AC signal at this frequency was then applied at each current in order to determine the high frequency resistance, or the ohmic losses due to electrolyte and electronic resistance outside the electrode layer. The high frequency method, like current interrupt, is unable to detect resistances that are in parallel to capacitances, such as those that exist within the electrode structure [39].

The Fuel Cell Testing Station was used to control the cell temperature, the reactant gas flow rates, the relative humidity, and the pressure (no pressurization was

used in general) using LabView software. Pure hydrogen was fed to the anode and either pure oxygen or air was fed to the cathode. At current densities below 400 mA/cm^2, the flow rates were fixed at the minimum that the mass flow controllers could control accurately (12 ccm hydrogen and 23 ccm oxygen or air). Above 400 mA/cm^2, the flow was stoichiometric, with hydrogen at 33% utilization, pure oxygen at 5% utilization, and oxygen in air at 25% utilization. However, the mass flow controllers with this equipment were not very accurate and the flow tended to fluctuate within $\pm$ 5-10 ccm of the set value.

The cell temperature for all tests was 80°C. Humidification was achieved using water bubblers, which were not very accurate and would often cause flooding problems in our fuel cells. The humidification bottles were set at 75°C, and the reactant preheaters were set at 85°C in order to attempt to evaporate any liquid water coming from the bubblers [12]. Thus the relative humidity of the cell was nearly 100%.

To perform hydrogen crossover measurements, the anode side was fed hydrogen, as usual, and the cathode side was given a nitrogen feed. Then the potential was swept, at 4 mV/s, from 0.1 to 0.5 V vs. the anode (which approximates an RHE). Cells with significant hydrogen crossover problems were not used.

The fuel cell setup, with the connection between the battery tester and the fuel cell station, is shown in Figure 8.

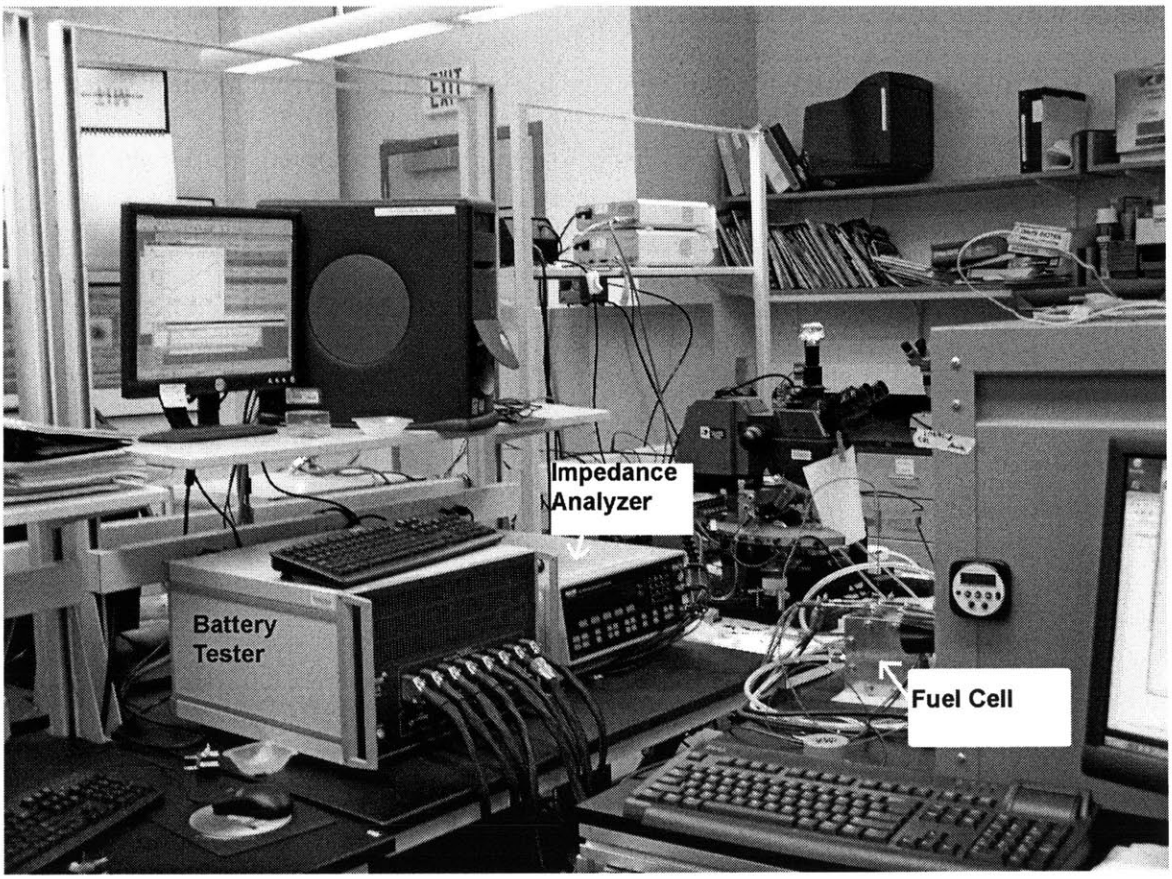

Figure 8. Fuel cell testing setup in the EEL showing the FC test station, the battery testers with impedance analyzers and the fuel cell itself.

2.7 Scanning Electron Microscopy

In order to determine the carbon nanofibers' size and the degree of spindling, SEM was performed using the FEI/Philips XL30 FEG Environmental SEM located in the Center for Materials Science and Engineering's Shared Experimental Facility. Energy dispersive spectroscopy was also used with the SEM in order to examine the cross-sectional distribution of platinum within an assembled MEA. For typical SEM use, a small amount of the sample was placed on double-sided carbon tape and loaded onto the

sample stub. For cross-sectional views a 90° stub was used. For images of the sputtered platinum distribution within the nanofibers, the backscattering electron detector was used. The sample was first hardened in resin overnight, microtomed using an MT-X Ultramicrotome, collected on a copper grid and then placed on an SEM stub with carbon tape. This eliminated edge effects as a possible source of brightness differences. For the cross-sectional images of the MEA, the microscope was operated in wet mode, and EDAX energy dispersive spectroscopy was used to obtain elemental analysis.

2.8 Transmission Electron Microscopy

In order to examine the platinum particle sizes for the various sputtering times, transmission electron microscopy was used. TEM was also performed in the Center for Materials Science and Engineering's Shared Experimental Facility, using a JEOL 200CX machine operating at 200kV. To prepare samples for TEM, a small amount of sample was cut and placed partially covering the hole of Ted Pella copper film. This allowed the fibers on the edges of the sample to be imaged, since the cutting procedure caused the fibers on the edge to be exposed and separated from the bulk, which had too many layers and was thus too thick to be imaged in TEM [36]. The film was developed in a dark room and scanned into a computer while making certain to keep the scale of the images correct. For the sample sputtered for 45 s, TEM was also performed by Dr.Anthony Garrett-Reed of the CMSE using a JEOL 2010 at 200 kV.

3. Electrospinning and Characterization

3.1 Electrospinning

During electrospinning, the large external field charges the drop of polymer solution protruding from the nozzle. This charging is due to ionic polarization of the solution [40]. The combination of the applied external field and the surface charge repulsions form the drop into a conical shape called a Taylor cone [13]. Once the external electric field is large enough to overcome the surface tension, a straight jet shoots from the Taylor cone. The jet then experiences a bending instability which causes a rapid whipping process, which elongates the fiber and reduces its diameter. As this is occurring, the solvent (DMF in this case) evaporates, further thinning the jet, and finally leaving a solidified mat of fibers on the collector plate.

During the electrospinning process there are three competing forces: surface tension tends to decrease the surface area of the jet and form beads and spindles, surface charge repulsions tend to increase the jet's surface area and reduce beading and spindling, and viscoelastic forces tend to reduce sudden changes in the jet's shape, and thus resist the formation of beads and spindles. On this theoretical basis, it is possible to determine the effect that changing certain experimental parameters will have on electrospun fibers. Since increasing the polymer concentration increases the solution's viscosity, it will reduce the spindling in the fibers [41]. However, it also will produce thicker fibers, since there is more solute present. Increasing the ionic conductivity of the solution by adding some type of salt has the double benefit of reducing the fiber diameter and reducing spindling, both of which are due to the increased charge repulsions on the jet's surface

[40]. Increasing the charge carried by the solution increases the current carried from the needle to the collector plate, and the fiber diameter is thought to scale with current to the $-2/3^{rd}$ power [42]. Increasing the flow rate of the solution will increase the fiber diameters simply because there is more material present in the jet, and theoretically, the fiber diameter scales with flow rate to the $2/3^{rd}$ power [42]. There is no consensus on what effect, if any, the applied voltage has on the fiber morphology [43]. From my experience, there is no noticeable effect, and the voltage is chosen simply to maintain a stable jet and whipping instability.

The goal of electrospinning was to spin fibers that were roughly equal to, or less than, 200 nm in diameter, while at the same time free of spindles. Some of the main parameters that affected the fiber morphology were the concentration of PAN in the spinning solution, the flow rate and the plate to plate distance (the nozzle protruded from the plate by a fixed 5.5 cm). The reason the plate to plate (or, nozzle to plate) distance may effect the fibers is because there is thought to be a terminal jet radius, beyond which the fiber does not thin any further [42]. If the collector plate is placed at a distance before the terminal radius has been achieved, the fibers will not be as thin as possible.

In the previous work in this lab, although there was a significant amount of salt in the spinning solution, mixtures of 9% PAN produced diameters that were between ~300 and 500 nm [36]. Unlike that previous work, there was no palladium acetate or any other compound that dissociates to ions in the spinning solution, and thus the current flowing in the jet was inherently smaller. Therefore, an effort was made to modify the other parameters affecting fiber diameter. The flow rate was decreased (from roughly 0.7 to 0.45 mL/hr), since this has a large effect (theoretically) on the fiber diameter, and the

plate to plate distance was increased from 17cm to roughly >20cm. The spinning nozzle was also replaced with a nozzle that was half the size (0.04 vs. 0.08 inches inner diameter). This may have the positive effect of reducing the size of the Taylor cone, and thus reducing the amount of solution flowing in the jet.

Table 2 shows the nine attempts at spinning plain PAN fibers and summarizes the results. The last two attempts were deemed successful and no more electrospinning was performed, since there were enough electrospun fibers from the last run for all the electrochemical testing.

Table 2. Electrospinning runs with key parameters and summary of results.

Date	% PAN in DMF	Flow Rate [mL/hr]	Voltage [kV]	Plate-to-plate dis [cm]	Results and fiber size after carbonization
11/1	8.5	0.55	16	23-25	Could not remove from foil
11/8	8.5	0.6-0.7	11-13	15-23	Difficult removing from foil; spindles
11/14	9				Unspinnable
11/17	9.5	0.55-0.6	12	17	Large spindles
11/29	8.5	0.55-0.57	11.6-12	18	400 nm fibers
12/1	9	0.5	12-14	21,23	250 nm fibers
12/13	9.5	0.42, 0.45	14-15	20,21,23	Large spindles
12/14	9	0.42-0.55	11.8,14.3	21,18	Fibers <200nm, few or no spindles
1/17	9.25	0.43-0.45	13.5-14.5	20,22	Fibers <200nm, few or no spindles

3.2 SEM Results

Figure 9 shows electrospun fibers that were spun from 9% PAN and that are spindle free with average diameters less than or equal to 200 nm. The low flow rate and

increased plate to plate distance may have been the key factors in achieving these goals, which can be seen in Table 2 above.

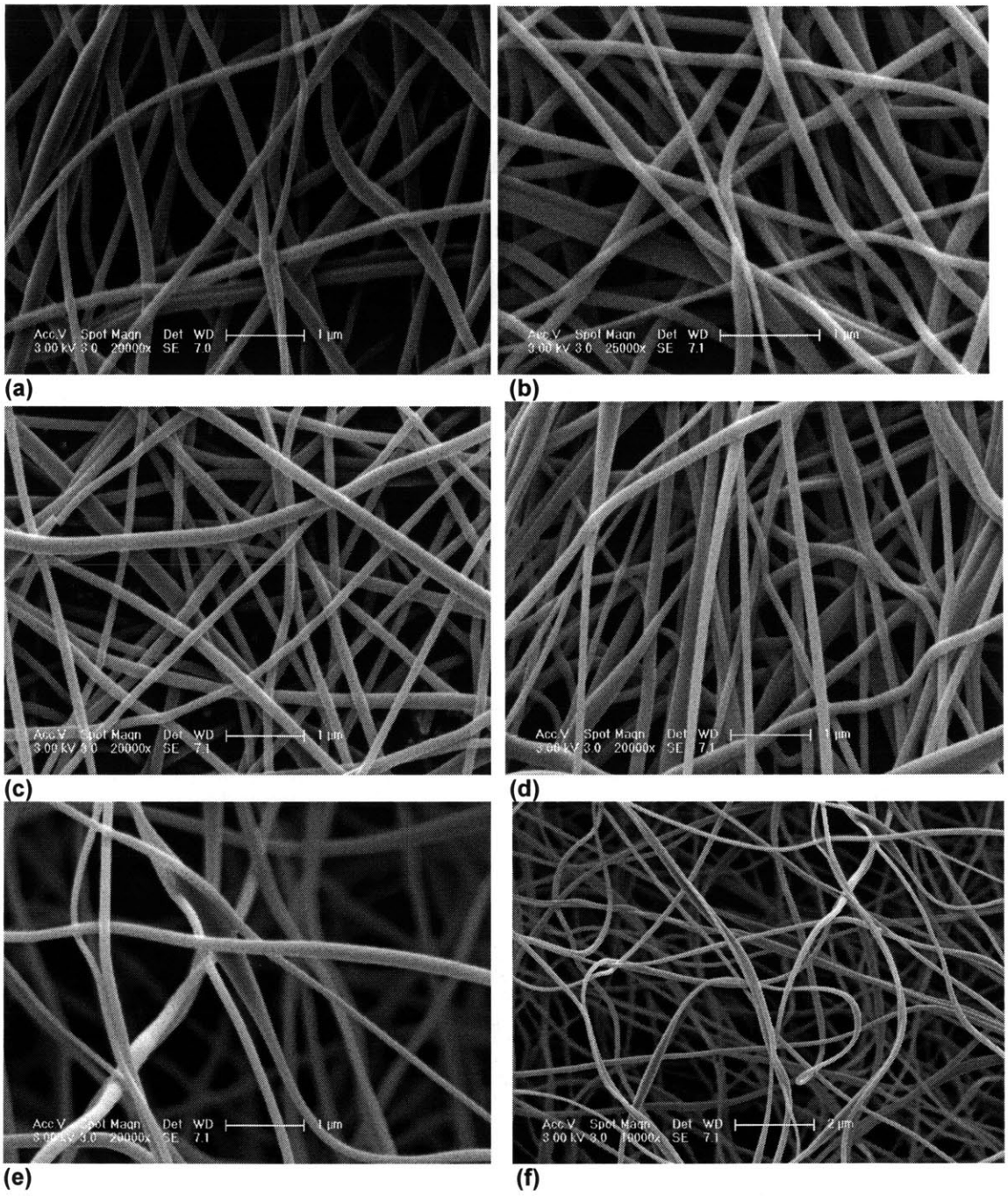

Figure 9. SEM images of runs from a solution of 9% PAN in DMF after carbonization heat treatment at (a) 14.3 kV, 0.42 mL/hr, 21 cm plate to plate distance (b) 14.3 kV, 0.55 mL/hr, 21 cm plate to plate distance (c) 14.3 kV, 0.55 mL/hr, 21 cm plate to plate distance (d) 11.8 kV, 0.47 mL/hr, 18 cm plate to plate distance, (e) and (f) 11.8 kV, 0.44 mL/hr, 18 cm plate to plate distance

Scale bars 1 μm, except in (f) it is 2 μm

Figure 10 shows high magnification images of electrospun fibers that were spun from 9.25% PAN and that are spindle free with average diameters less than or equal to 200 nm. Like the samples spun from 9% PAN, the low flow rate and larger plate to plate distance may have been key factors in obtaining small fiber diameters.

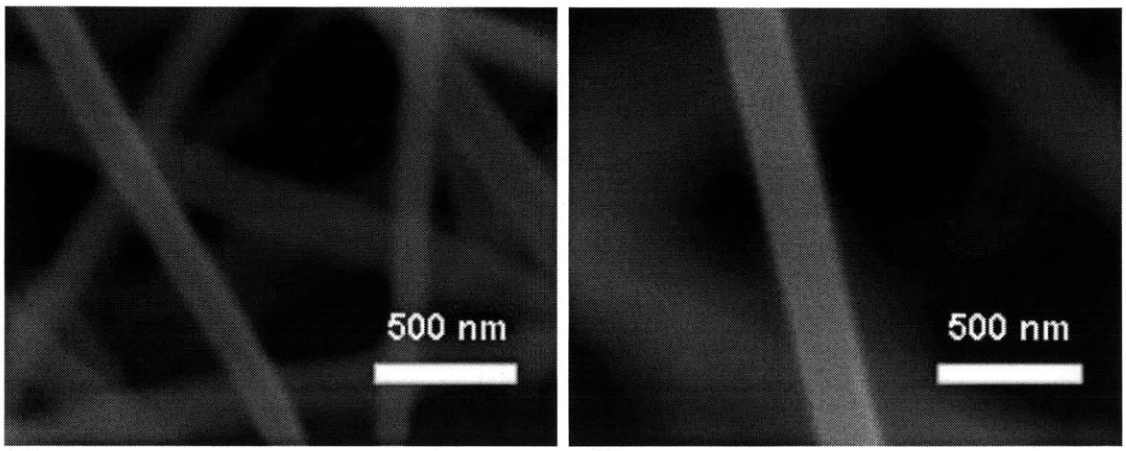

(a) (b)

Figure 10. SEM images, after carbonization, of runs from a solution of 9.25% PAN in DMF (a) 14.5 kV, 0.5 mL/hr, 21 cm plate to plate distance (b) 13.5 kV, 0.43 mL/hr, 21 cm plate to plate distance.

Figure 11 shows the samples spun from 9.25% PAN at lower magnification. It is clear that the samples are nearly spindle-free, despite the small fiber diameters.

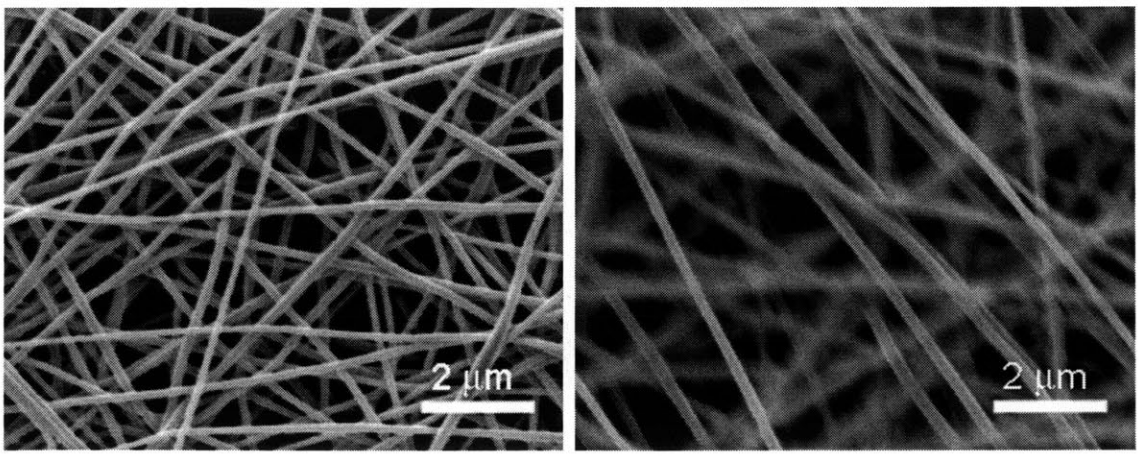

(a) (b)

Figure 11. SEM images, after carbonization, of runs from a solution of 9.25% PAN in DMF (a) 14.5 kV, 0.5 mL/hr, 21 cm plate to plate distance (b) 13.5 kV, 0.43 mL/hr, 21 cm plate to plate distance. Lower magnification shows the absence of spindling that is often associated with thin PAN fibers.

Figure 12(a) shows an SEM image of fibers spun with 9.5% PAN and a flow rate of 0.55 mL/hr. Despite the high PAN concentration the fibers show spindling, and despite the relatively high flow rate and PAN concentration, the fibers are quite *thin*. This illustrates the fact that electrospinning is by no means totally predictable, and that there are several unknown factors that may affect the results.

Figure 12(b) shows fibers from an 8.5% PAN solution spun with the same flow rate and plate to plate distance. These show no spindles, but are around 400 nm in diameter; much *thicker*, and again contrary to theory.

Finally, Figure 12(c) shows fibers spun from a 9% PAN solution with a flow rate of 0.5 mL/hr and increased plate to plate distance. It seems that although the concentration slightly increased from Figure 12(b), the fiber diameter decreased to ~250nm, possibly due to the increased plate to plate distance and the decreased flow rate.

These three examples illustrate the fact that lower polymer concentrations do not always, in practice, lead to reduced fiber diameters and the elimination of spindling. Another point to be made is that increasing the plate to plate distance from 18 to 21 cm may have been the key point in reducing the fiber diameter that is evident between Figures 12(b) and 12(c) below.

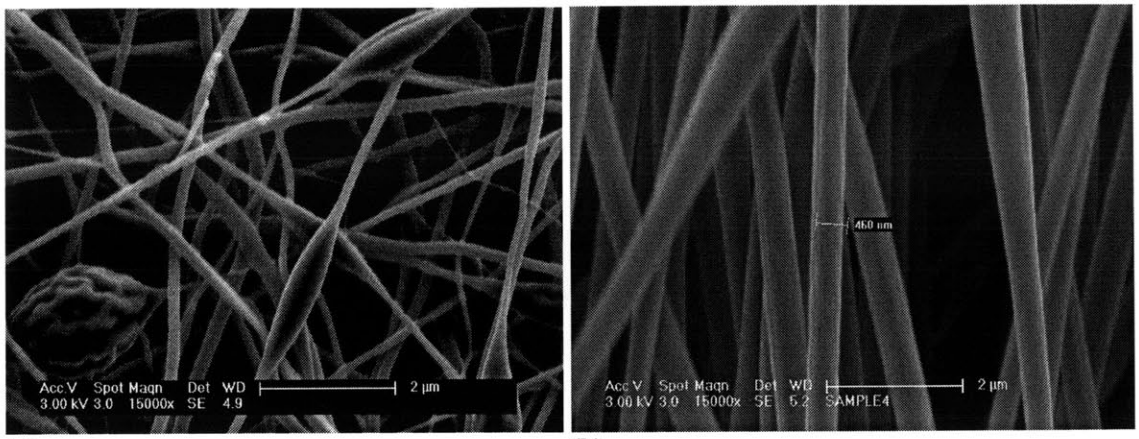

(a) (b)

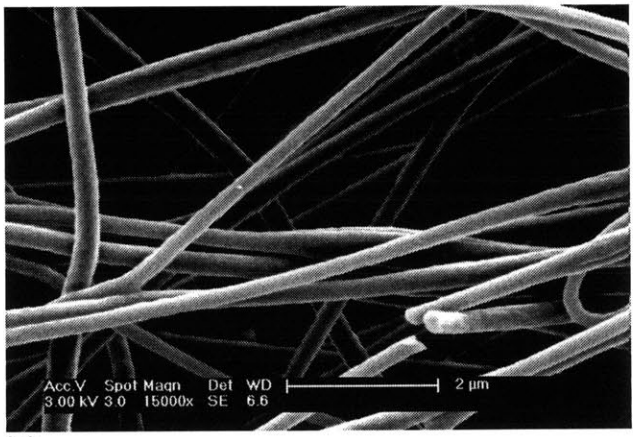

(c)

Figure 12. SEM images of (a) Spindled fibers from 11/17 (9.5% PAN), (b) 400 nm fibers from 11/29 (8.5% PAN), (c) 250 nm avg. diameter fibers from 12/1 (9%PAN)

Cross-sectional SEM was performed in order to examine the thickness of the electrospun layers. An image is shown below in Figure 13. It can be seen that the thickness in some places is less than 10 µm, while in other places, it is above 15 µm. Typical thicknesses were observed to be 15 µm, and the amount of polymer solution electrospun was the same for all the samples tested.

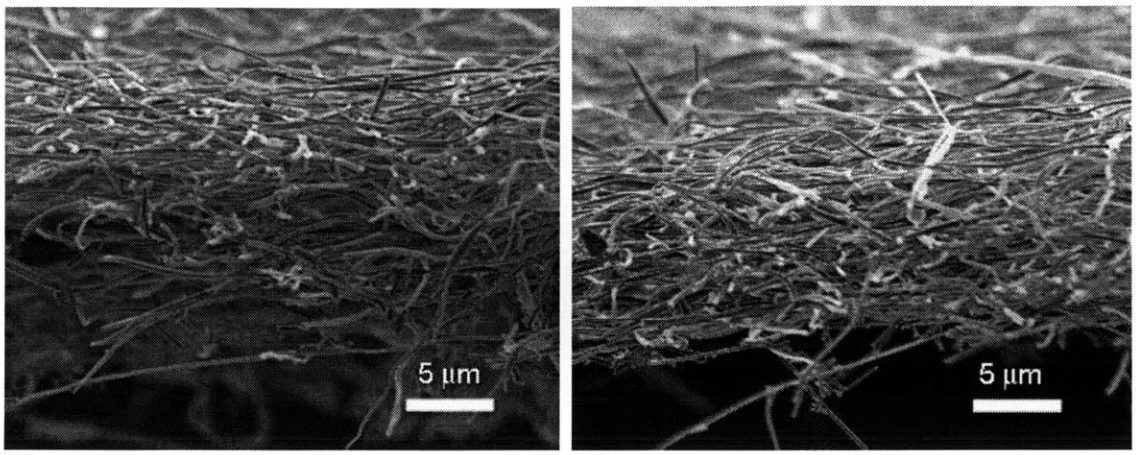

(a) (b)

Figure 13. Cross sectional SEM images of a sample spun from 0.04 mL of spinning solution and used for sputtering. The cross-sectional thickness varies along the mat in (a) 9-15 µm and is constant in (b) at roughly 15µm.

After sputtering the fibers appeared the same in the SEM images, except that the area that had been sputtered appeared brighter than the plain carbon fibers. In order to get an idea of how deeply the sputtered platinum penetrated into the electrospun layer, cross-sectional SEM was performed on a sample set in resin and microtomed, as explained in the experimental section. Microtoming made certain that there were no height variations in the sample and that any brightness differences could not be attributed to edge effects. Additionally, the backscattered electron detector was used, in order to highlight elemental differences, since higher molecular weight elements (platinum) appear much brighter than lower molecular weight elements (carbon) when using the backscattered electron detector. Figure 14 shows that the thickness of the electrospun layer is about 15 µm and that the sputtered platinum is located within roughly 2-3 µm from the surface. The vertical lines appearing in the images are due to microscope problems that particular day. Many previous papers reported platinum sputtering depths of roughly 100nm [44] [31] [30], with one reporting a tiny amount of platinum

penetrating up to 2 μm into the gas diffusion layer [29]. The higher penetration of platinum in the electrospun samples is likely due to their increased macro-porosity compared to typical gas diffusion layers.

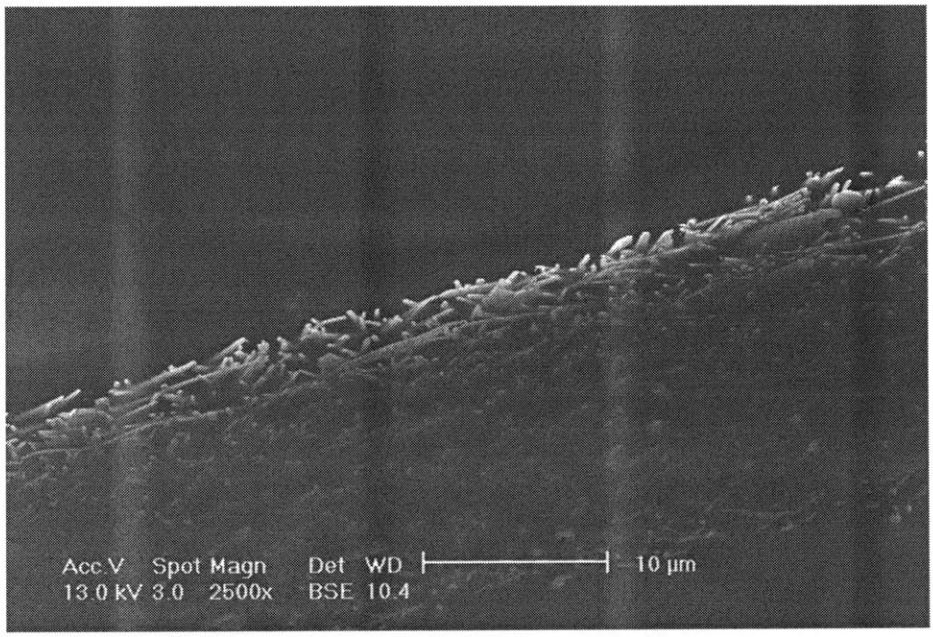

(a)

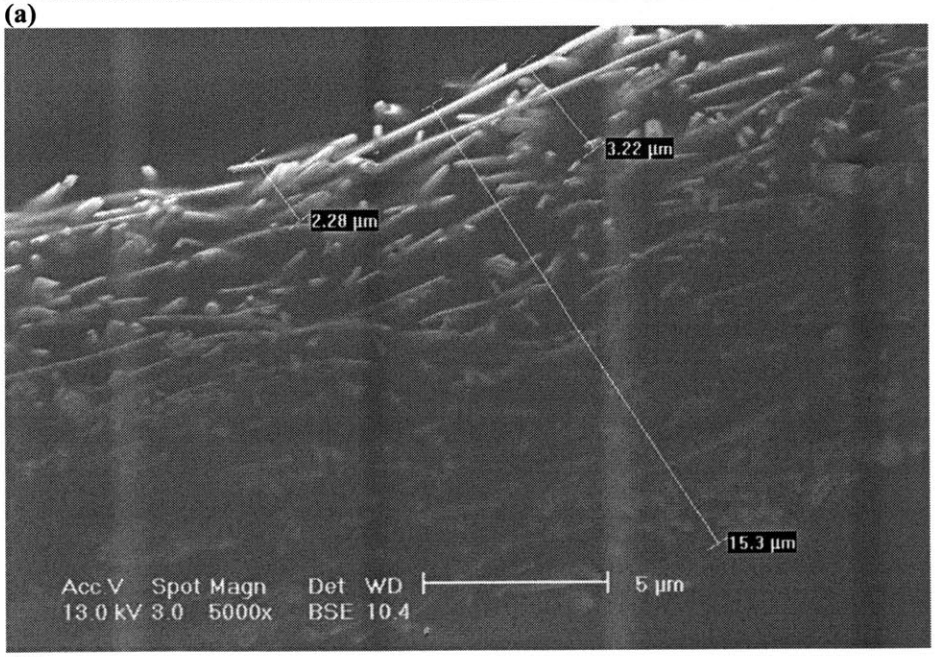

(b)

Figure 14. SEM images at (a) lower and (b) higher magnifications of the cross-section of a sputtered sample set in resin and microtomed. The bright area is the platinum.

Figure 15 shows SEM images of E-TEK 1400 LT gas diffusion layers with an ELAT microporous layer on top. Clearly, the surface area of the commercial gas diffusion layer with the carbon black microporous layer, thought to be made of carbon black, is greater than that of the smooth electrospun carbon fibers. A sample of electrospun fibers made specifically for surface area evaluation, had a surface area of 89.5 m^2/g as determined by BET (Brunauer, Emmett and Teller) surface area analysis (performed by Serkan Koc and Yang-Hyo Kim). In fact, typical carbon blacks can have 1000-2000 m^2/g, so electrospun carbon fibers have significantly less surface area [45].

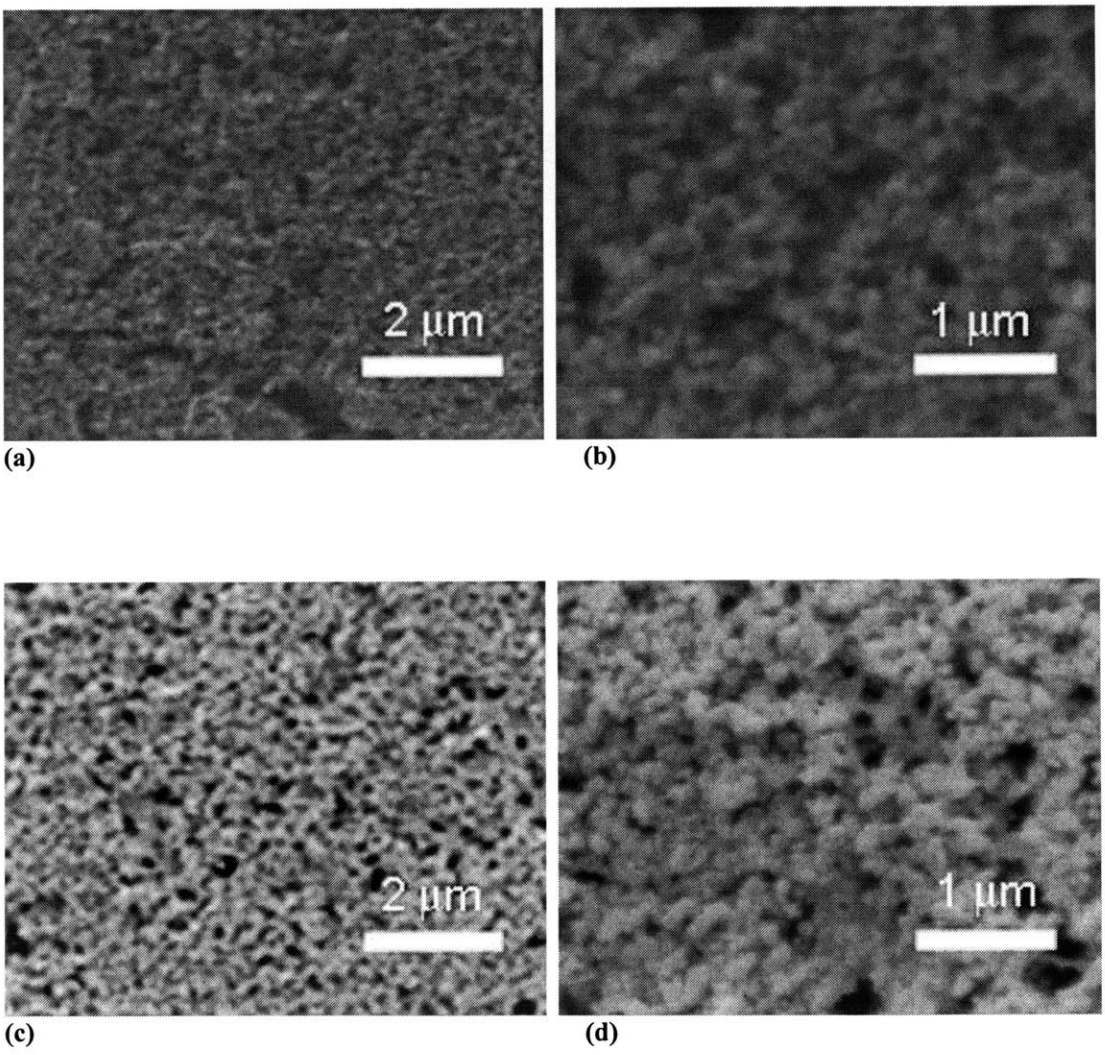

Figure 15. (a) and (b) plain GDL with microporous layer and (c) and (d) GDL with microporous layer sputtered with platinum

Using cross-sectional SEM in wet mode, it was possible to examine the structure of the assembled MEAs. The different layers are shown and labeled in Figure 16. The bright spots are probably due to variations in the height of the cross-section.

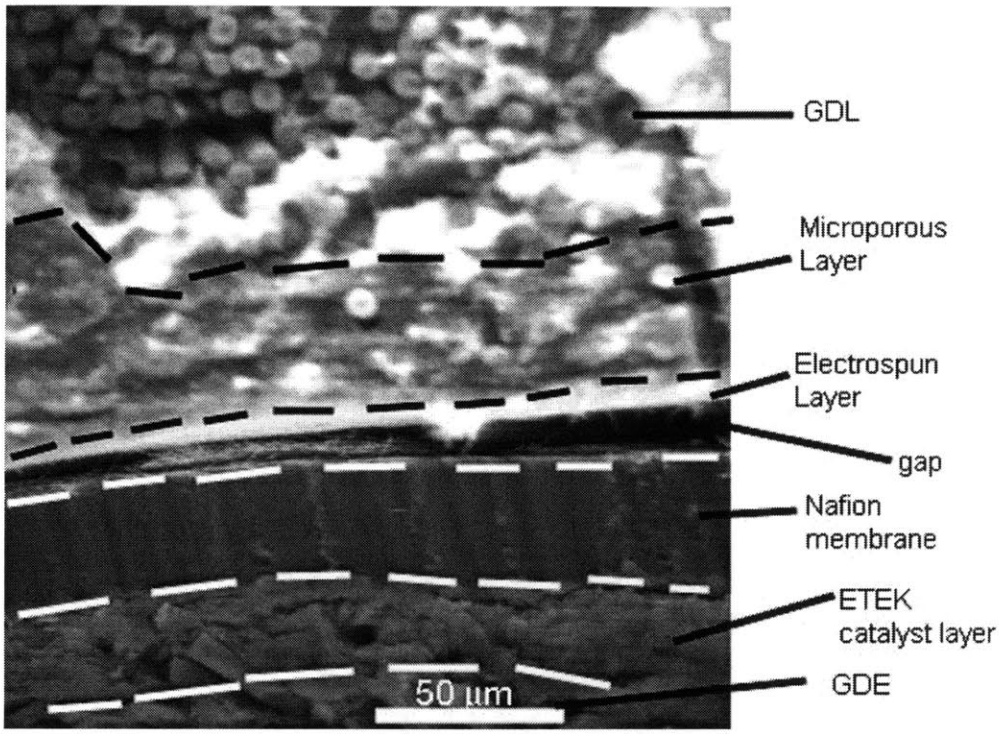

Figure 16. Cross sectional SEM image of an MEA, showing the various structures.

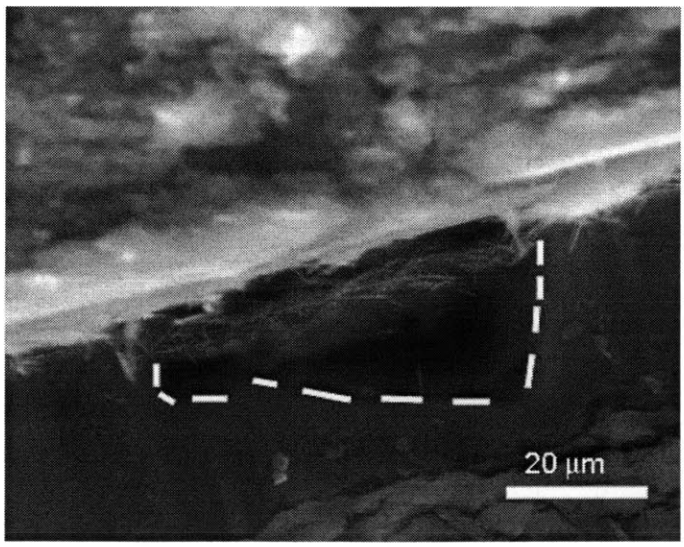

Figure 17. SEM image showing beam damage from charging, indicating that the damaged structure is the Nafion membrane.

The Nafion membrane is roughly 35-40 μm in thickness, and was identified by the beam damage it incurred (see the square in Figure 17 above).

Another important point of note is that for many parts of the examined cross-section, the electrospun layer was torn apart, with one small layer stuck to the Nafion membrane and the majority of it still attached to the microporous layer of the GDL. This is evident in Figure 18 below

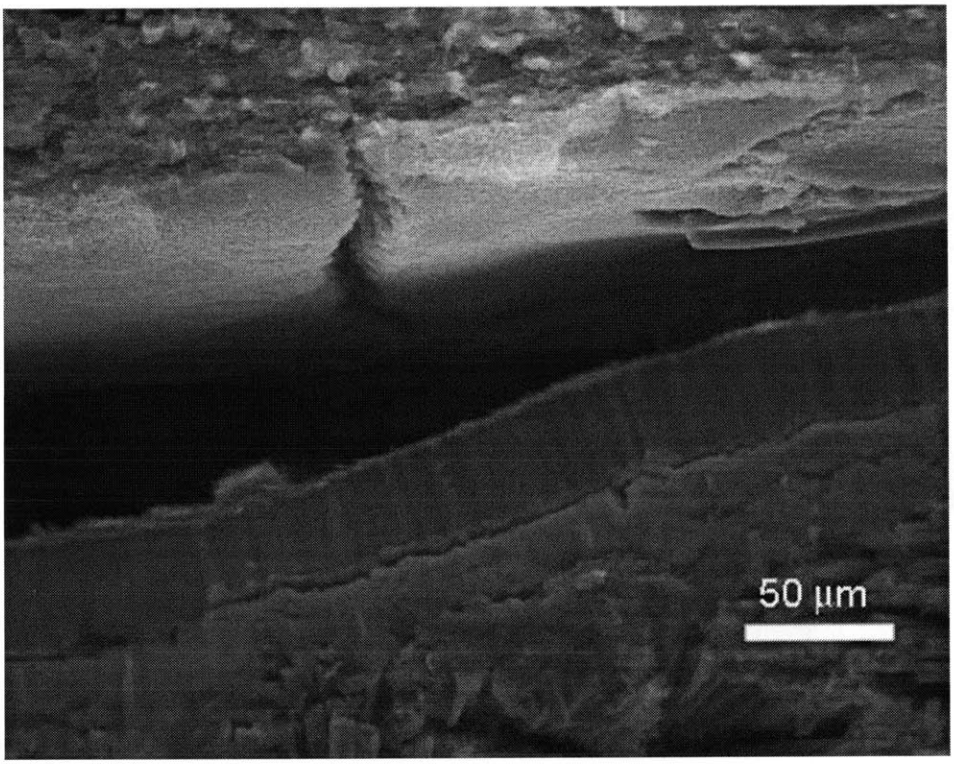

Figure 18. Cross-section SEM image of an MEA showing a gap between the membrane and electrospun layer.

To further verify that it was indeed two parts of the electrospun layer across an empty divide (the black area in the figures above), images were taken at increased magnification shown in Figure 19 below. While the two sides are in different focal

planes, it seems that the electrospun layer did, in fact, peel into two layers, with the majority staying connected to the GDL.

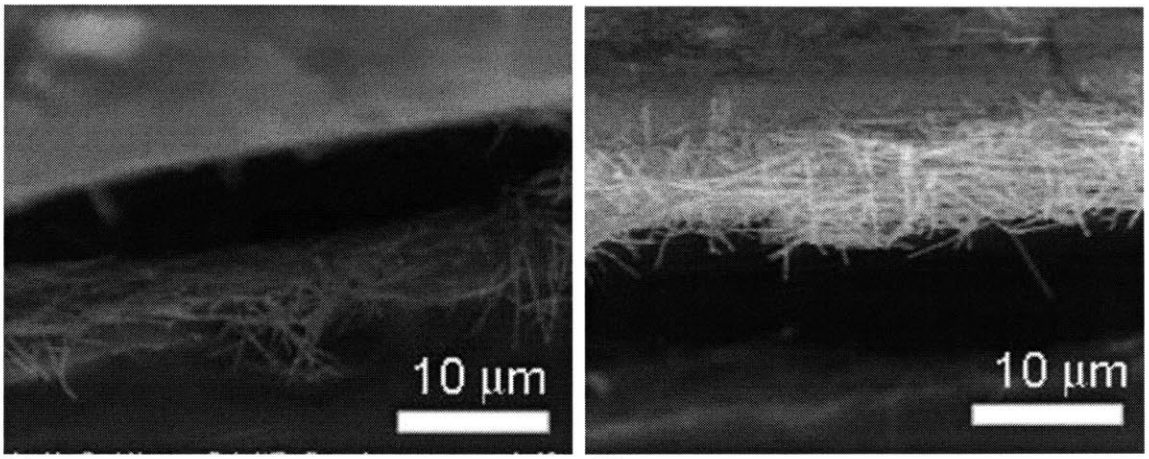

(a) (b)

Figure 19. Cross-section SEM images focused on (a) the GDL side, and (b) the membrane side, of the black divide, showing that a top layer of fibers was stuck on the membrane, while most of it remained with the GDL.

The E-TEK GDE, on the other hand, showed no signs of detaching from the membrane along the whole length of the MEA. This can perhaps be attributed to the fact that the GDE has a dense catalyst layer that is relatively homogeneously mixed with Nafion ionomer, where as the electrospun layer is thought to have most of its Nafion pooled at the bottom, on top of the GDL's microporous layer. This hypothesis was supported by energy dispersive spectroscopy scans.

Using the EDAX energy dispersive spectroscopy system in the environmental SEM, it was possible to obtain elemental line scans of the cross-sectional SEM images. Fluorine is found in the Nafion ionomer, and thus its presence indicates the presence of Nafion. One such line scan is shown below in Figure 20 and the corresponding elemental plot is shown in Figure 21.

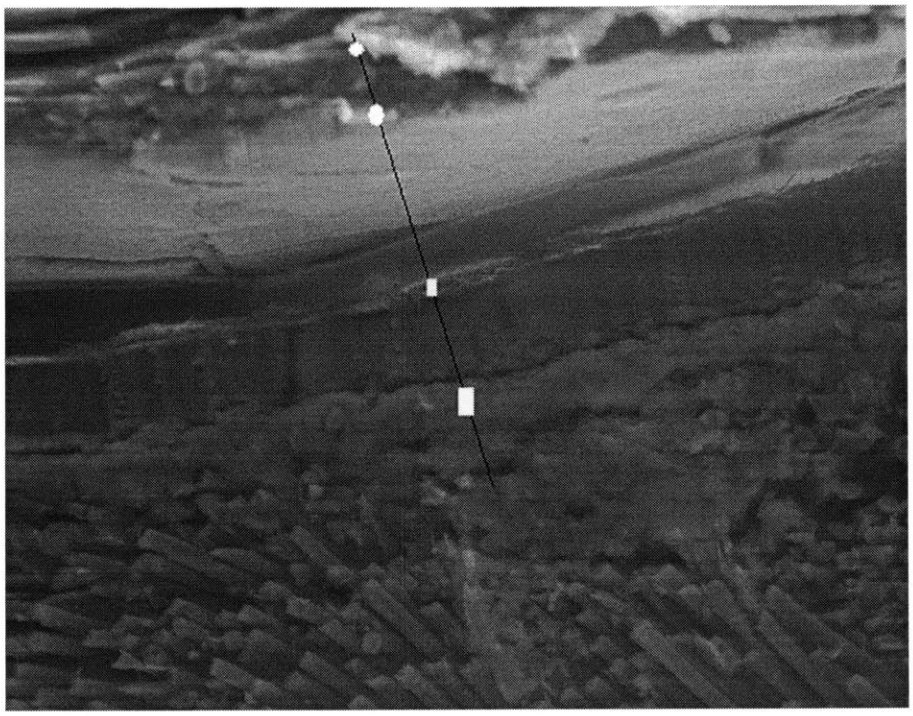

Figure 20. SEM image used for EDS line scan. The line scanned is shown in black, the circles are the locations of fluorine peaks and the squares represent the location of Pt peaks.

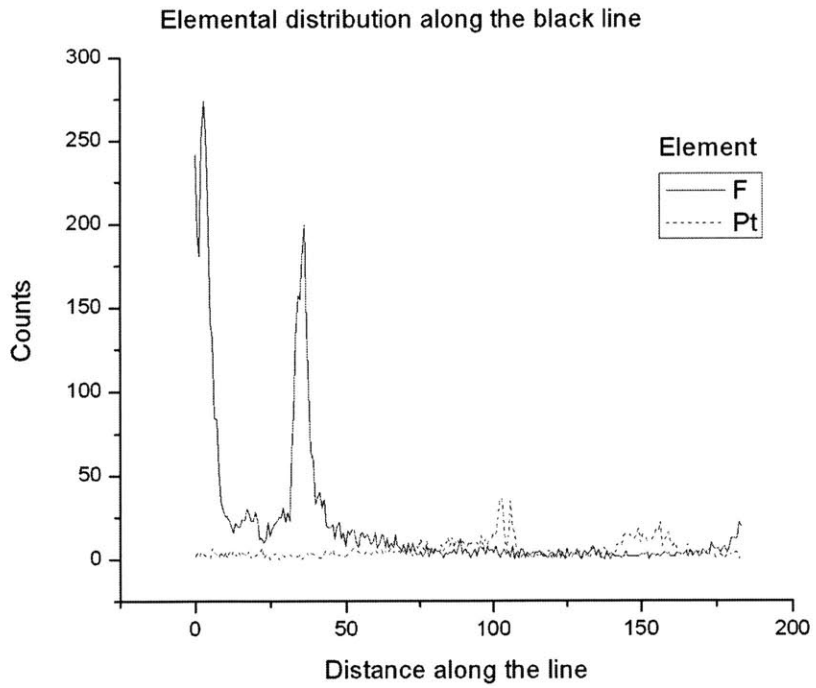

Figure 21. EDAX line scan corresponding to Figure 20.

Using the Photoshop software package and the elemental distributions shown below, it was possible to determine the location of the two fluorine and two platinum peaks. The two fluorine peaks occurred at the two bright locations denoted by the ovals in Figure 20 above, and the locations of the platinum peaks are denoted by the rectangles. The sharper Pt peak (the smaller, top rectangle) corresponds to the cathode side; specifically, to the part of the electrospun catalyst layer that is stuck to the membrane. The broader platinum peak corresponds to the anode (the lower, larger rectangle). The two fluorine peaks are located within the microporous layer of the GDL that is on the cathode side. There are no fluorine peaks within the membrane itself, but this is possibly due to the fact that the membrane could be located beneath the surrounding layers.

This tells us two important facts about our electrode structure. The first is that the electrospun layer is not mechanically strong, and tends to separate in its thickness direction. When this occurs, the fibers with the platinum, nearest to the membrane stay with the membrane, suggesting that they are well embedded in it. Secondly, the sharp fluorine peaks suggest that the Nafion ionomer added to the cathode electrode is not well-dispersed within the electrospun catalyst layer, but rather, it pools in certain locations beneath the catalyst layer in the microporous layer. This is not surprising, given the macroporous nature of the electrospun layer and the method of applying the Nafion ionomer solution. It is likely that the liquid ionomer flows through the electrospun layer before much of the solvent has had time to evaporate, and when it does begin to evaporate and leave a layer of polymer, it has already fallen through to the microporous layer.

3.3 TEM Results

TEM images used for particle counts were taken at magnifications of 200,000, 270,000 or 400,000. Since many of the particles were not spherical, the "diameter" was taken as the average of each particle's two perpendicular lengths. Table 3 summarizes the particle size distributions in terms of average diameter and standard deviation.

Table 3. Mean particle diameter and standard deviation as a function of sputtering time.

Sputtering Time [min]	Pt Loading [mg/cm^2]	Avg. Particle size [nm]	Standard Deviation [nm]
0.75	0.0105	2.05	0.65
1.5	0.021	3.76	1.49
3	0.043	4.98	2.24
4.5	0.063	5.07	2.13
6	0.084	6.37	2.77
8	0.112	7.25	3.27

As the sputtering time increases, the particle size increases and the standard deviation of the distribution increases, as the particle size distribution widens and shifts to the right (higher diameters). It has been shown previously that Pt sputtered on graphite substrates follows an island growth mechanism, in which small individual polycrystalline clusters of Pt are first formed. As sputtering time increases, these begin to join together, forming larger islands, and eventually coalesce into a continuous film [46]. This appears to be the method of growth in this case as well, as smaller particles grow and merge with nearby particles as the sputtering time increases. This is probably the reason for the large number of irregularly shaped particles. Figure 22 shows TEM images and the corresponding particle size distributions for each sputtering time. Note the shift in the peaks of the particle size distributions, and the relative heights of the 2nd and 3rd bins as

the sputtering time is increased (below 6 minutes the 2nd bin is the highest, for 6 and 8 minutes the 3rd bin is the highest. The sample sputtered for 45s shows many areas of contrast between light and dark gray, other than the black areas. Perhaps this indicates that for the other samples, which do not have this contrast, a thin platinum film covers the entire surface, whereas for the samples sputtered for only 45 s, this film has not yet been entirely formed. For all the other loadings then, the particles form on top of this platinum film. Therefore, the particle size distribution may not be very accurate in predicting the electrochemical active area based on cyclic voltammetry, since much of the mass of the platinum is not in the form of particles, but rather, in the form of a thin film on the fiber's surface. Appendix A shows the high magnification TEM image of the sample sputtered for 45 s taken on a JEOL 2010 operating at 200 kV. It can be seen that the platinum has not yet formed a surface layer, and that the average particle diameter is roughly 2 nm.

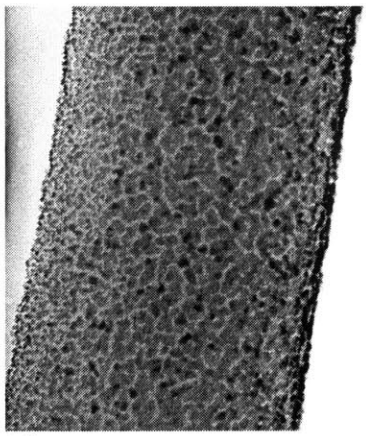
25 nm

(a)

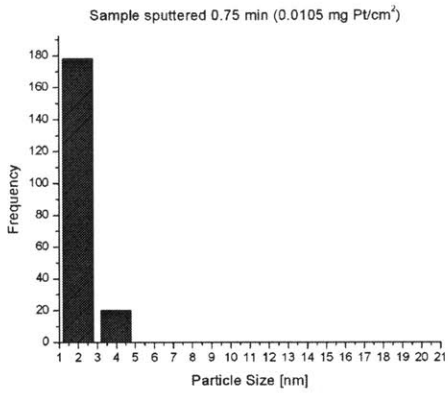
Sample sputtered 0.75 min (0.0105 mg Pt/cm²)
Frequency
Particle Size [nm]

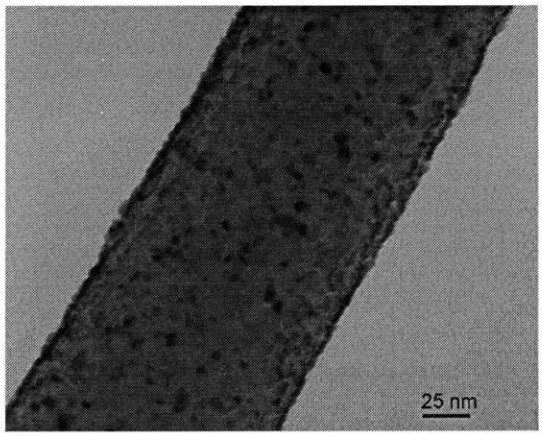
25 nm

(b)

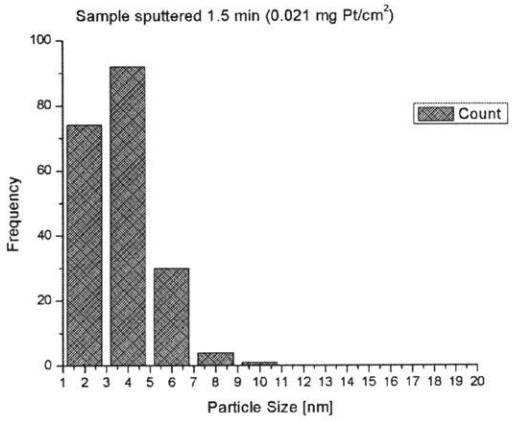
Sample sputtered 1.5 min (0.021 mg Pt/cm²)
Count
Frequency
Particle Size [nm]

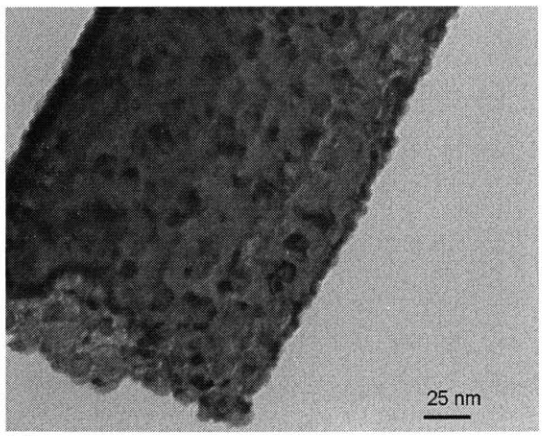
25 nm

(c)

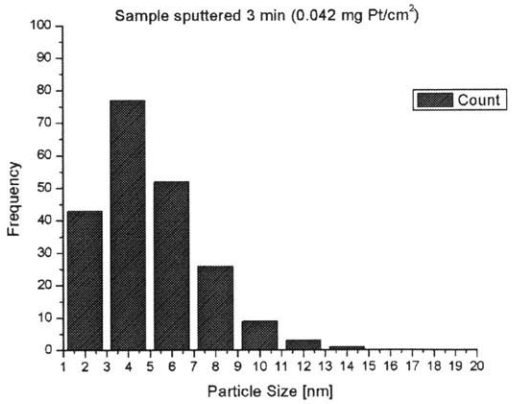
Sample sputtered 3 min (0.042 mg Pt/cm²)
Count
Frequency
Particle Size [nm]

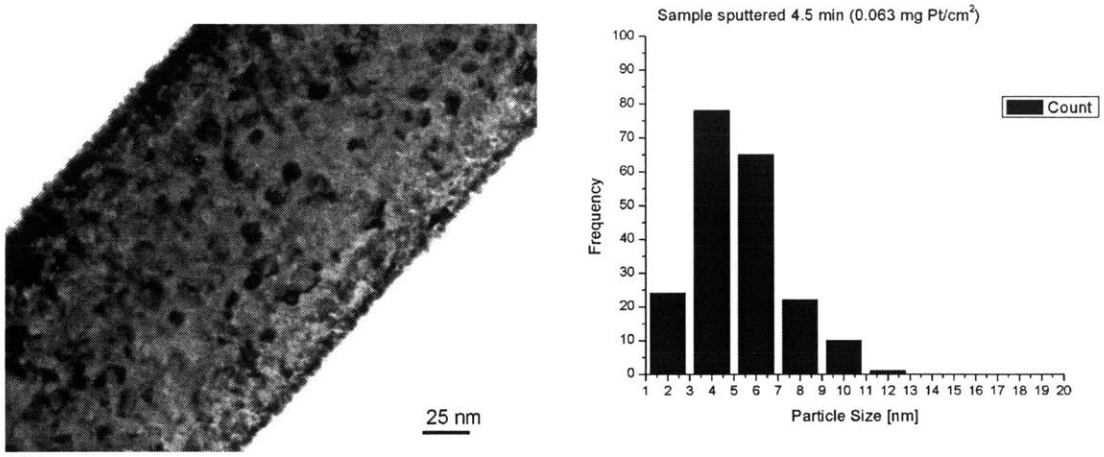

(d)

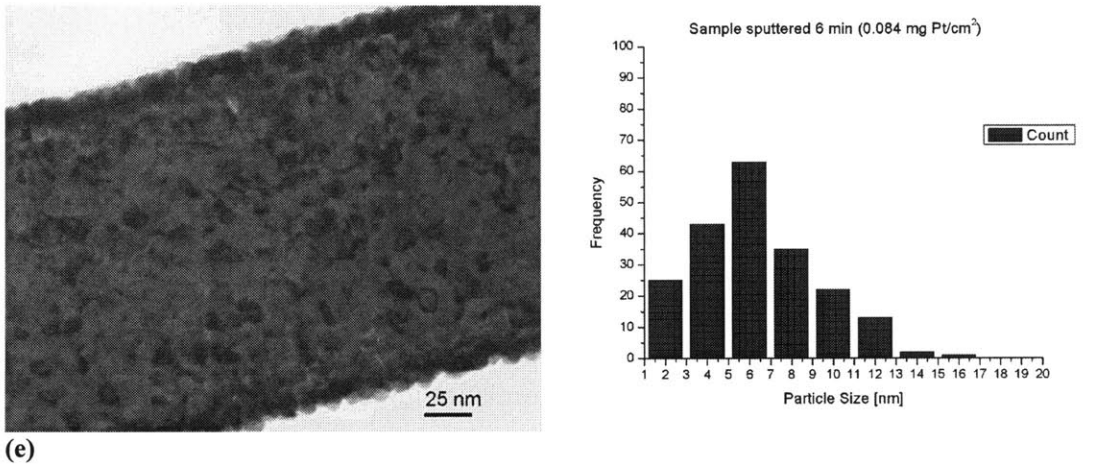

(e)

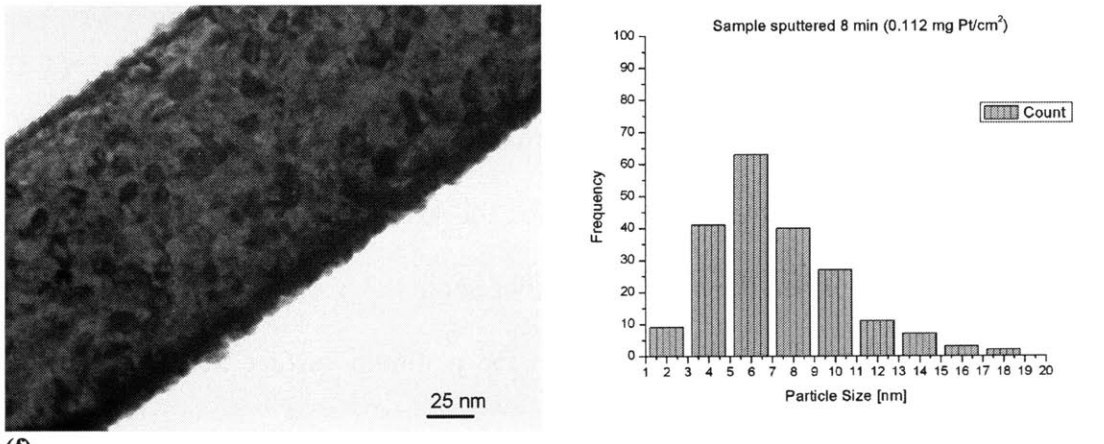

(f)

Figure 22. TEM images and particle size distributions for samples sputtered: (a) 45 seconds, (b) 1.5 minutes, (c) 3 min, (d) 4.5 min, (e) 6 min, and (f) 8 min.

4. Cyclic voltammetry and RDE

4.1 Cyclic Voltammetry

Cyclic voltammetry was performed in the same electrolyte used for oxygen reduction measurements, before the oxygen measurements were carried out. Instead of bubbling oxygen, the cell is bubbled with an inert gas in order to purge the oxygen from the solution. The electrode is not rotated during the cyclic voltammograms because there is no need to convectively bring reactants to the surface, since the reactants are simply water and protons, which exist in excess. A cyclic voltammogram of polycrystalline platinum in an acid solution is shown in Figure 23 [47].

For the positive sweep direction, starting in the oxygen region at ~0.7 V vs. RHE, oxides form on the platinum surface according to the reaction:

$$Pt+H_2O \rightarrow PtOH+H^+ +e^- \quad (4.1)$$

Further increasing the potential causes the formation of PtO by further oxidation according to:

$$PtOH \rightarrow PtO+H^+ +e^- \quad (4.2)$$

On the negative sweep, the oxides are removed from the electrode in one reduction peak; first equation (4.2) happens in the reverse direction followed by equation (4.1) happening in the reverse direction. When the potential reaches about 0.3 V vs. RHE in the negative sweep direction, hydrogen begins to adsorb on the platinum surface according to the reaction:

$$Pt+H_3O^+ +e^- \rightarrow PtH_{ads}+H_2O \quad (4.3)$$

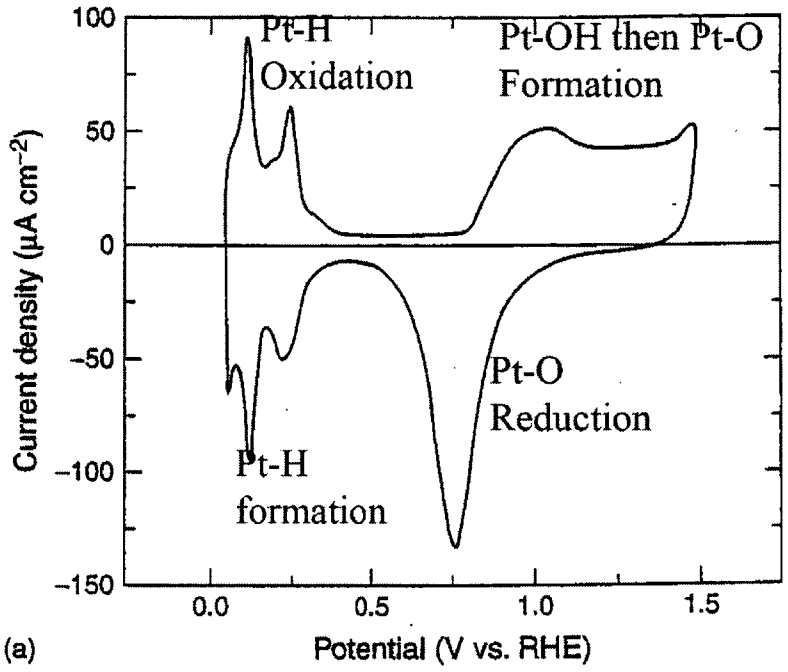

Figure 23. Typical cyclic voltammogram for platinum in acidic media showing the various peaks [47].

When the scan is reversed and the potential increases, this reaction occurs in reverse as the adsorbed hydrogen is cleaned off the surface of the platinum. There are three different hydrogen peaks corresponding to the adsorption/desorption contributions of the different single crystal faces of the polycrystalline platinum. In sulfuric acid, the most active is the (110) plane, followed by the (100) crystal plane and the least active peak is the (111) plane [48].

The region between the hydrogen and oxygen regions is called the double layer region, and there are no Faradaic reactions that occur in this potential window. The observed current is a charging current due to the capacitance of the electrochemical double layer, which is the approach of ions within the electrolyte towards the electronic charge within the electrode. This layer extends only a few tens of angstroms from the

electrode into the electrolyte. The current measured follows an exponential equation of a series RC-circuit, but quickly approaches the constant value observed in Figure 23 [6].

4.2 Cyclic voltammetry Results

CV and RDE were performed on samples sputtered 45 seconds, 1.5 minutes, 3 minutes, 4.5 minutes, 6 minutes and 8 minutes. A typical CV is shown below in Figure 24.

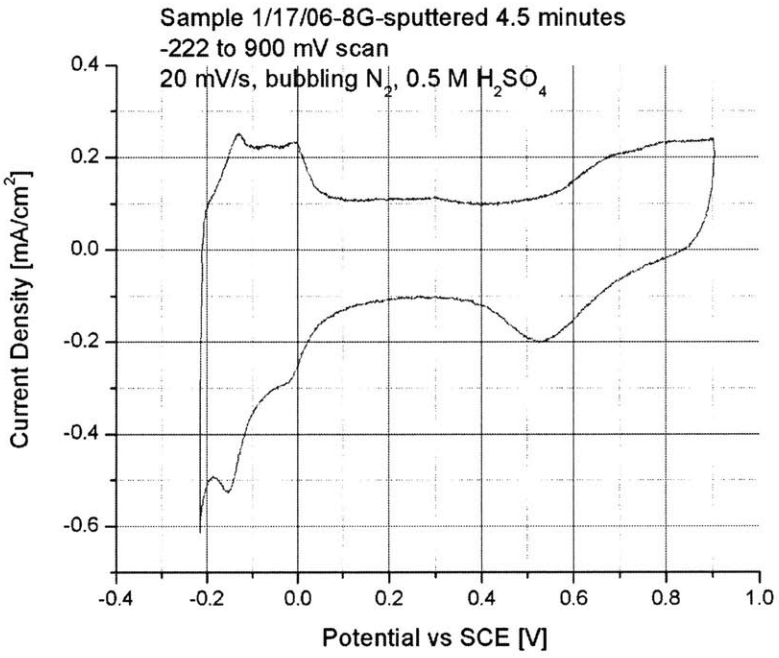

Figure 24. CV for an electrospun sample sputtered 4.5 minutes (0.06 mg/cm^2), taken in nitrogen purged 0.5 M H_2SO_4 electrolyte at a scan rate of 20 mV/s and room temperature.

Using cyclic voltammetry, it is possible to determine the electrochemical active area, or the actual surface area of platinum, of the working electrode. This is done by calculating the charge passed in the hydrogen adsorption/desorption region of the voltammogram, which is the region between 0.05 and 0.4 V vs. RHE. One must make sure to subtract the double layer charge from this charge passed, and one must also be careful that the CV

does not extend into the region of hydrogen evolution and oxidation. Once the hydrogen adsorption charge is known, in terms of charge per geometric area of the working electrode, that value is divided by 210 $\mu C/cm^2$, which is the theoretical value for an atomically flat platinum surface, assuming one adsorbed hydrogen per platinum atom and assuming that the surface density of platinum atoms equals the average of the various low-index single crystal planes [49]. The resulting quantity, called the roughness factor, is the electrochemical active area divided by the geometric area. When the roughness factor is divided by the platinum loading (in $mg/cm_{geometric}^2$) we arrive at the electrochemical active area per mass catalyst (m^2/g). This procedure is illustrated in Figure 25.

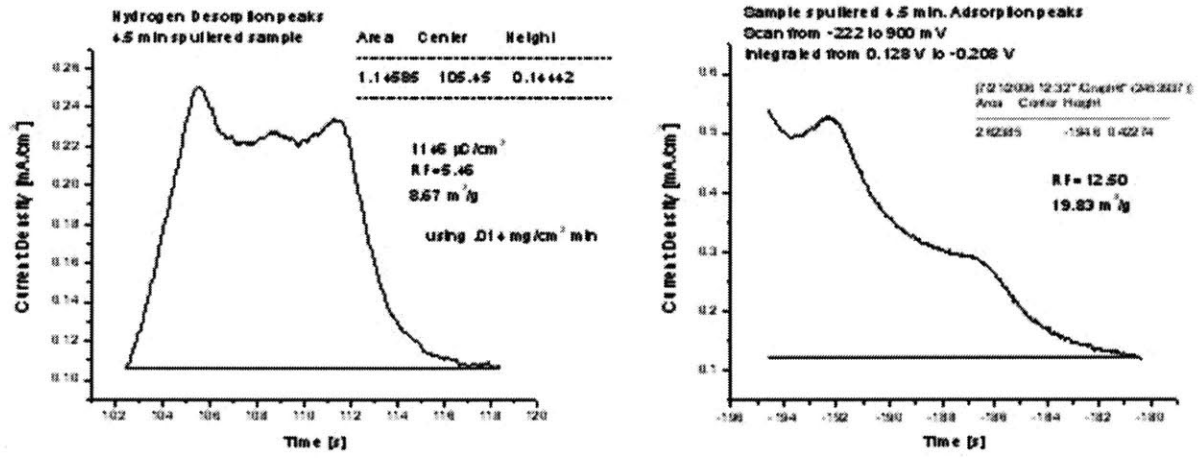

(a) **(b)**

Figure 25. Illustration of method to determine electrochemical active area from the hydrogen (a) adsorption and (b) desorption peaks.

This procedure was followed for all the samples tested. CVs for all the samples are shown in Figure 26. The current density in the hydrogen adsorption/desorption region increases with the platinum loading/sputtering time as would be expected. The current

density in the double layer region also increases with sputtering time, but the trend is not as clear (e.g. the sample sputtered 6 minutes has the highest capacitive current). Since charging current is a function solely of the surface area of the entire sample (platinum *and* carbon) this is understandable since the amount of carbon surface area present varies somewhat between samples.

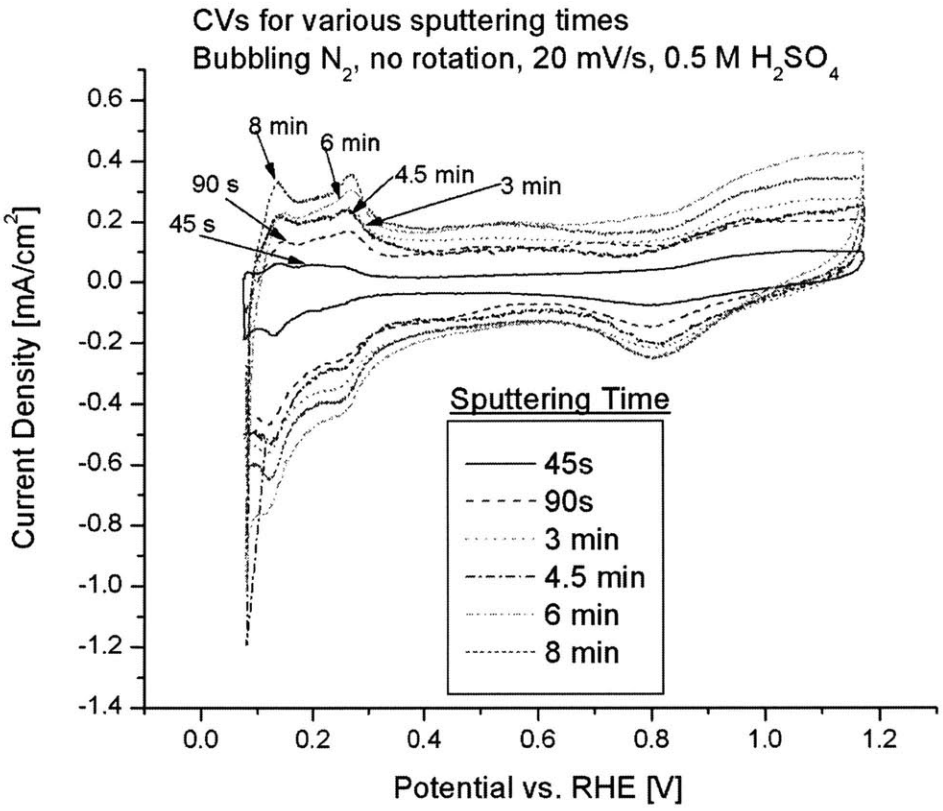

Figure 26. Cyclic voltammograms of electrospun samples sputtered for various times in 0.5 M H_2SO_4 electrolyte at a scan rate of 20 mV/s and room temperature.

The results in terms of the roughness factor are shown in Figure 27 below. The roughness factor increases with the sputtering time, which is to be expected, since the more platinum that is deposited, the more platinum area that is produced. The increase

seems to be somewhat exponential in nature (it is concave downward and levels off somewhat) since the effect of linearly increasing the loading is mitigated by the platinum film on the fibers and the increasing particle size inherent in the sputtering method. The effect of sputtering time on the particle size was discussed in the section on the TEM images.

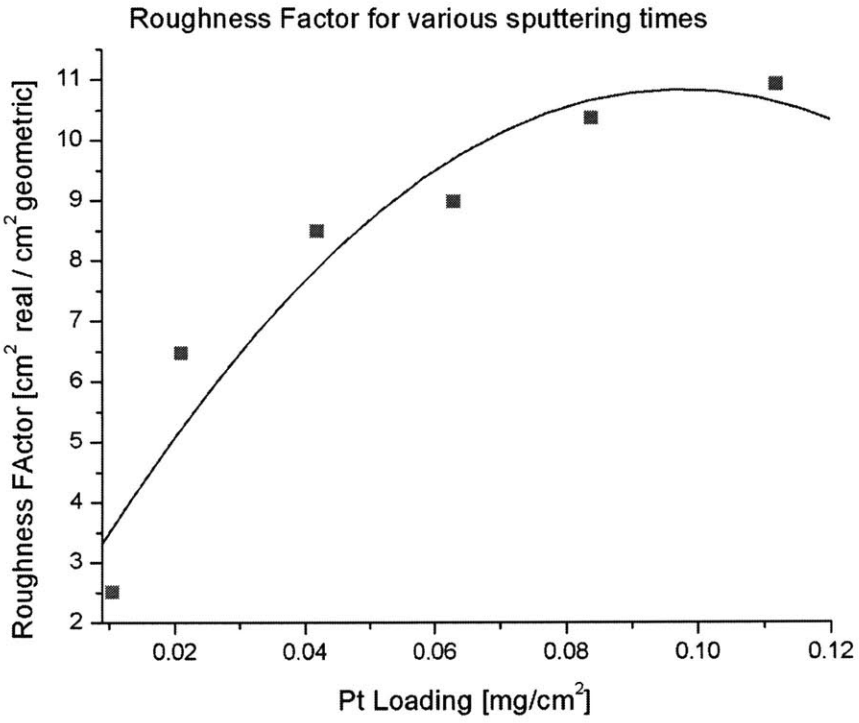

Figure 27. Roughness factor vs. Pt loading as determined by cyclic voltammetry.

The change in electrochemical active area (platinum specific surface area) with sputtering time is shown in Figure 28. It is evident that as that as the loading increases, the electrochemical active area decreases in what seems to be an exponential fashion. This is to be expected since: (a) the particle size increases with sputtering time and therefore the increase in electrochemical area is not as great as it would be if additional

platinum particles of the same size were added and (b) because the normalization is by the platinum loading, which increases linearly with sputtering time. The fact that the first data point (the 45 s sample ~0.01 mg/cm^2) does not have the highest ECA may be due to the fact that the particles are small enough such that the Pt does not adsorb hydrogen as well as "normal" sized platinum particles.

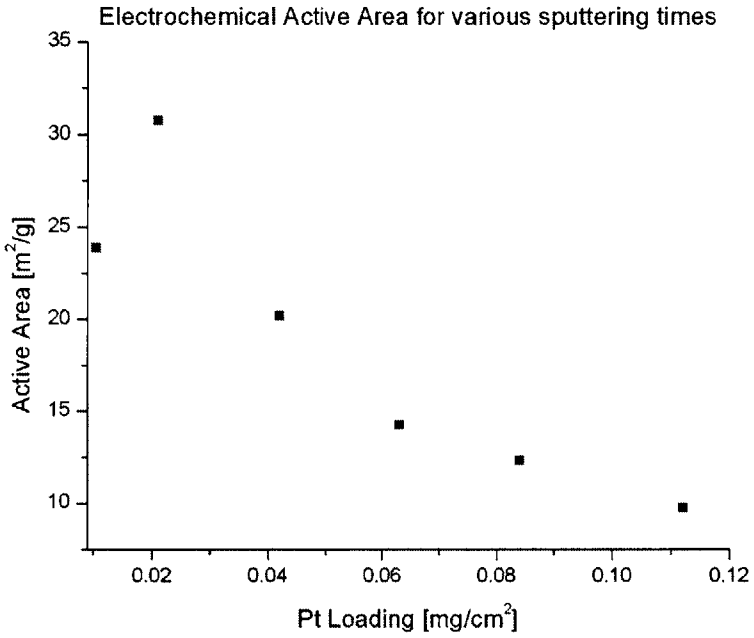

Figure 28. Electrochemical active area vs. Pt Loading determined by cyclic voltammetry.

It is possible to estimate the platinum specific active area of platinum particles from a "back of the envelope" calculation. Assuming perfect spheres and taking the surface area (πd^2), we can divide that by the weight of a platinum sphere (density of platinum, 21.45 g/cm^3, multiplied by volume, $\pi d^3/6$). The result (in units of area per mass) is only a function of diameter and is:

$$ECA=\frac{6}{\rho d} \tag{4.4}$$

Using this it is possible to compare the actual and theoretical electrochemical active areas for the particle sizes observed in TEM. This is shown in Figure 29 below.

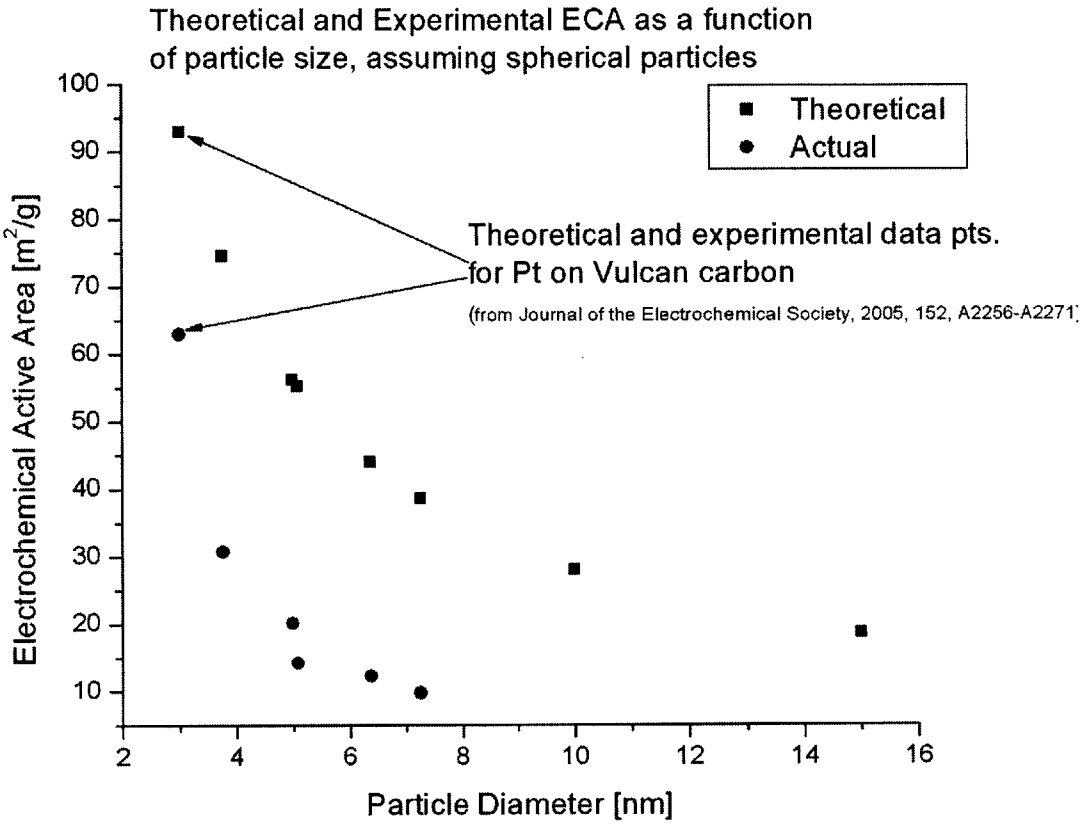

Figure 29. Comparison of experimental active area (circles) determined from cyclic voltammetry and theoretical active area (squares) as a function of particle size.

Clearly the actual electrochemical active area from CV is significantly less than the theoretical prediction in equation (4.4). This discrepancy is made even worse by the fact that spheres have the least surface area per unit volume of any shape, and the sputtered particles are far from spherical, so they should have a higher area ECA, if anything. This discrepancy could result from the nature of the sputtering deposition method. Based on the TEM images and the discussion in Section 3.3, it is thought that the fibers are actually covered with a thin film of platinum, on top of which particles of

platinum grow following an island growth mechanism. Since much of the mass of platinum is in this film, this could explain the significantly lower than theoretical electrochemical active area.

4.3 Rotating Disc Electrode Results

After the cyclic voltammograms were performed on each given sample, they were then immediately tested using the RDE configuration. A typical potential scan from 0.03 V to 1.17 V vs. RHE is shown in Figure 30.

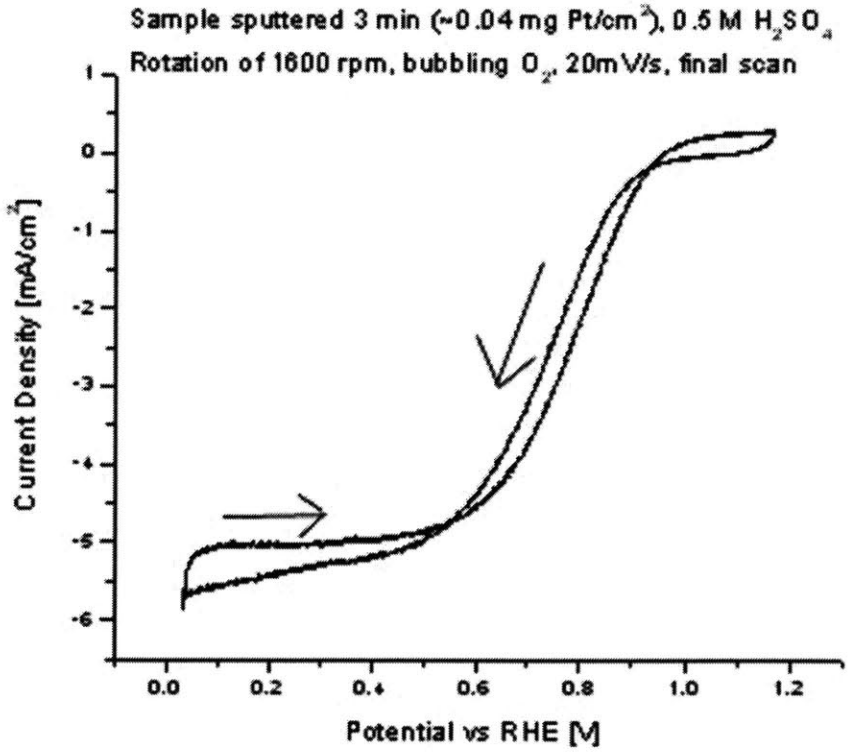

Figure 30. Oxygen Reduction Scan of sample sputtered 3 minutes using the RDE configuration. 0.5 M H_2SO_4, bubbling O_2, 1600 rpm, 20 mV/s at room temperature.

Within the region of mixed kinetic and diffusion current control, the positive going scan always exhibits larger currents at a given potential, and a lower overpotential for a given current. This can be explained by the oxide coverage on the platinum, which acts to inhibit the oxygen reduction reaction. In the positive scan direction, the oxide coverage on the electrode starts at higher potentials than the potential at which the oxides are removed on the negative sweep [50]. Therefore, in the positive sweep direction, currents are higher at a given overpotential. This can be seen in Figure 23 above.

A typical Koutecky-Levich plot using an electrospun sample sputtered with platinum is shown in Figure 31.

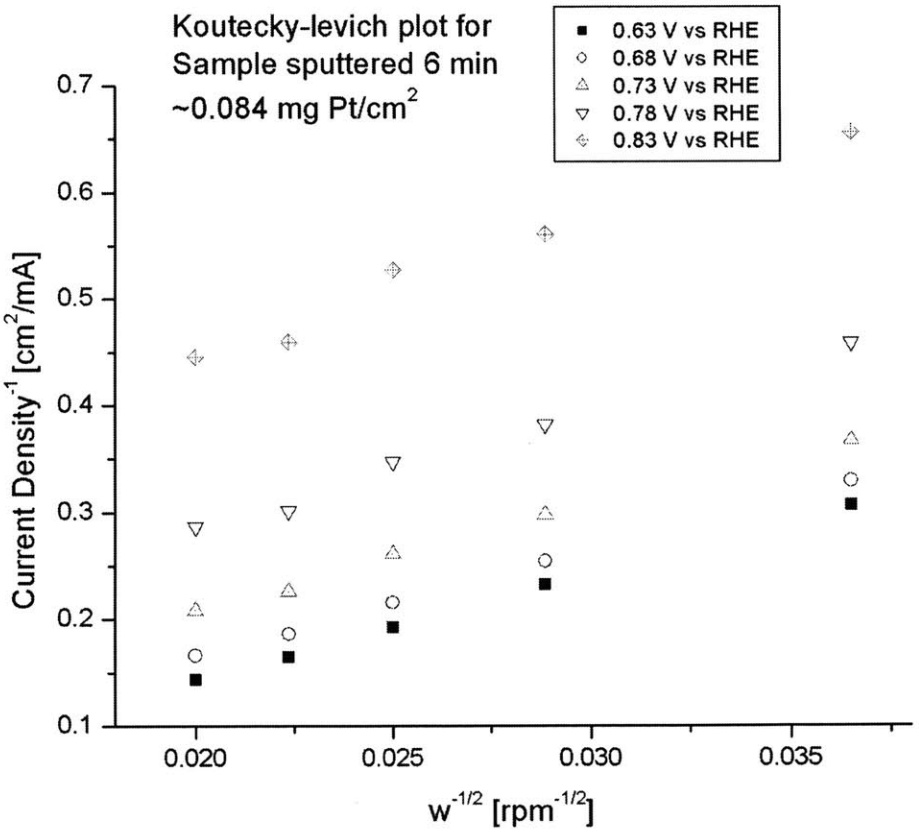

Figure 31. Typical Koutecky-Levich plot for sputtered samples.

The slopes of the lines are nearly parallel, and do come quite close to the theoretical value of 1/B, which is indicative of the current obeying a form of equation (1.10) or (1.12). However, at the higher overpotentials, the y-axis intercepts eventually become negative, which indicates an *enhancement* of the current beyond that which is predicted from the analysis. At the highest overpotentials, when i_k becomes very large, the intercept should become 0, corresponding to $1/\infty$, but should never become negative according to equation (1.10). I believe that this anomaly is due to the fact that our samples have a thickness on the order of 15 μm, making the surface not flush with the surrounding Teflon. This contributes another term to equation (1.10) similar to the $1/ i_f$ term in equation (1.12), except that this term is not in the form of a limiting current, but rather enhances the measured current since the platinum surface protrudes further into the flow field than the flat Teflon surface. In summary, this analysis reveals that the RDE equations are not completely satisfied for the electrodes tested here, and the current may be enhanced by some unknown term resulting from the thickness of the electrode. However, the deviation is probably small at higher potentials, and comparison between different samples should be valid.

Using the positive scan of the oxygen reduction curves at a rotation rate of 1600 rpm, it is possible to compare the performance of the different electrodes. As was explained in Section 1.8 above, the current measured is a mixture of the mass transport limited current (which also takes into account the extra term discussed above) and the kinetic limited current following equation (1.10). In order to compare the kinetic currents

and to control for the mass-transport, it is common to apply the following corrective equation based on equation (1.10) [35]:

$$i_k = \frac{i_d \times i}{i_d - i}, \tag{4.5}$$

where i is the measured current and i_d is the observed limiting current in the mass transfer controlled region of high overpotentials. This correction is small in the kinetic dominated region (low overpotentials), which is the region of interest, and where it is common to compare performance at 0.9 V vs. RHE, as was mentioned above. Figure 32 shows the deviation between the measured current and the kinetic current after the correction. Clearly the correction is small at low overpotentials such as 0.9 V vs. RHE and this indicates that 0.9 V is well within the kinetic-controlled regime and this correction method is acceptable.

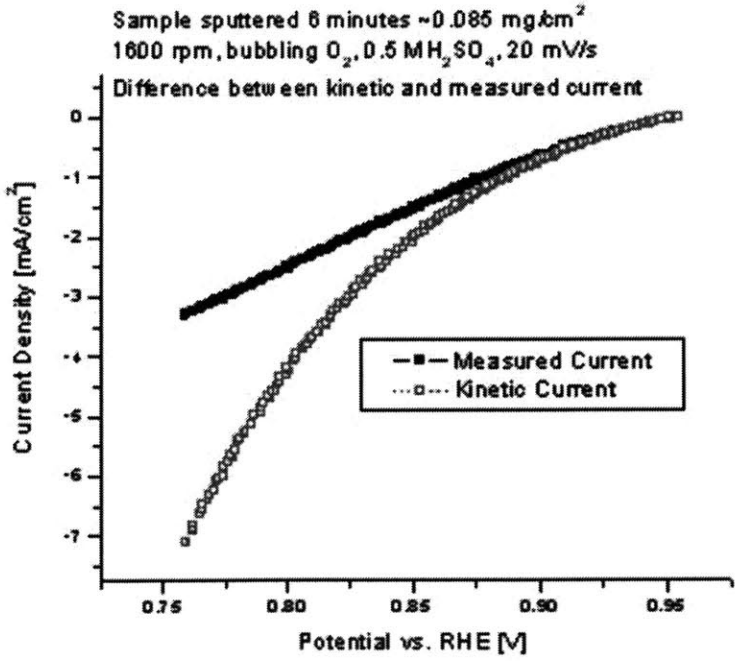

Figure 32. Measured current and mass-transport corrected current as a function of potential in the RDE, 0.5 M H_2SO_4, bubbling O_2, 1600 rpm, 20 mV/s, positive scan.

Using this kinetic current density, a table was constructed comparing the performance of the different sputtering times at 0.9 V vs. RHE. This table compares three different currents at 0.9 V: the geometric activity, which is the current normalized by the geometric electrode area, the mass activity, which is the current normalized by the platinum loading, and the specific activity, which is the current normalized by the electrochemical active area (determined from cyclic voltammetry). Table 4 summarizes the results.

Table 4. Results from RDE for various sputtering time. All measurements are from mass transport corrected currents at 0.9 V vs. RHE, taken at 1600 rpm in 0.5 M H_2SO_4 at room temperature. Tafel slopes are between 0.94 and 0.88 V vs. RHE.

Time sputtered [min]	Pt Loading [mg/cm^2]	Geometric Current [mA/cm^2]	Mass Current [mA/mg]	Specific Current [mA/cm$^2_{Pt}$]	Tafel Slope [mV/decade]
0.75	0.0105	0.065	6.14	0.026	-44
1.5	0.021	0.394	18.78	0.059	-66
3	0.042	0.567	13.50	0.067	-73
4.5	0.063	0.574	9.11	0.064	-92
6	0.084	0.722	8.59	0.070	-66
8	0.112	0.815	7.27	0.075	-61

Not surprisingly, the geometric current density increases with the platinum loading. Also unsurprisingly, the mass activity decreases with platinum loading, aside from the lowest loaded sample, since mass activity is the current divided by the platinum loading. This is in agreement with many published results that observe an increase in mass activity as particle size decreases, with some reporting peaks in the mass activity at around 3 nm particle sizes [9] [51]. This is thought to be due to the changing fractions of (100) and (111) crystal faces on the surfaces of the particle as the size is decreased [51].

The specific activity seems to increase sharply with platinum loading between the 0.75 and 1.5 minute sputtering times, and increases slightly with platinum loading above the 1.5 minute time. This makes sense considering the particle size distributions from the TEM images, which show the average particle size increasing from around 2 nm to 3.76 nm for the 0.75 and 1.5 minute sputtering times, respectively, and from 3.76 nm to 7.25 nm in the range of 1.5 minutes to 8 minutes sputtering time. The particle size effect is thought to become more pronounced for particles below 3 nm, which could explain the trend in specific activity.

In the literature, specific activities for carbon supported platinum (average diameter of 3.7 nm) and bulk polycrystalline platinum in 0.5 M H_2SO_4 at 60° C were reported to be 0.035 and 0.110 mA/cm^2_{Pt}, respectively [52]. The values here are between those reported above, which makes sense given the larger particle size and polycrystalline nature of the sputtered platinum particles. Additionally, the specific activities reported here are all within 16$\mu A/cm^2_{Pt}$ of each other (aside from the lowest loading), which is reasonable since this is the most intrinsic of the measurements of catalytic activity, and all the samples are made of the same catalyst. The reason behind the poor performance of the lowest loading sample may be evidence for the particle size effect. Specific and mass activity as a function of loading is presented in graphical form in Figure 33.

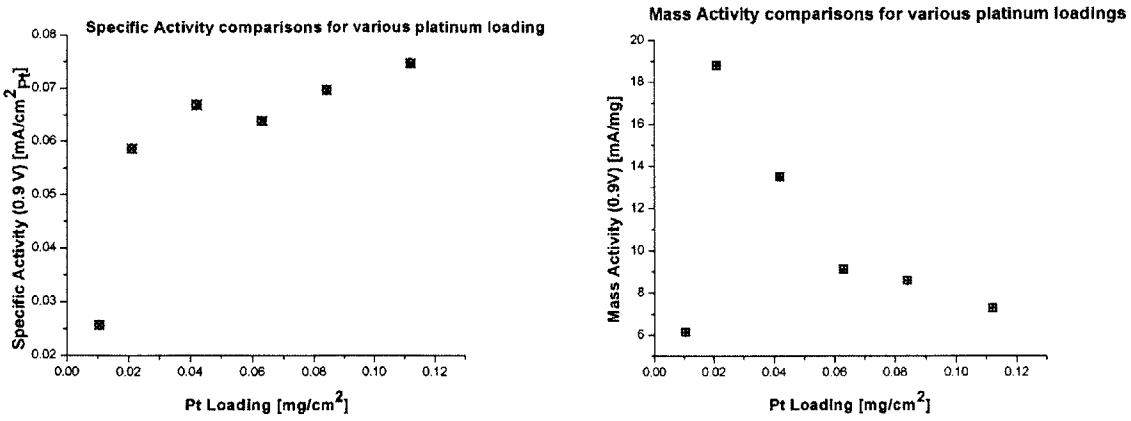

(a) (b)

Figure 33. (a) Specific Activity and (b) Mass Activity as a function of platinum loading as determined by RDE at 0.9 V vs. RHE, with 0.5 M H_2SO_4, bubbling O_2, 1600 rpm, 20 mV/s, room temperature.

The mass activity curve (Figure 33(b)) follows the general shape of the electrochemical active area curve. This makes sense, since electrochemical active area has units of m^2_{Pt}/g_{Pt} and mass activity has units of mA/g_{Pt}. Thus, if the current is proportional to the surface area of platinum, the mass activity curve should be the same shape as the ECA curve. This condition seems to be fulfilled, since Figure 33(a) shows the specific activity to be only slightly increasing in the loading range tested, meaning that the current is almost proportional to the electrochemical platinum surface area.

The oxygen reduction performance is best summarized using Tafel plots and is shown for the six sputtered samples in Figure 34 below. The high potential Tafel slopes are similar for the samples sputtered 1.5 minutes, 3 minutes, 6 minutes and 8 minutes, at ~60-70 mV/decade, which is similar to the literature values [9]. For the sample sputtered 4.5 minutes, the Tafel slope is anomalously high at 92 mV/decade. The sample sputtered for 45 seconds has a significantly lower Tafel slope of ~45 mV/decade, and at lower potentials, exhibits a significantly different "mid-range" Tafel slope than the other

samples. The reason for this may have to do with the small particle size and the non-continuous platinum film on the fibers of the sample sputtered for 45 s.

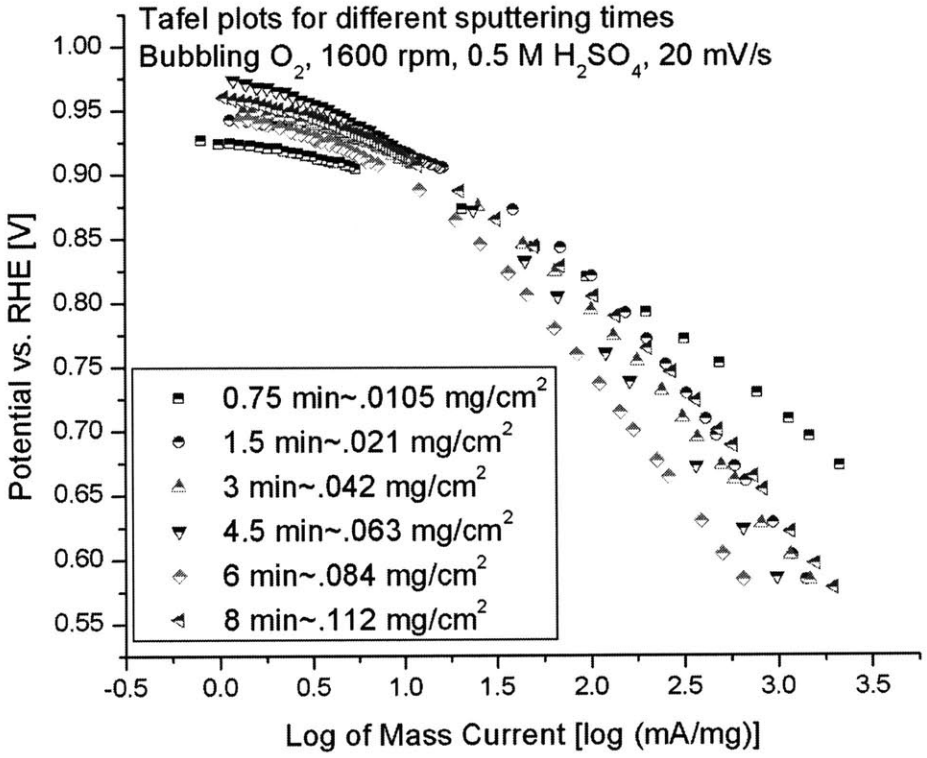

Figure 34. Tafel plots for the various sputtering times. Data from RDE with 0.5 M H_2SO_4, bubbling O_2, 1600 rpm, 20 mV/s, at room temperature.

Perhaps the best comparison for this RDE data is from a paper published in 1994 by Poirier and Stoner [46]. They sputter deposited platinum onto polished graphite stubs and performed cyclic voltammetry and rotating disc electrode measurements in 0.5 M H_2SO_4 at 25 °C in order to determine their oxygen reduction activity. Additionally, they performed TEM in order to ascertain the particles size of the platinum deposits. The deposition rate in those experiments was 0.013 mg/cm^2/min, similar to the 0.014 mg/cm^2/min in these experiments. The TEM images for different loadings are shown in

Figure 35 below. It looks similar to the TEM images presented above, with the exception being that the spacing between particles is larger for the electrospun carbon supports, presumably due to the larger surface area when compared to the flat graphite stubs.

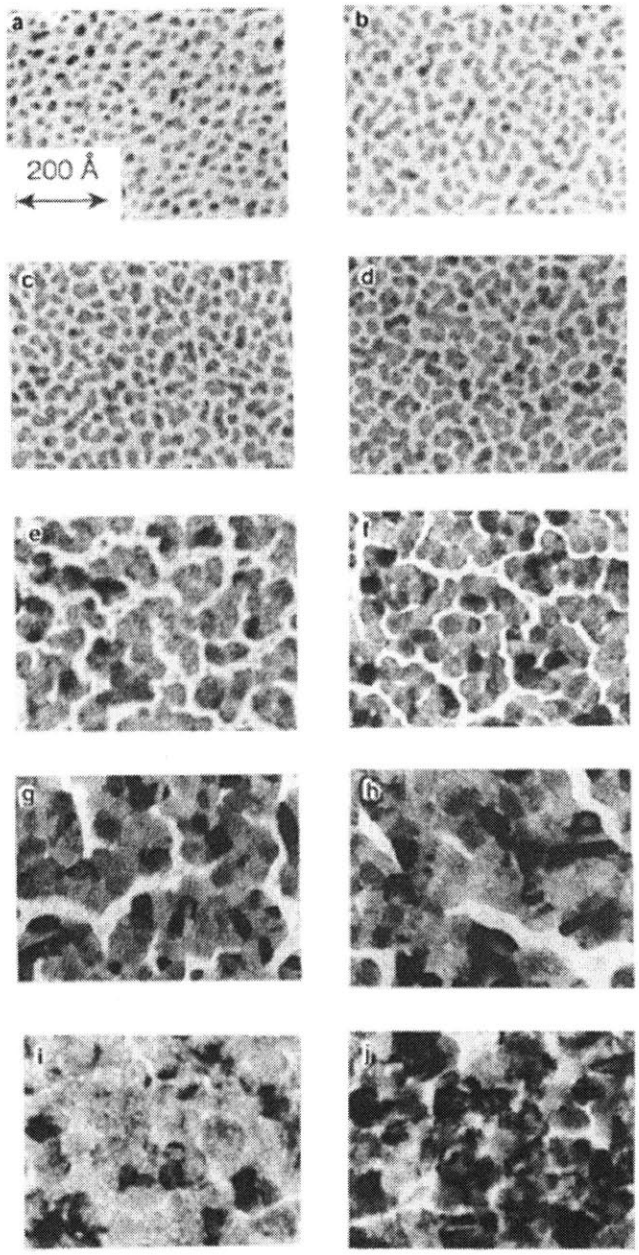

Fig. 1. Transmission electron micrograph of thin film Pt, loading and deposition times indicated, respectively. a, 6.6 μg/cm² (0.5 min); b, 10 μg/cm² (0.75 min); c, 13 μg/cm² (1 min); d, 20 μg/cm² (1.5 min); e, 26 μg/cm² (2 min); f, 40 μg/cm² (3 min); g, 53 μg/cm² (4 min); h, 66 μg/cm² (5 min); i, 135 μg/cm² (10 min); j, 200 μg/cm² (15 min).

Figure 35. TEM images of platinum sputtered on graphite stubs for various [46].

From their cyclic voltammetry data, they concluded that the particle size increased and the electrochemical active area decreased with sputtering time (i.e. platinum loading), similar to the data presented here. The electrochemical active area as a function of Pt loading is shown in Figure 36 for their study and for this study. It is quite similar, except that the ECA in this work seems to fall slightly more rapidly.

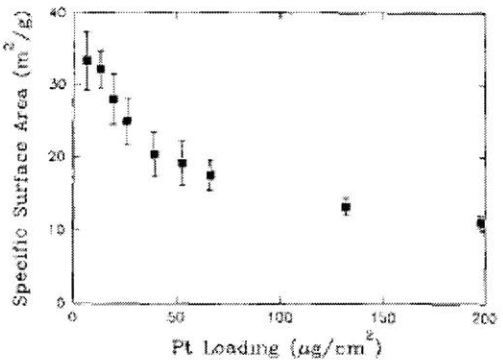

Fig. 7. Specific surface area vs. Pt loading.

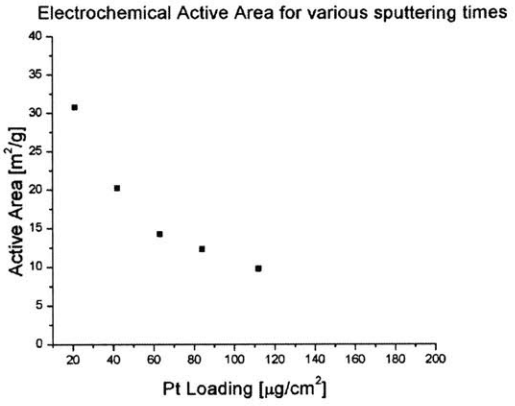

(a) (b)

Figure 36. Active area vs. Pt loading from (a) reference [46] and (b) this study. Data determined by cyclic voltammetry at the same conditions (0.5 M H_2SO_4, bubbling N_2, 20 mV/s, room temperature) in both cases.

From their RDE data they determined that the mass activity (0.9 V) decreased with sputtering time, due to the fact that particles size as well as the loading increased, similar to the data presented here. The most interesting conclusion that they draw, however, is that the specific activity (0.9 V) of their platinum was higher for smaller sputtering times, which conflicts with literature results on the particle size effect [49]. This is shown in Figure 37(a) below. They speculate that the sputtering method produces a different type of platinum structure from chemical deposition methods [46]. However, their data is quite scattered and the trend may not actually be significant. This also conflicts with the data from this study, shown in Figure 37(b), which suggests an increase in the specific activity with particle size.

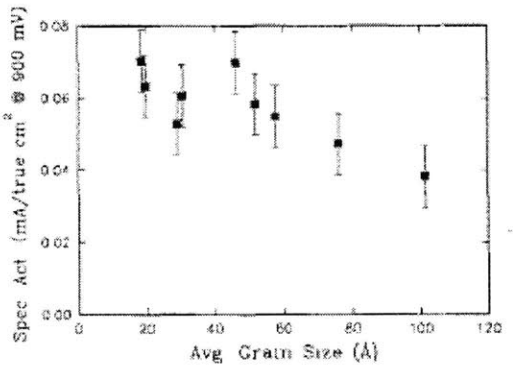

Fig. 12. Specific activity vs. average grain size.

(a)

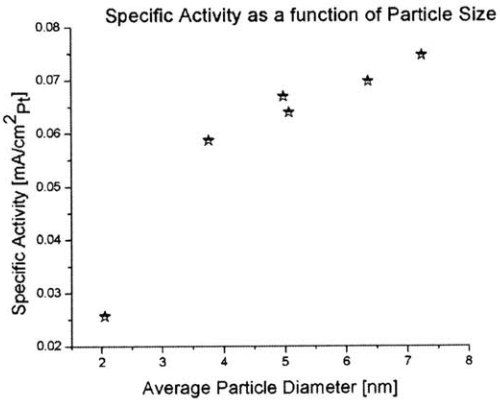

(b)

Figure 37. Specific activity vs. particle size from (a) reference [46] and (b) this work. Data determined by RDE at the same conditions (0.5 M H_2SO_4, bubbling O_2, 1600 rpm, 20 mV/s, at room temperature) in both cases.

5. Fuel Cell Results and Discussion

Since electrospinning was used to fabricate the whole catalyst layer, RDE was not entirely descriptive for our purposes. In other words, we fabricated electrodes, rather than just supported catalyst particles. Therefore it was important to test the sputtered electrospun layers in a fuel cell setup in order to evaluate the performance of the electrode structure as well as of the catalyst. The results and analysis are presented below.

5.1 Methodologies used in Fuel Cell Testing and Diagnostics

A recent paper by Williams, Kunz and Fenton details an approximate method for identifying what they term the six types of overpotentials that are significant in PEM fuel cells (they divide the typical three further into six, which is more useful as a diagnostic tool) [12]. Aside from these losses, there can also be polarization due to hydrogen crossover and oxidation directly on the cathode. Additionally, platinum catalyst and/or carbon support material can be oxidized directly on the cathode. These oxidations reduce the cell voltage and lead to a mixed potential at the cathode. Internal short circuits can also cause cell polarization and can be identified using linear sweep voltammetry. This analysis, however, assumes no internal short circuits are present, is based upon the Butler-Volmer kinetic model, assumes oxygen reduction is first order in oxygen concentration, assumes there is no overpotential due to hydrogen oxidation, and oxygen transport is by Fickian diffusion.

The six polarizations that can be distinguished are:

1. Non-electrode ohmic overpotential: contact resistances, electron resistance outside the cathode (the GDL) and proton resistance,

2. Cathode Electrode Ohmic overpotential: resistance of electron and proton transport within the cathode,
3. Non-electrode concentration overpotential: resistance to oxygen transport in GDL and ionomer film,
4. Electrode concentration overpotential: resistance to oxygen transport in the cathode,
5. Tafel Activation overpotential: from oxygen reduction kinetics as the current density increases,
6. Activation overpotential: losses at low current densities (<10mA/cm^2).

Determining Non-electrode Ohmic Overpotential:

To measure $R_{\text{Non-electrode ohmic}}$ (often called "cell internal resistance") the current-interrupt technique is used, in which the current is interrupted for a few microseconds. This causes the voltage drop due to all the non-electrode components to decay (the ohmic overpotential vanishes much faster than the electrochemical overpotentials) and when a reading is taken a few microseconds after the interruption, the difference in the potentials gives the ohmic overpotential of the non-electrode components, $\eta_{\text{Non-electrode ohmic}}$. Then,

$$R_{\text{Non-electrode ohmic}} = \eta_{\text{Non-electrode ohmic}} / i. \quad (5.1)$$

The current interruption should be performed at every current density data point. The high frequency resistance is another method that can be used to determine the non-electrode ohmic overpotential [53].

These techniques account for all electronic resistances, and if the electrode itself is not sufficiently conductive, then its electrical resistance will be included in this

overpotential. However, most electrodes (catalyst layers) have sufficient conductivity such that the ohmic loss is negligible. After this has been determined, the fuel cell's corrected voltage is:

$$V_{corr1}=V_{cell}+iR_{non\text{-}electrode}. \tag{5.2}$$

Determining Cathode Ohmic Overpotential:

At high overpotentials (current densities > 100 mA/cm^2) the oxygen reduction reaction current following the Butler-Volmer model is given by:

$$i = i_0 \times \left[\frac{\text{Concentration } (O_2 \text{ catalyst})}{\text{Concentration}(O_2 \text{ bulk})}\right] \times \exp[-\alpha f \eta], \tag{5.3}$$

where the symbols are the same as above. Fick's Law of Diffusion (assuming linear diffusion only) also is first order in oxygen concentration. A property called the current ratio is defined as the current density obtained from pure oxygen feed to an air feed at the same potential. The theoretical current ratio is 4.8 (moles O_2 in pure O_2 vs. moles O_2 in air) if there is no ohmic overpotential and the utilization is not too large (which would cause the concentration ratio to drop). If at some high overpotential (where the current density should be first order with oxygen concentration) the current ratio, using V_{corr1}, is less than 4.8, it indicates the presence of electrode (cathodic) ohmic overpotential.

To determine the value of $R_{cathode}$, one must set its value such that performance plots of V_{corr1}+i $R_{cathode}$ vs. current density yields a current ratio of 4.8 for oxygen and air polarization curves. This is an iterative procedure: assume a value for $R_{cathode}$, plot new curves of V_{corr2} =Vc_{orr1}+i $R_{cathode}$ vs. current density and measure the current ratio, and repeat until the current ratio equals 4.8, which indicates the current is first order with oxygen concentration. As mentioned above, electrodes are usually sufficiently

electronically conductive such that most of $R_{cathode}$ is due to proton resistance within the cathode layer. Now,

$$V_{corr2} = V_{cell} + iR_{non\text{-}electrode} + iR_{cathode}, \quad (5.4)$$

which is the cell current corrected for all ohmic losses.

Determining Non-Electrode Concentration Overpotential:

The limiting current of an electrochemical cell is due to concentration losses at parts of the cell where the reactant is *not* consumed. The Butler-Volmer equation can be written in terms of the limiting current:

$$i/(1-i/i_{lim}) = i_o' \exp[(V_{eq}-V_{corr2})/b'], \quad (5.5)$$

where b' is the modified Tafel slope and i_o' is the modified exchange current density. To find i_{lim}, one uses another iterative procedure to make the plot of ohmic free voltage, V_{corr2} vs. log $[i/(1-i/i_{lim})]$, a straight line. Using this value of i_{lim}, we now have V_{corr3}, which is the voltage further corrected for non-electrode concentration overpotential. The slope of this line is b', and is a modified Tafel slope. The difference between V_{corr2} and V_{corr3} is the non-electrode concentration overpotential, and cannot be written as an explicit function of current density (it changes with current density).

Determining Cathode Electrode Concentration Overpotential:

It has been shown that a concentration overpotential associated with the catalyst layer causes the Tafel slope of the ORR to double from the kinetically controlled ~70-80 mV/decade to ~140-150 mV/decade. Thus to determine the concentration overpotential associated with the cathode catalyst layer, we compare the actual kinetic Tafel slope

using oxygen (in the 10-100 mA/cm^2 region to eliminate any mass transport losses) to the slope of the V_{corr3} plot (i_{lim} chosen for straight V_{corr2} vs. log $i/(1-i/i_{lim})$). Thus, if the slope of the V_{corr3} line is greater (more negative) than the actual (typically 70-80 mV/dec) kinetic Tafel slope, it indicates cathode electrode concentration overpotential, which is the difference between the two lines (V_{corr3} and the ~70 mV/decade sloped line). This can be written as a specific function of current density as follows:

$$\eta_{conc,\ electrode} = (b'-b)\ \log[i/i_b] \tag{5.6}$$

Now,

$$V_{corr4} = V_{corr3} + \eta_{conc,\ electrode}, \tag{5.7}$$

and this new value is actually the Tafel slope in the kinetically controlled region extrapolated across all current densities.

Determining the Cathode Activation Overpotential due to ORR kinetics

The Tafel overpotential is:

$$\eta_{act,Tafel} = b\ \log(i/10), \tag{5.8}$$

and it is the voltage loss representing the energy required to drive the ORR reaction at increasing current densities. Now,

$$V_{corr5} = V_{corr4} + \eta_{act,Tafel}, \tag{5.9}$$

and it is a straight horizontal line independent of current density, which is the cell voltage at 10 mA/cm^2. It should be noted that 10 mA/cm^2 is a somewhat arbitrary choice for the beginning of the "Tafel region."

Determining the Cathode Activation Overpotential from Catalyst Activity

The difference between the equilibrium voltage and the voltage at 10 mA/cm^2 is the activation overpotential, $\eta_{activity}$, and is not fundamentally meaningful, except that we chose 10 mA/cm^2 as the starting point for evaluating the Tafel slope, rather than at zero current (where hydrogen crossover, etc. would give errors to the Tafel slope).

$$V_{corr6} = V_{corr5} + \eta_{activation}, \quad (5.10)$$

It should be emphasized that this method is only an approximate one. Sources of error include the assumption of first order oxygen reduction kinetics, which is definitely not exact. The assumption of no anode overpotential may also be a slight source of error.

5.2 Fuel Cell Test Results

Fuel cell testing was carried out for samples sputtered with platinum for 1.5 minutes, 3 minutes, 4.5 minutes, 6 minutes and 8 minutes on both ETEK gas diffusion layers and on electrospun layers. A membrane electrode assembly was also made using a commercial ETEK cathode with a loading of 0.5 mg Pt/cm^2 for comparison. These 11 MEAs were tested using both oxygen and air as described in the experimental section, and then the performance was analyzed using the step-by-step method explained above. Comparisons could then be made between electrospun and GDL supports, between different sputtering times, and between the sputtered cathodes and the standard ETEK cathode.

A typical plot for the H_2/Air and H_2/O_2 performance of sputtered electrodes after correcting for the non-electrode ohmic resistance is shown below in Figure 38. Although the performance varied somewhat for the different sputtering times, especially at the

higher current values, this MEA, which was had a cathode electrospun layer sputtered for 8 minutes, has a fairly representative performance. All samples had a *very* steep initial drop in voltage at low currents. The oxygen performance typically got to about 800-1100 mA/cm^2 before reaching the voltage cutoff of 0.1 V, while the air performance typically reached only 300-400 mA/cm^2. The losses at the higher current densities are typically attributed to mass transport limitations, and the variation between electrodes could be due to a number of factors, including variations in the MEA's assembly that could adversely affect the mass transport properties of the cell. This will be elaborated upon later.

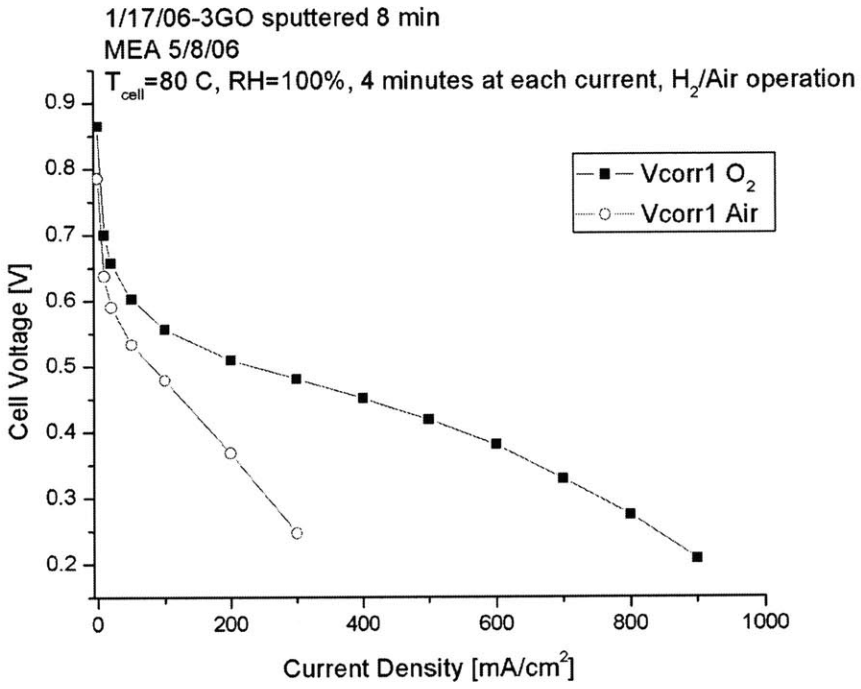

Figure 38. Representative performance curves with air and oxygen for a sample sputtered 8 minutes (0.11 mg Pt/cm^2). All data collected at 80 °C, RH~100%, and atmospheric pressure.

Comparison to Standard E-TEK Cathodes

Figure 39 shows the voltage curve for the MEA constructed with a standard E-TEK electrode as the cathode. Clearly the E-TEK cathode outperforms the sputtered

cathode by a great deal. At 200 mA/cm^2, the MEA made with the E-TEK cathode has a voltage of 0.658 V, while the best of the sputtered samples has a voltage of roughly 0.4 V at the same current.

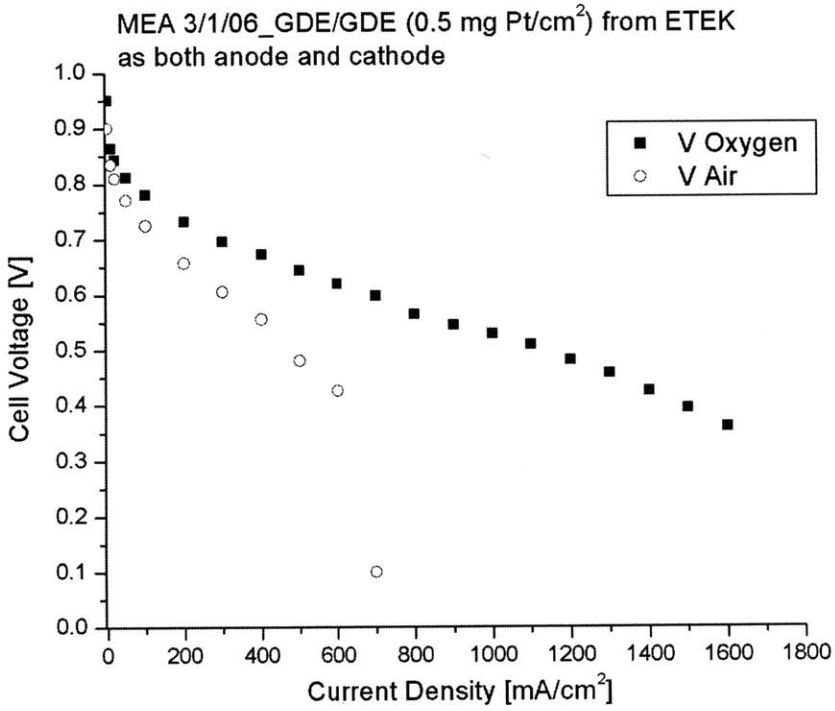

Figure 39. Performance, before any corrections, of MEA with E-TEK GDE (Pt loading 0.5 mg/cm^2) on both anode *and* cathode, for oxygen and air on cathode. All data collected at 80 °C, RH~100%, and atmospheric pressure.

In terms of the power density, the E-TEK cathode almost triples the performance of the *best* sputtered cathode. Figure 40 shows power density curves for H_2/O_2 feeds, and it can be seen that the peak power for the E-TEK sample is 0.595 W/cm^2 at a voltage of 0.43 V, and at 0.4 V the current is 1500 mA/cm^2. The sputtered sample's peak power is 0.225 W/cm^2 at a voltage of 0.28 V, while at 0.4 V the current is only 500 mA/cm^2, which is identical to the literature value for a GDL sputtered to a loading of 0.08 mg/cm^2 [28].

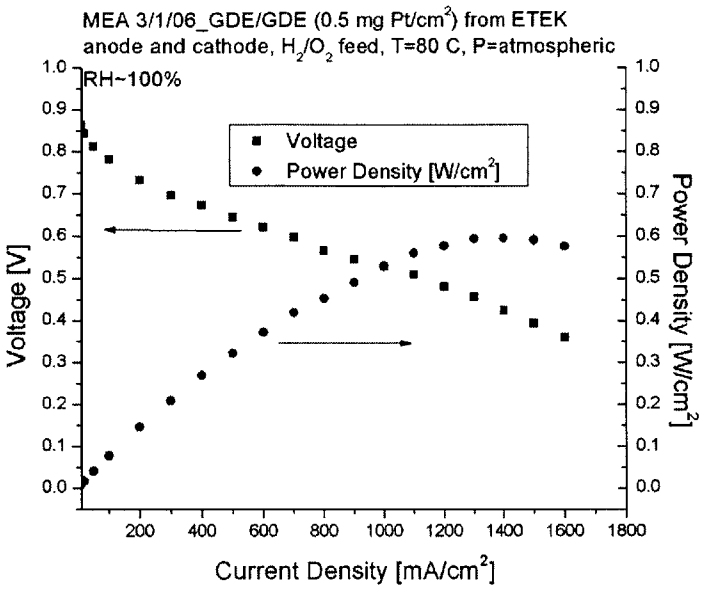

(a)

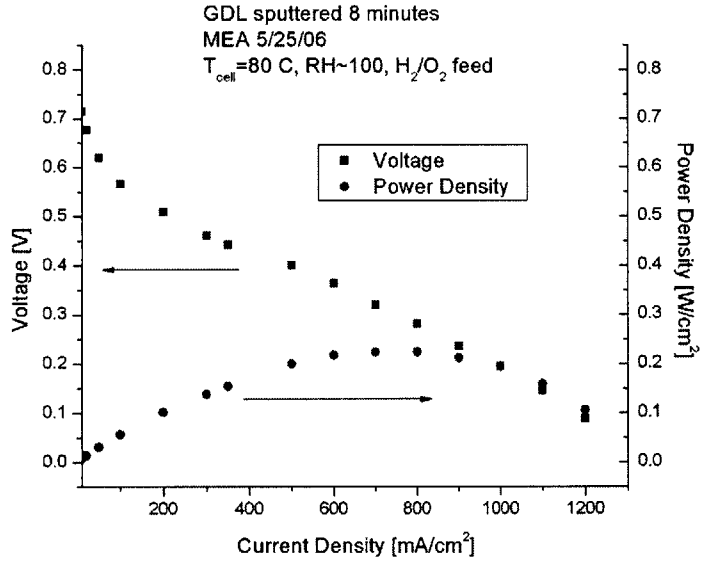

(b)

Figure 40. Voltage and power density curves as a function of current density for (a) the E-TEK cathode (0.5 mg/cm^2) and (b) the best sputtered cathode: GDL sputtered 8 minutes (0.11 mg/cm^2).

At 0.6 V, the maximum power for the sputtered samples, on H_2/Air operation, is only ~0.012 W/cm^2, almost two orders of magnitude below the requisite 0.9 W/cm^2 for automotive applications [27].

Identifying Overpotentials

Figure 41 shows the same MEAs as Figures 38 and 39 after each of the step by step corrections described above. Note that the x-axis is on a log scale. It should be mentioned that for all the sputtered samples, Vcorr4 is actually an extrapolation of the approximate *theoretical* Tafel slope of 70 mV/decade rather than the actual Tafel slope of the oxygen data, as recommended by the authors [12]. This is because *all* the sputtered MEAs had *oxygen* Tafel slopes of roughly double the theoretical values, indicative of mass transport losses in the cathode catalyst layer, even under oxygen feed at low current densities. Since the Tafel slopes from RDE are around the theoretical value of 60-70 mV/decade, this indicates that the double Tafel slopes at low currents are due to other factors, such as electrode structure, rather than the catalyst itself.

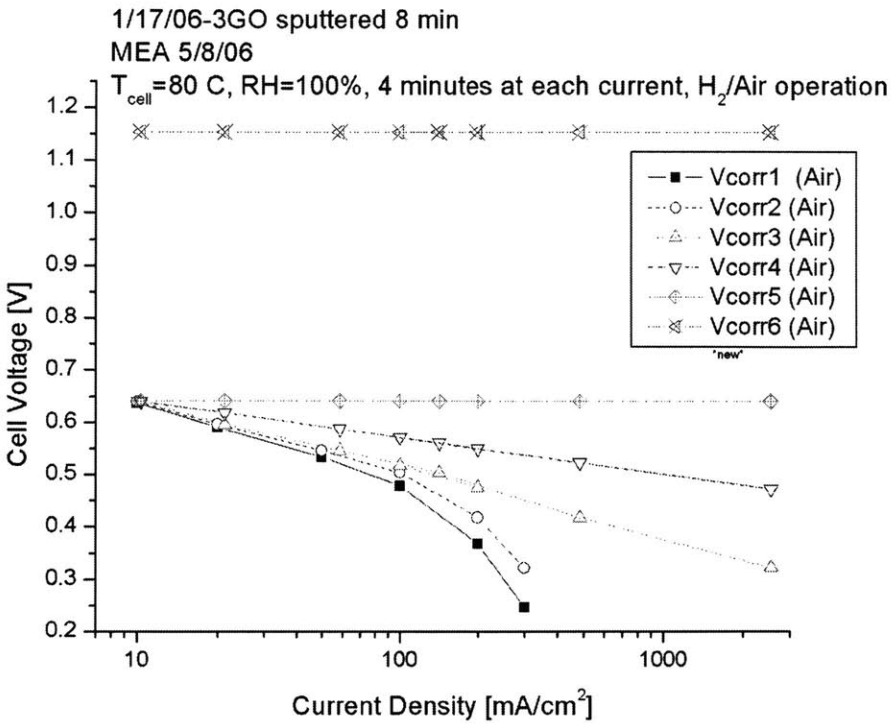

(a)

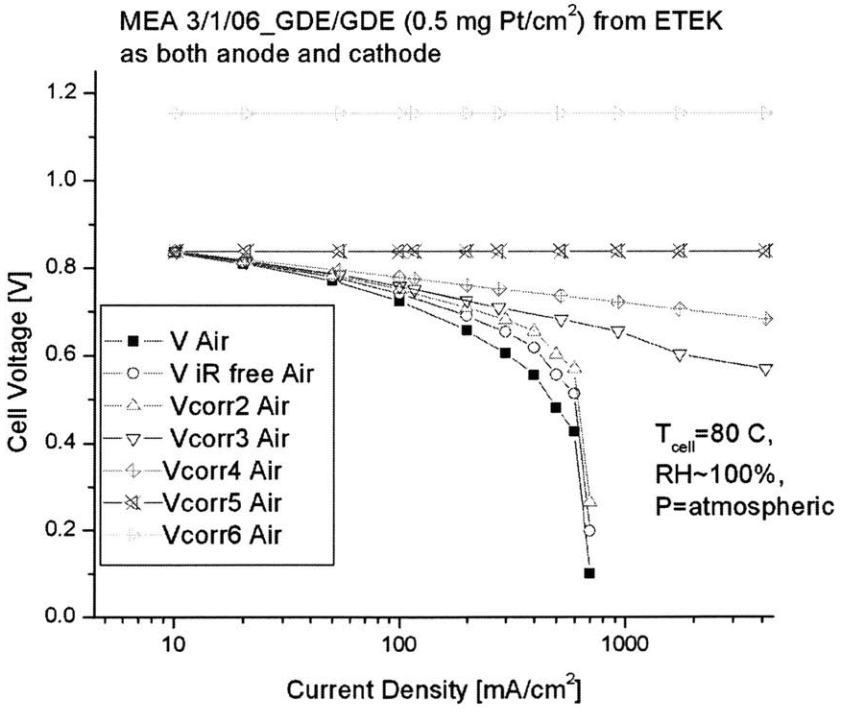

(b)

Figure 41. Performance curves with air, after applying the step-by-step correction method for (a) sample sputtered 8 minutes (0.11 mg Pt/cm^2), and (b) E-TEK GDE (0.5 mg Pt/cm^2). All data collected at 80 °C, RH~100%, and atmospheric pressure.

Using this data, it was possible to extract the sources of overpotential at any current density. This is shown as a pie chart in Figure 42 for the sample sputtered 8 min and the E-TEK sample, at current densities of 200 mA/cm^2.

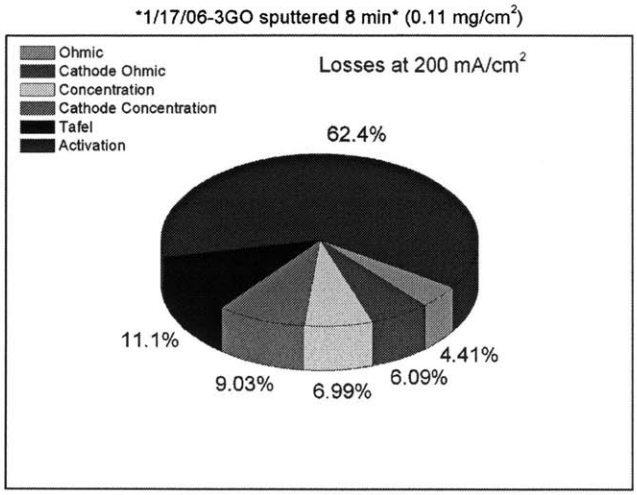

(a)

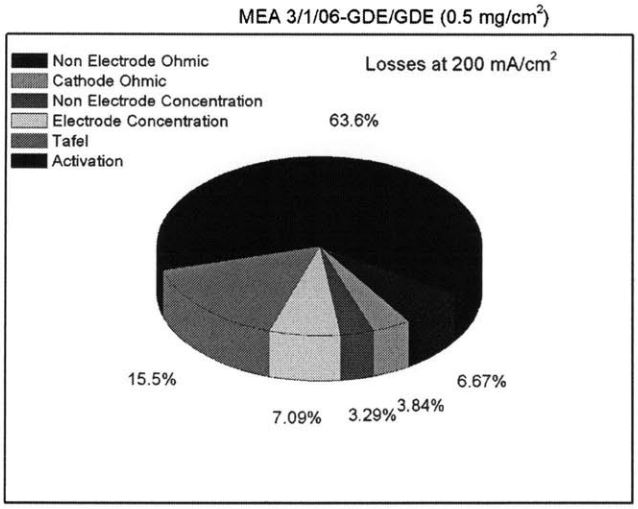

(b)

Figure 42. Contribution of each source of overpotential to the total overpotential at 200 mA/cm^2 with an H_2/Air feed, for the sample (a) sputtered 8 minutes and (b) E-TEK electrode. Data collected at 80 °C, RH~100%, and atmospheric pressure.

The largest source of overpotential is clearly the two kinetic overpotentials, followed by the two mass transport overpotentials. This was typical for the sputtered samples and the charts for all the samples can be found in Appendix B.

To facilitate comparisons between different samples, absolute data was compiled on the voltage losses from each overpotential at 200 mA/cm^2. This current was chosen because it was the largest current density at which all samples could be measured (one sample had its maximum current at 250 mA/cm^2). This is presented in Table 5.

Table 5. Sources of overpotential, in volts, at 200 mA/cm^2 for each sample tested. Sputtering time in parentheses. All data collected at 80 °C, RH~100%, and atmospheric pressure.

	GDL (1.5)	E-spun (1.5)	GDL (3)	E-spun (3)	GDL (4.5)	E-spun (4.5)
Ohmic [V]	0.0341	0.0404	0.0484	0.0569	0.0378	0.039
Cathode Ohmic [V]	0.0518	0.0344	0.0212	0.0168	0.028	0.0516
Concentration [V]	0.1075	0.0741	0.0501	0.116	0.07674	0.0779
Electrode Concentration [V]	0.0915	0.0733	0.0654	0.094	0.0895	0.0641
Tafel [V]	0.09107	0.09107	0.09107	0.09107	0.09107	0.09107
Activation [V]	0.5418	0.5289	0.5114	0.4782	0.5125	0.5374
	GDL (6)	**E-spun (6)**	**GDL (8)**	**E-spun (8)**	**GDE**	
Ohmic [V]	0.0297	0.0228	0.03738	0.0362	0.033	
Cathode Ohmic [V]	0.0344	0.052	0.0192	0.05	0.019	
Concentration [V]	0.0375	0.04	0.04713	0.0574	0.0163	
Electrode Concentration [V]	0.101	0.0571	0.0672	0.0742	0.0351	
Tafel [V]	0.0911	0.09107	0.0911	0.0912	0.07676	
Activation [V]	0.4828	0.4991	0.4993	0.5123	0.31482	

Comparing Losses in GDL vs. Electrospun Supports, and in Different Sputtering Times

Overall, the electrospun supports performed as well as the GDLs for the sputtered MEAs tested. This can be seen below in Figure 43 (a) and (b) showing the performance for air and oxygen, respectively, of all the sputtered MEAs tested. There is no absolute trend in the data in terms of performance vs. sputtering time or in terms of GDL vs. electrospun supports. At the five different loadings, the GDL outperformed the electrospun supports at 200 mA/cm^2 for three of the five loadings, which is hardly a trend. Generally, the higher loaded samples did perform better overall than did the lower loaded samples. This is consistent with some of the data in the literature that suggests that there is a peak sputtering time beyond which the GDL's pores become overly blocked with platinum and performance decreases, but that this occurs at a loading *above* 0.1 mg Pt/cm^2 [28]. This issue clearly would not apply to electrospun supports, due to their macroporosity. Both samples sputtered for 4.5 minutes seemed to have a lower performance than would be expected, and the samples sputtered for 3 minutes performed better than expected.

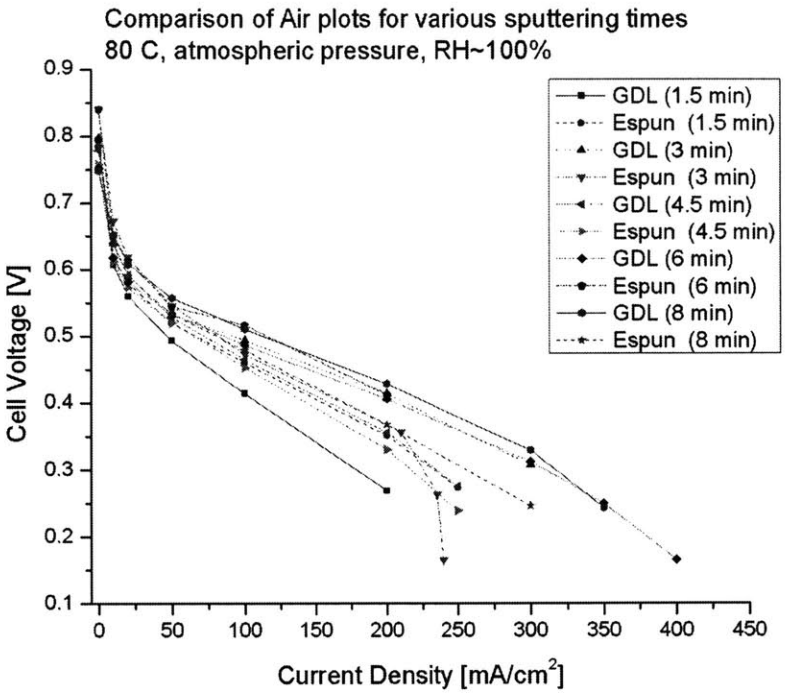

(a)

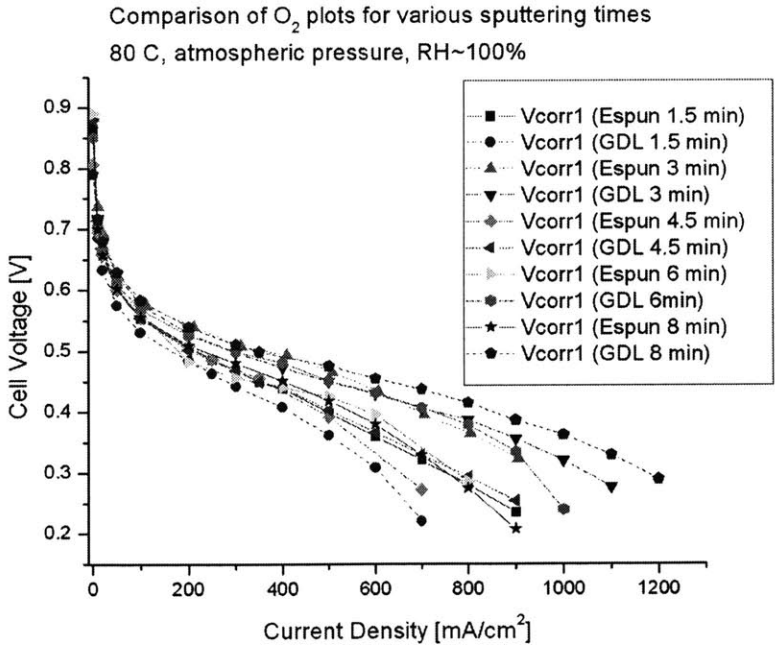

(b)

Figure 43. Fuel cell performance curves for (a) Air and (b) Oxygen feed on the cathode. All data collected at 80 °C, RH~100%, and atmospheric pressure.

One trend that at first seems legitimate is in the cathode ohmic overpotential. For the lower loaded samples (sputtering times of 1.5 and 3 minutes) the GDL supports had higher cathode ohmic overpotentials that the electrospun supports, while for the higher loaded samples (sputtering times of 4.5, 6 and 8 minutes) the electrospun layers had higher cathode ohmic overpotentials than their GDL counterparts. This is shown in Figure 44 below. The reason for this might have to do with the MEA structure since cathode ohmic overpotential is mainly due to resistance to proton transfer in the cathode, and this suggests that increased cathode ohmic losses result from a deficiency of Nafion surrounding the platinum particles. However, there is not a plausible explanation as to why the cathode ohmic resistance suddenly jumps for the electrospun layers as sputtering time increases. Furthermore, this step is the step in the analysis that is the most approximate, since it relies on the assumptions of the current being first order with oxygen concentration, as mentioned above.

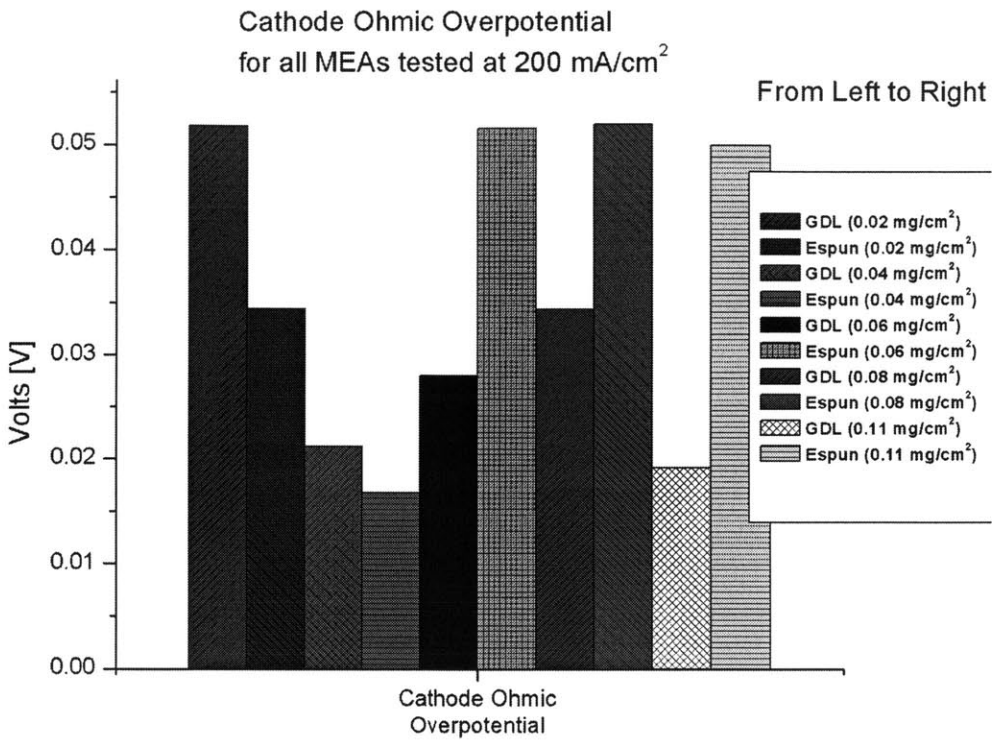

Figure 44. Cathode ohmic overpotential for all sputtered samples tested, at 200 mA/cm^2. All data collected at 80 °C, RH~100%, and atmospheric pressure.

The activation overpotential for each sputtered MEA is shown below. While there is not much of a trend in the data between the various sputtering times, it can be seen that for the low loading samples (1.5 and 3 minutes) the GDLs have greater activation overpotential, while for the higher loaded samples (4.5, 6 and 8 minutes) the electrospun supports have greater activation overpotential. This is shown in Figure 45 below. This is the same trend as observed for the cathode ohmic overpotential. At this point there is not an explanation for these trends, and it is not known if they are significant, or if they are related.

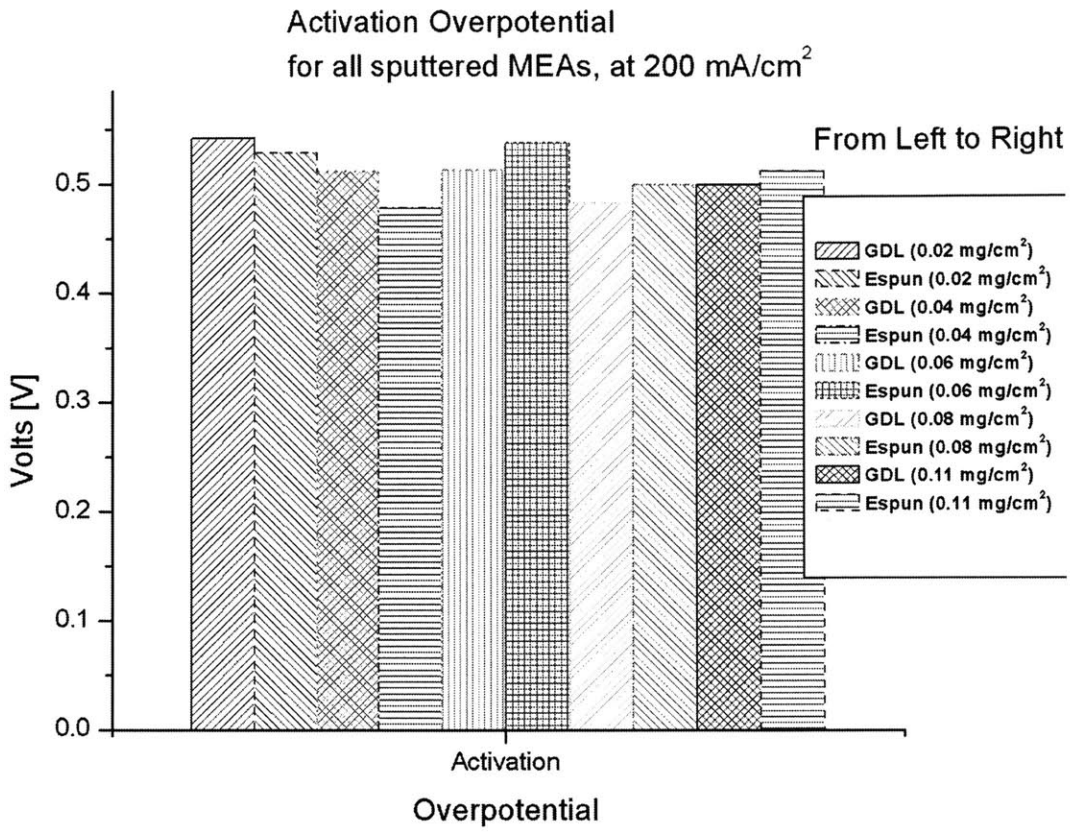

Figure 45. Activation overpotential for all sputtered samples tested, at 200 mA/cm^2. All data collected at 80 °C, RH~100%, and atmospheric pressure.

There is no trend of interest in any of the other overpotentials in terms of overpotential vs. sputtering time or in terms of electrospun performance vs. GDL support performance.

Comparing Losses in Sputtered vs. Commercial E-TEK cathodes

For all the MEAs tested, the largest contribution to the voltage drop is clearly the activation overpotential (the difference between Vcorr6 and Vcorr5). Table 5 and Figure 46 reveal a large difference in activation overpotentials between the E-TEK and sputtered samples (0.315 V and 0.478-0.537 V, respectively). This difference of ~0.2 V is understandable. The actual formula for the overpotential associated with kinetics (ie. encompassing both the Tafel and activation overpotentials of this method, and the difference between Vcorr6 and Vcorr4) is given by [10]:

$$\eta_{ORR} = TS \times \log\left[\frac{i}{RF \times i_0}\right], \tag{5.11}$$

where TS is the Tafel slope, i is the current density, i_0 is the exchange current density (in mA/cm^2_{Pt}), and RF is the roughness factor which expresses the amount of platinum surface area in the electrode (in $cm^2_{Pt}/cm^2_{electrode}$). The roughness factor for the sputtered samples is roughly 10 (see Section 4.2), while for the E-TEK sample it can be estimated using:

$$10 \times L_{Cathode} \times ECA, \tag{5.12}$$

where $L_{Cathode}$ is the platinum loading in mg/cm^2 and ECA is the electrochemical active area, as above, in m^2_{pt}/g_{Pt}. Assuming an ECA of 112 m^2/g (taken from the E-TEK website), and using the given loading of 0.5 mg/cm^2, we arrive at a roughness factor of 560 for the E-TEK electrode. Using an exchange current density of 6.7×10^{-9} A/cm^2_{Pt}, and using equation (5.11) we arrive at:

$$\eta_{ORR} = TS_{sputtered} \times \log\left|\frac{i}{6.7 \times 10^{-8}}\right| \tag{5.13a}$$

$$\eta_{ORR} = TS_{E-TEK} \times \log\left|\frac{i}{3.75\times10^{-6}}\right| \tag{5.13b}$$

At 200 mA/cm^2, these become:

$$\eta_{ORR} = TS_{sputtered} \times 6.47 \tag{5.14a}$$

$$\eta_{ORR} = TS_{E-TEK} \times 4.72\,. \tag{5.14b}$$

Since the electrospun electrodes experience concentration overpotentials even at the lowest currents, their (oxygen) Tafel slopes were ~120-140 mV/decade, even in the 10-100 mA/cm^2 range. If we add together the Tafel and activation overpotentials at 200 mA/cm^2 using this step-by-step method, the E-TEK sample has ~0.39 V of kinetic overpotential and the sputtered samples have ~0.59 V of kinetic overpotential. If the sputtered and E-TEK samples had the theoretical Tafel slopes of 70 mV/decade, it would result in a $\acute{\eta}_{ORR}$ of ~0.33 V for the E-TEK sample, which is close to the actual 0.39 V (and if the E-TEK electrode has less than 112 m^2/g, which is likely the case, it would be closer to 0.39 V). For the sputtered samples, using equation (5.14), the kinetic overpotential would be ~0.45 V. If the sputtered samples had Tafel slopes through the entire current regime back to the exchange current density of ~120-140 mV/decade, then the $\acute{\eta}_{ORR}$ would be ~0.77-0.9 V, which is larger than the actual kinetic losses. Thus, as would be expected, the concentration overpotential causes a double Tafel slope which begins at some current density below 10 mA/cm^2, but which does not begin at the exchange current density. In other words, the Tafel slope begins at the theoretical value, but switches to the double slope before the range of our measurements, which accounts for the kinetic losses of 0.59 V. To summarize, then, the difference in activation overpotential between the E-TEK and sputtered samples is due to both the reduced active

area of platinum in the sputtered sample and the electrode concentration overpotential distorting the measurement, even at 10 mA/cm^2, where it should be purely kinetically limited.

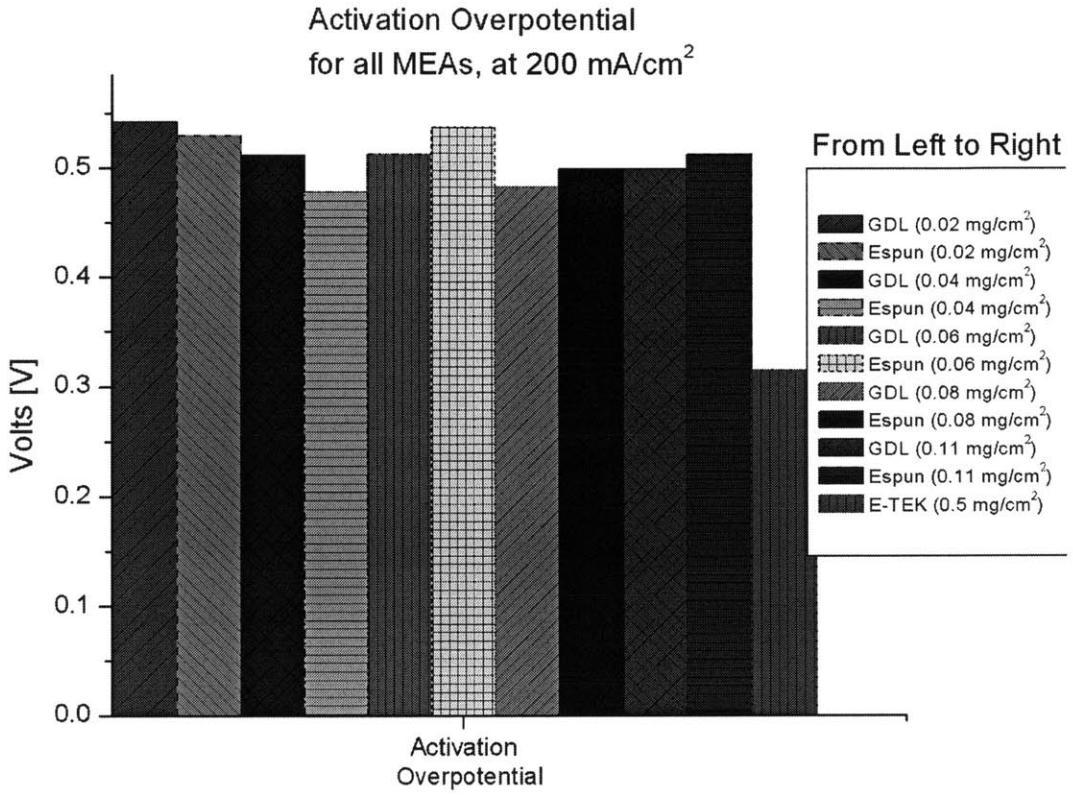

Figure 46. Activation overpotential for all samples tested, at 200 mA/cm^2. All data collected at 80 °C, RH~100%, and atmospheric pressure. Sputtering times (minutes) shown in parentheses. E-TEK GDE/GDE loaded with 0.5 mg Pt/cm^2.

The difference in the Tafel overpotentials are not significant, and it is due to the fact that an experimental oxygen Tafel slope was used in the E-TEK sample whereas the theoretical 70 mV/decade was used in the sputtered samples, as mentioned above. The ohmic overpotentials are similar between the E-TEK and sputtered samples as can be seen in Table 5. The differences in the non-electrode and electrode concentration

overpotentials are important to note, and are presented graphically in Figure 47 and Figure 48, respectively.

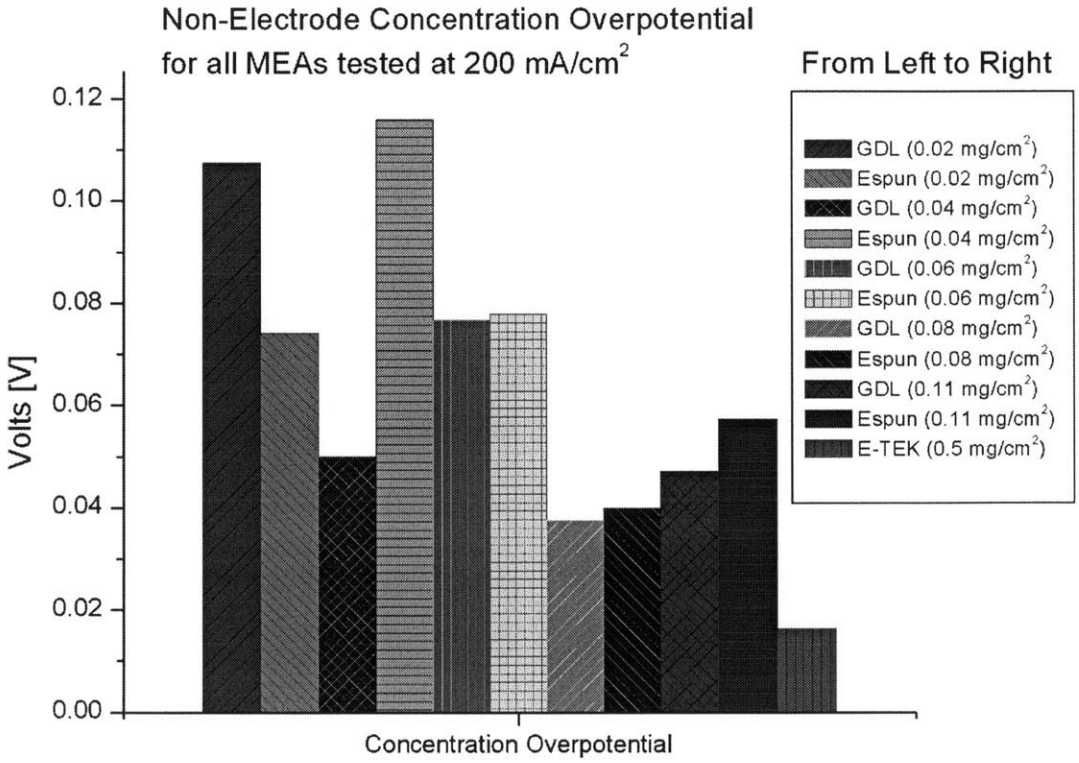

Figure 47. Non-electrode concentration overpotentials, at 200 mA/cm^2, for all samples tested. All data collected at 80 °C, RH~100%, and atmospheric pressure.

Clearly, the non-cathode concentration overpotentials are much larger in the sputtered samples than in the E-TEK sample. Recall from above that non-electrode concentration overpotential is due to resistance to oxygen transport in layers where oxygen is not consumed. This implies that there is something preventing the flow of reactant gas to the catalyst layer in the sputtered sample. This could be due to the Nafion ionomer solution application method used on the sputtered samples. For the sputtered

samples, the Nafion ionomer was simply pippeted onto the top of the platinum catalyst layer and allowed to seep through and dry. What probably occurred was that a good portion of the solution went right through the very porous electrospun layer and landed on top of the microporous layer of the gas diffusion layer, where the solvents evaporated leaving a thick Nafion film, which somewhat obstructed the flow of oxygen. This is supported by the EDAX line scan shown in Figures 20 and 21. For the samples sputtered on the GDLs, the same thing probably occurred: a buildup of Nafion on the microporous layer.

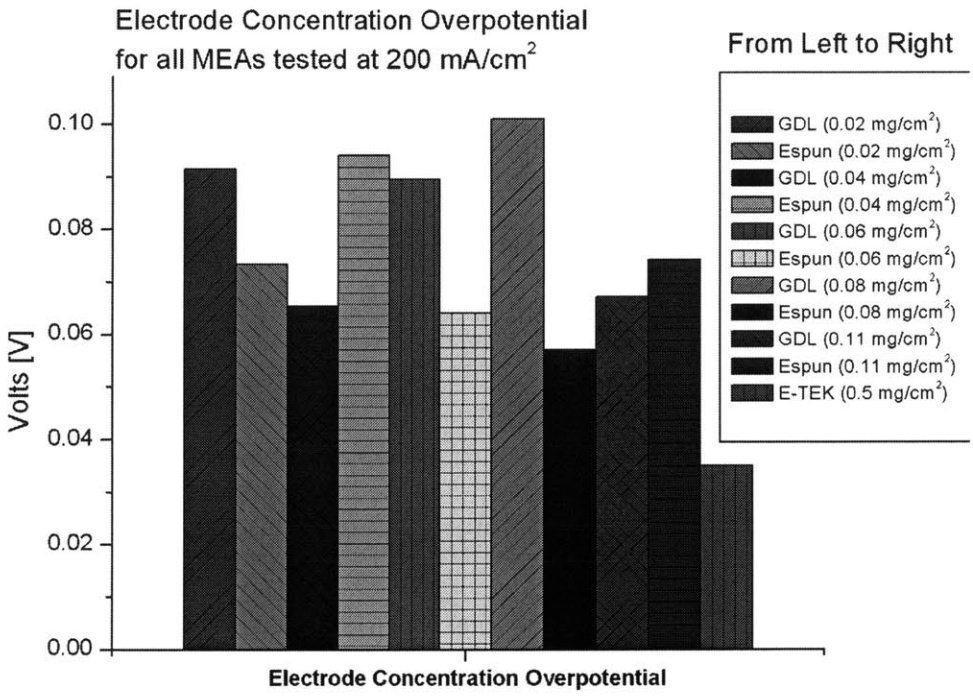

Figure 48. Electrode concentration overpotentials, at 200 mA/cm^2, for all samples tested. Sputtering times (minutes) shown in parentheses. All data collected at 80 °C, RH~100%, and atmospheric pressure.

The electrode concentration overpotential is also much larger for the sputtered samples than the E-TEK sample, which is shown in Figure 48. I speculate that the reason for this is that the platinum catalyst and Nafion ionomer are spread homogeneously throughout a 10-15 μm thick layer in the E-TEK samples, whereas in the sputtered samples, the platinum is concentrated in a thin (1-2 μm) layer near the membrane. Therefore, oxygen transport in the sputtered platinum layer may be significantly impeded if the platinum is largely stuck within the membrane itself. This makes sense given the nature of sputtered platinum: it is located in a thin region (<3 μm) adjacent to the membrane. This is confirmed in Figure 14, Figure 20 and Figure 21 above. For sputtered GDLs, the platinum has been shown to be confined to a 2 μm layer [29]. Thus it is likely that the oxygen molecules are impeded in reaching the platinum catalyst even at the lowest current densities.

6. Conclusions

The objective of this work was threefold: to fabricate and evaluate the performance of electrospun carbon nanofiber layers as catalyst supports for PEMFCs, to examine the sputtering method as a technique for platinum deposition in PEMFCs, and to examine the effect of sputtering time on ORR performance. From the results presented above, it seems that electrospun carbon nanofiber layers are adequate as catalyst supports in PEMFCs, since their performance is on par with that of the commercial GDL supports, but their implementation in membrane electrode assemblies will require optimizing the process of Nafion impregnation and other structural considerations. The sputtering method, however, is probably not a good method for catalyst deposition in PEMFCs based on the data presented in this work. Increasing the sputtering time does increase the fuel cell performance up to the loadings tested here (0.1 mg/cm^2), and the effect of increased loading on ORR kinetics is not conclusive, although the specific activity seems to increase with sputtering time.

Electrospinning of carbon nanofiber mats with diameters of 200 nm was successfully carried out. The main parameters that were critical in fabricating these thinner fibers are thought to be flow rate (~0.4 mL/hr) and plate to plate distance (~21cm), and to a lesser degree, polymer concentration (~9% PAN). Additionally, a smaller nozzle was used than in the previous work on fibers with embedded palladium particles. Although electrospinning is not totally predictable or repeatable, it is thought that these parameters were important in maintaining diameters of 200nm.

These fibers were sputtered with platinum for various sputtering times between 45 seconds and 8 minutes. The sputtering times were varied in order to evaluate the effect

that loading has on the particle size, the electrochemical active area, and on the oxygen reduction kinetics.

SEM images confirmed that the electrospun fibers had diameters smaller than or equal to 200 nm, and were nearly spindle free. Images taken with the backscattered electron detector and EDS data helped to determine the location of platinum in the electrode and in the cross-section of an MEA. Cross-section images taken in wet-mode revealed that the electrospun electrodes were not as robust as the commercial thin film electrodes from E-TEK when assembled as an MEA.

TEM images were used to examine the particle sizes of the samples sputtered for different amounts of time. It was found that the average diameter increases with sputtering time, from 2.05 nm at 45 seconds to 7.25 nm at 8 minutes, and the standard deviation of the distribution also seems to increase. It seemed that the platinum followed an island growth mechanism, with many irregularly shaped particles. It is also thought that beyond a sputtering time of 45 s, the fibers are covered with a thin film of platinum, on top of which the particles form.

Cyclic voltammetry and RDE were used to evaluate the performance of electrospun samples with different platinum loadings in terms of their electrochemical active area and their oxygen reduction performance. Active platinum area increased with sputtering time and the active area per mass of platinum decreased, in accordance with expectations. The numeric values for the electrochemical active area agreed with those in the literature for sputtered platinum, but differ from the theoretical amounts based on particle size data from the TEM. This is thought to be due to the thin film of platinum covering the fibers. Oxygen reduction activity on a mass basis decreases with loading, as

expected, and the specific activity increases with loading (with particle size). Tafel slopes are close to the theoretical values at low overpotentials.

Fuel cell testing revealed several important conclusions. Electrospun supports for sputtered platinum catalyst performed on par with commercial gas diffusion layer supports. There was no absolute trend of the fuel cell performance (ie. power density or voltage at a given current density) with the sputtering time, but overall, longer sputtering times performed better. None of the sputtered electrodes performed as well as the commercial E-TEK electrode, and in fact, the best sputtered electrode performed only 33% as well as the E-TEK electrode using an H_2/O_2 feed.

The activation overpotential for the sputtered samples was significantly more than the commercial E-TEK sample. This is due to the fact that the E-TEK sample has about 50 times the surface area of platinum as does the sputtered sample, and because the sputtered samples had concentration overpotentials at even the lowest current densities, which masquerade as activation overpotentials.

The cathode and non-cathode ohmic overpotentials are pretty similar for the sputtered and E-TEK cathodes. The sputtered samples have the platinum in close contact with the Nafion membrane, and therefore there is little ionic resistance in the cathode layer, which is the dominant contribution to the cathode ohmic overpotential. The non-cathode ohmic losses are similar because they depend mostly on the membrane hydration.

The non-electrode concentration overpotential was significantly higher for the sputtered samples than for the E-TEK sample. This is thought to be due to the Nafion ionomer pooling on the microporous layer and impeding the diffusion of molecular oxygen to the electrode.

Concentration losses within the electrode were also higher for the sputtered samples, and caused a double Tafel slope at even the lowest current densities. This may be due to the fact that the sputtered catalyst is located so near to the membrane, and exclusively on the side facing the membrane. Therefore, when the MEA is hot-pressed, the catalyst particles may be stuck within the thick membrane and the diffusion of oxygen to the platinum is very difficult.

7. Perspectives

As supports for sputtered platinum in PEMFCs, electrospun carbon nanofiber layers perform as well as commercial gas diffusion layers. As a technique for manufacturing PEMFC cathodes, sputtering does not seem to be very promising, given the low platinum surface area inherent in this method and the poor performance observed in these experiments. If the electrospun layers had platinum deposited by chemical deposition and were able to achieve the small particle size, good dispersion and high loading and Pt/C ratio, their performance might be as good as commercial thin film catalyst layers. This would require the electrospun fibers to have surface areas similar to carbon blacks; in other words, the fiber diameters would have to be reduced. Even granted that, this is not an easy assumption to make, since the electrospun fibers are in the form of a mat, not a powder, and the chemical deposition methods are typically employed using dispersed carbon particles. Another requirement would be to find a method of optimizing the Nafion distribution in the solid (non-powder) electrospun layer, which is more difficult than it is for Pt/C particles, which can simply be made into a homogeneous mixture of platinum, carbon and Nafion and painted or sprayed on the GDL. If these things were to be accomplished, the performance of the electrospun support could equal that of the carbon black supports. The advantage for electrospinning then might be in the manufacturing, especially if it were somehow possible to electrospin with the catalyst in the spinning solution without the problems mentioned in the introduction. Obviously, a cost analysis would have to be done, and would have to take into consideration the fact that carbon black used in commercial catalysts is cheaper than the polyacrylonitrile used in electrospinning.

1. http://www.eia.doe.gov/oiaf/aeo/pdf/overview.pdf. 2006 [cited; Available from: http://www.eia.doe.gov/emeu/international/crude2.html.
2. http://www.eia.doe.gov/oiaf/aeo/pdf/overview.pdf. *Annual Energy Outlook 2006.* 2006 [cited; Available from: http://www.eia.doe.gov/oiaf/aeo/pdf/overview.pdf.
3. Ballard Power Systems, *http://www.ballard.com/be_informed/fuel_cell_technology/roadmap*. 2006
4. Litster, S. and G. McLean, *PEM fuel cell electrodes.* Journal of Power Sources, 2004. **130**(1-2): p. 61-76.
5. Larminie, J.D., Andrew, *Fuel Cell Systems Explained.* 2 ed. 2003: John Wiley & Sons.
6. Allen J. Bard, L.R.F., *Electrochemical Methods: Fundamentals and Applications.* 2 ed. 2001: John Wiley and Sons.
7. Ryan O'Hayre, S.-W.C., Whitney Colella, Fritz B. Prinz, *Fuel Cell Fundamentals.* 2006: John Wiley and Sons.
8. Department of Industrial Engineering - University of Perugia, webpage, *Fuel Cell Performances.*
9. Kinoshita, K., *Electrochemical Oxygen Technology.* 1992: John wiley and Sons, INC.
10. Gasteiger, H.A., J.E. Panels, and S.G. Yan, *Dependence of PEM fuel cell performance on catalyst loading.* Journal of Power Sources, 2004. **127**(1-2): p. 162-171.
11. Rho, Y.W., et al., *Mass-Transport Phenomena in Proton-Exchange Membrane Fuel-Cells Using O2/He, O2/Ar, and O2/N2 Mixtures .1. Experimental-Analysis.* Journal of the Electrochemical Society, 1994. **141**(8): p. 2084-2088.
12. Williams, M.V., H.R. Kunz, and J.M. Fenton, *Analysis of polarization curves to evaluate polarization sources in hydrogen/air PEM fuel cells.* Journal of the Electrochemical Society, 2005. **152**(3): p. A635-A644.
13. Reneker, D.H. and I. Chun, *Nanometre diameter fibres of polymer, produced by electrospinning.* Nanotechnology, 1996. **7**(3): p. 216-223.
14. Shin, Y.M., et al., *Experimental characterization of electrospinning: the electrically forced jet and instabilities.* Polymer, 2001. **42**(25): p. 09955-09967.
15. Megelski, S., et al., *Micro- and nanostructured surface morphology on electrospun polymer fibers.* Macromolecules, 2002. **35**(22): p. 8456-8466.
16. Demir, M.M., et al., *Palladium nanoparticles by electrospinning from poly(acrylonitrile-co-acrylic acid)-PdCl2 solutions. Relations between preparation conditions, particle size, and catalytic activity.* Macromolecules, 2004. **37**(5): p. 1787-1792.
17. Sun, Z.C., et al., *Compound core-shell polymer nanofibers by co-electrospinning.* Advanced Materials, 2003. **15**(22): p. 1929-+.
18. Loscertales, I.G., et al., *Electrically forced coaxial nanojets for one-step hollow nanofiber design.* Journal of the American Chemical Society, 2004. **126**(17): p. 5376-5377.
19. Dai, H.Q., et al., *A novel method for preparing ultra-fine alumina-borate oxide fibres via an electrospinning technique.* Nanotechnology, 2002. **13**(5): p. 674-677.
20. Larsen, G., et al., *A method for making inorganic and hybrid (organic/inorganic) fibers and vesicles with diameters in the submicrometer and micrometer range via*

sol-gel chemistry and electrically forced liquid jets. Journal of the American Chemical Society, 2003. **125**(5): p. 1154-1155.
21. Li, D., Y.L. Wang, and Y.N. Xia, *Electrospinning of polymeric and ceramic nanofibers as uniaxially aligned arrays.* Nano Letters, 2003. **3**(8): p. 1167-1171.
22. Li, D., Y.L. Wang, and Y.N. Xia, *Electrospinning nanofibers as uniaxially aligned arrays and layer-by-layer stacked films.* Advanced Materials, 2004. **16**(4): p. 361-366.
23. Gangeri, A., et al., *Electrocatalytic performances of nanostructured platinum-carbon materials.* Catalysis Today, 2005. **102**: p. 50-57.
24. Bessel, C.A., et al., *Graphite nanofibers as an electrode for fuel cell applications.* Journal of Physical Chemistry B, 2001. **105**(6): p. 1115-1118.
25. Lee, K., et al., *Progress in the synthesis of carbon nanotube- and nanofiber-supported Pt electrocatalysts for PEM fuel cell catalysis.* Journal of Applied Electrochemistry, 2006. **36**(5): p. 507-522.
26. Chen, C.C., et al., *Growth and characteristics of carbon nanotubes on carbon cloth as electrodes.* Diamond and Related Materials, 2005. **14**(3-7): p. 770-773.
27. Gasteiger, H.A., et al., *Activity benchmarks and requirements for Pt, Pt-alloy, and non-Pt oxygen reduction catalysts for PEMFCs.* Applied Catalysis B-Environmental, 2005. **56**(1-2): p. 9-35.
28. Gruber, D., et al., *Sputter-deposited ultra-low catalyst loadings for PEM fuel cells.* Journal of Power Sources, 2005. **150**: p. 67-72.
29. Brault, P., et al., *Plasma sputtering deposition of platinum into porous fuel cell electrodes.* Journal of Physics D-Applied Physics, 2004. **37**(24): p. 3419-3423.
30. Haug, A.T., et al., *Increasing proton exchange membrane fuel cell catalyst effectiveness through sputter deposition.* Journal of the Electrochemical Society, 2002. **149**(3): p. A280-A287.
31. Cha, S.Y. and W.M. Lee, *Performance of proton exchange membrane fuel cell electrodes prepared by direct deposition of ultrathin platinum on the membrane surface.* Journal of the Electrochemical Society, 1999. **146**(11): p. 4055-4060.
32. O'Hayre, R., et al., *A sharp peak in the performance of sputtered platinum fuel cells at ultra-low platinum loading.* Journal of Power Sources, 2002. **109**(2): p. 483-493.
33. Ferreira, P.J., et al., *Instability of Pt/C electrocatalysts in proton exchange membrane fuel cells - A mechanistic investigation.* Journal of the Electrochemical Society, 2005. **152**(11): p. A2256-A2271.
34. Perry, M.L., J. Newman, and E.J. Cairns, *Mass transport in gas-diffusion electrodes: A diagnostic tool for fuel-cell cathodes.* Journal of the Electrochemical Society, 1998. **145**(1): p. 5-15.
35. Gasteiger, T.J.S.a.H.A., *Rotating thin-film method for supported catalysts*, in *Handbook of Fuel Cells*. 2003, John wiley and Sons.
36. Kurpiewski, J.P., *Electrospun Carbon Nanofiber Electrodes Decorated with Palladium Metal Nanoparticles: Fabrication and Characterization*, in *Mechanical Engineering*. 2005, M.I.T.: Cambridge.
37. Y.-S. Hsu, C.-S.H.a.Y.-C.C. in *Proceedings of the Third International Fuel Cell Conference* 1999. Nagoya, Japan

38. Kocha, S.S., *Ch. 46 Principles of MEA Preparation*, in *Handbook of Fuel Cells*, H.G. Wolf Vielstich, Arnold Lamm, Editor. 2003, John Wiley and Sons, Inc.
39. Hombrados, A.G., et al., *Symmetrical electrode mode for PEMFC characterisation using impedance spectroscopy.* Journal of Power Sources, 2005. **151**: p. 25-31.
40. Reneker, D.H., et al., *Bending instability of electrically charged liquid jets of polymer solutions in electrospinning.* Journal of Applied Physics, 2000. **87**(9): p. 4531-4547.
41. Theron, S.A., E. Zussman, and A.L. Yarin, *Experimental investigation of the governing parameters in the electrospinning of polymer solutions.* Polymer, 2004. **45**(6): p. 2017-2030.
42. Fridrikh, S.V., et al., *Controlling the fiber diameter during electrospinning.* Physical Review Letters, 2003. **90**(14).
43. Li, D. and Y.N. Xia, *Electrospinning of nanofibers: Reinventing the wheel?* Advanced Materials, 2004. **16**(14): p. 1151-1170.
44. Hirano, S., J. Kim, and S. Srinivasan, *High performance proton exchange membrane fuel cells with sputter-deposited Pt layer electrodes.* Electrochimica Acta, 1997. **42**(10): p. 1587-1593.
45. Maruyama, J., et al., *Influence of activated carbon pore structure on oxygen reduction at catalyst layers supported on rotating disk electrodes.* Carbon, 2004. **42**(15): p. 3115-3121.
46. Poirier, J.A. and G.E. Stoner, *Microstructural Effects on Electrocatalytic Oxygen Reduction Activity of Nano-Grained Thin-Film Platinum in Acid-Media.* Journal of the Electrochemical Society, 1994. **141**(2): p. 425-430.
47. Vielstich, W., *Cyclic voltammetry*, in *Handbook of Fuel Cells-Fundamentals, Technology and Applications*. 2003, John Wiley and Sons, Inc.
48. Markovic, N., H. Gasteiger, and P.N. Ross, *Kinetics of oxygen reduction on Pt(hkl) electrodes: Implications for the crystallite size effect with supported Pt electrocatalysts.* Journal of the Electrochemical Society, 1997. **144**(5): p. 1591-1597.
49. Peuckert, M., et al., *Oxygen Reduction on Small Supported Platinum Particles.* Journal of the Electrochemical Society, 1986. **133**(5): p. 944-947.
50. Maruyama, J. and I. Abe, *Cathodic oxygen reduction at the catalyst layer formed from Pt/carbon with adsorbed water.* Journal of Electroanalytical Chemistry, 2003. **545**: p. 109-115.
51. Kinoshita, K., *Particle Size Effects for Oxygen Reduction on Highly Dispersed Platinum in Acid Electrolytes.* J. Electrochem. Soc., 1990. **137**(3): p. 845-848.
52. Paulus, U.A., et al., *Oxygen reduction on a high-surface area Pt/Vulcan carbon catalyst: a thin-film rotating ring-disk electrode study.* Journal of Electroanalytical Chemistry, 2001. **495**(2): p. 134-145.
53. K.R. Cooper, M.S., *Electrical test methods for on-line fuel cell ohmic resistance measurement.* Journal of Power Sources, 2006.

Appendix A. TEM Image of Sample Sputtered for 45s

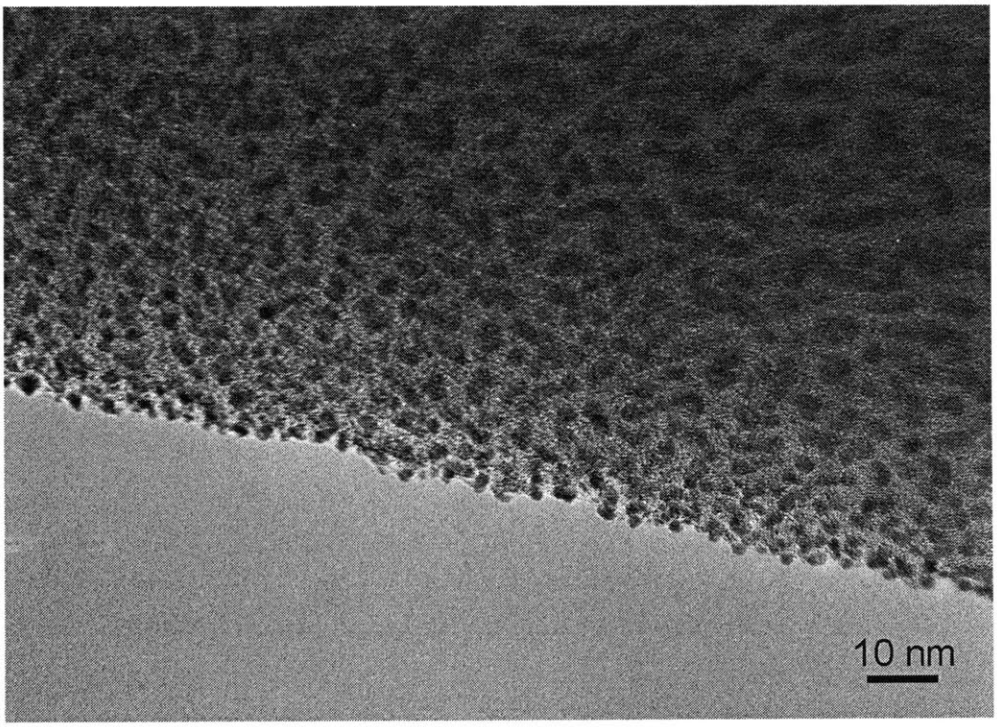

TEM image of sample sputtered for 45 s (0.01 mg Pt/cm^2), taken on the JEOL 2010 at 400,000x magnification, by Dr. Anthony Garratt-Reed.

The particle size distribution obtained in Section 3.3 for the sample sputtered for 45s was obtained from the image above. It can be clearly seen that for this sputtering time, the fiber is not yet covered with a thin layer of platinum.

Appendix B. Fuel Cell Performance Data

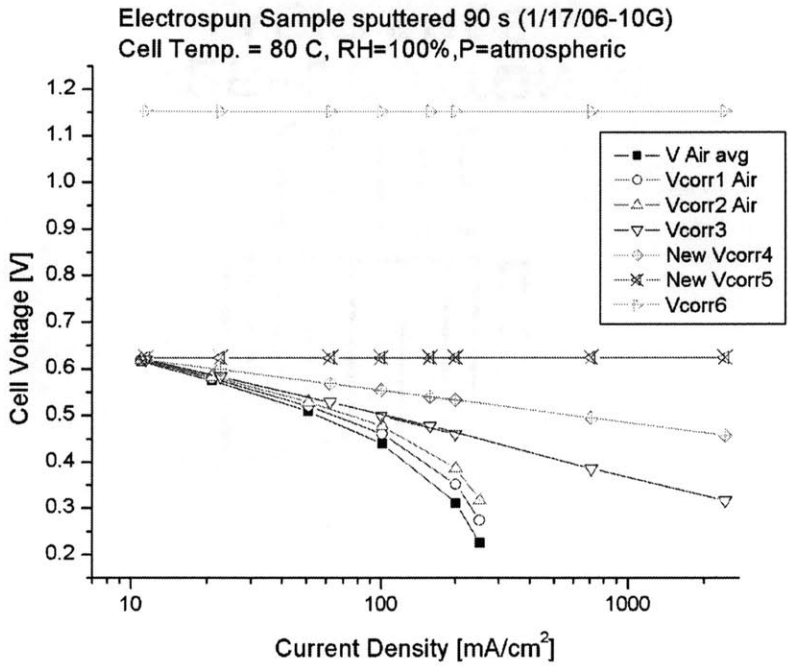

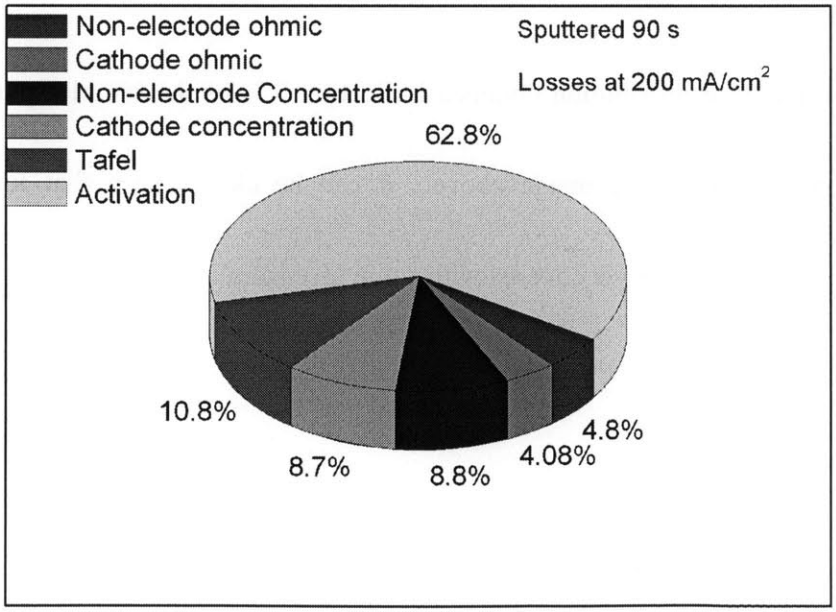

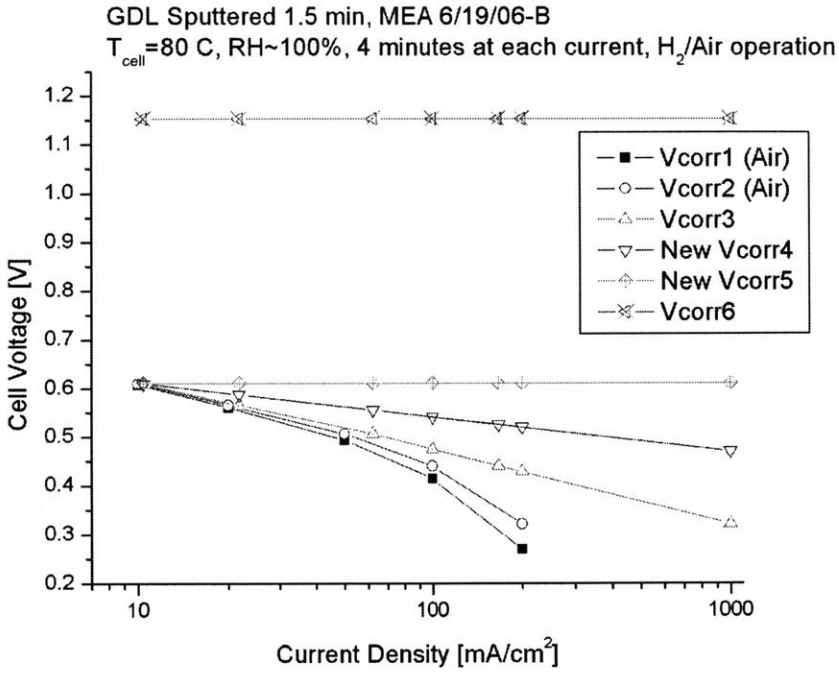
GDL Sputtered 1.5 min, MEA 6/19/06-B
T_cell=80 C, RH~100%, 4 minutes at each current, H2/Air operation
Cell Voltage [V]
Current Density [mA/cm2]
Vcorr1 (Air)
Vcorr2 (Air)
Vcorr3
New Vcorr4
New Vcorr5
Vcorr6

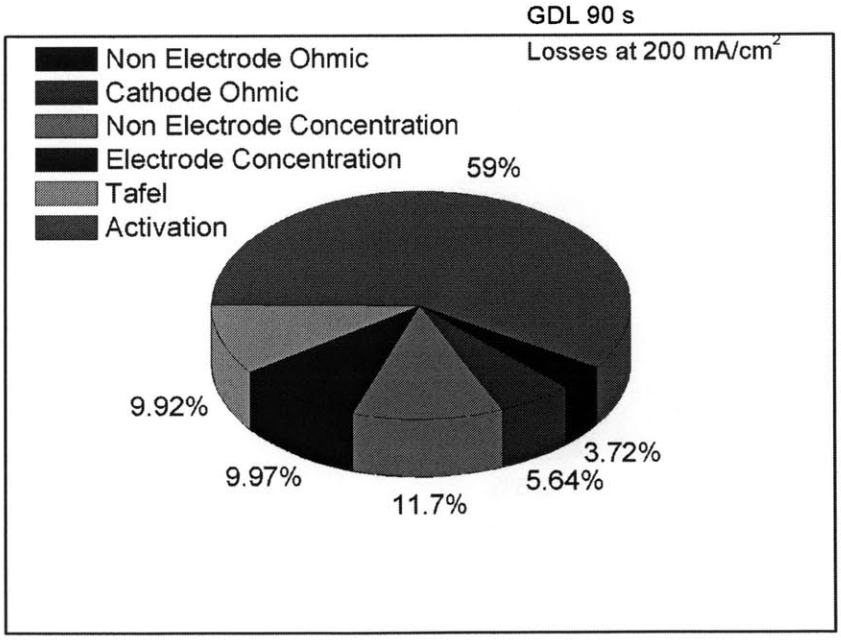
GDL 90 s
Losses at 200 mA/cm2
Non Electrode Ohmic
Cathode Ohmic
Non Electrode Concentration
Electrode Concentration
Tafel
Activation
59%
9.92%
9.97%
11.7%
5.64%
3.72%

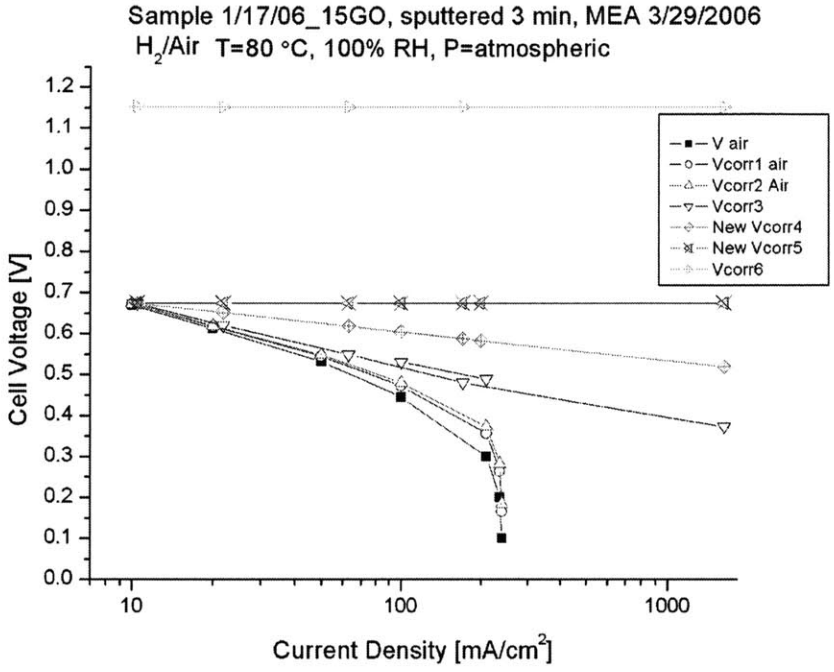

Sample 1/17/06_15GO sputtered 3 min

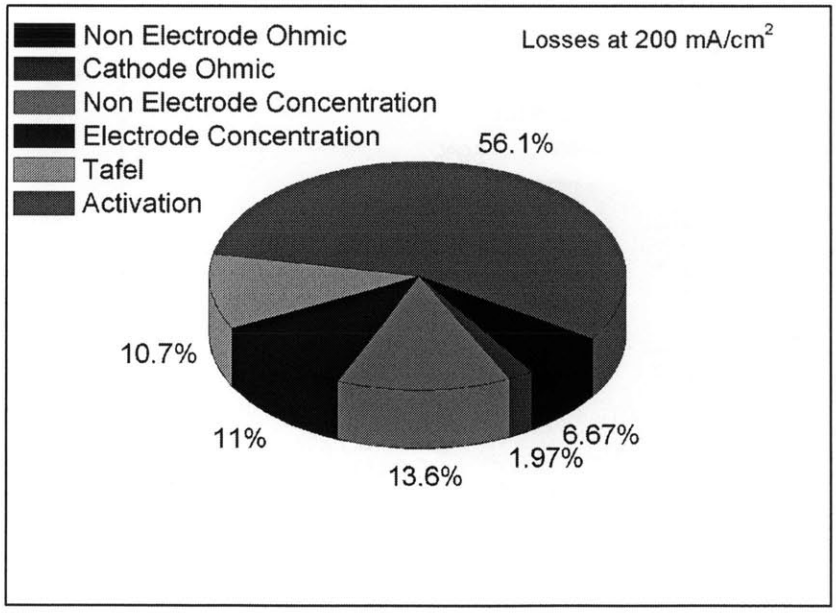

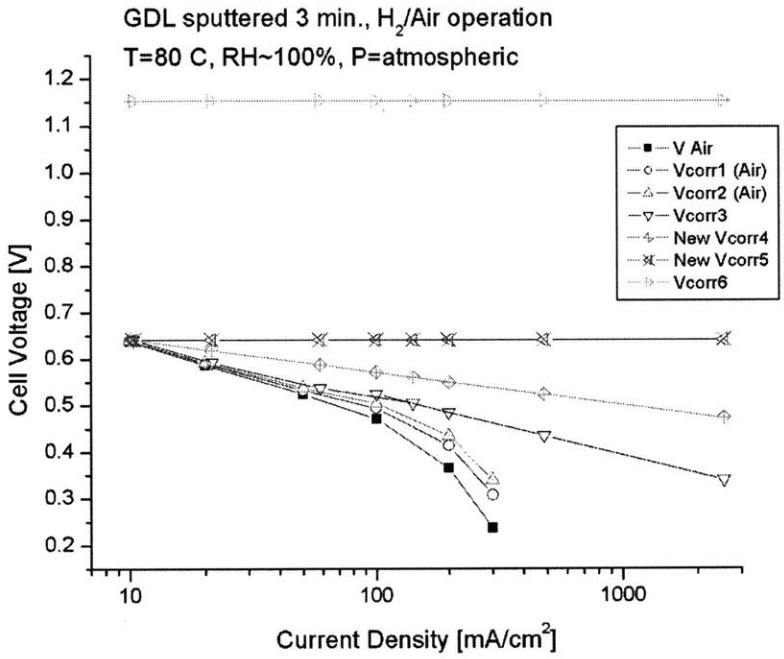
GDL sputtered 3 min., H_2/Air operation
T=80 C, RH~100%, P=atmospheric
Cell Voltage [V]
Current Density [mA/cm^2]
V Air
Vcorr1 (Air)
Vcorr2 (Air)
Vcorr3
New Vcorr4
New Vcorr5
Vcorr6

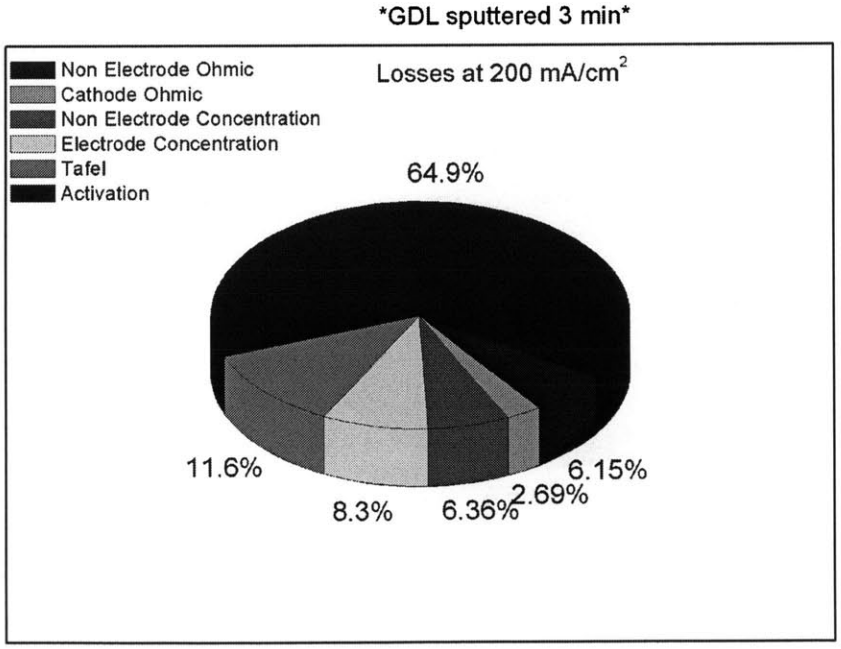
GDL sputtered 3 min
Losses at 200 mA/cm^2
Non Electrode Ohmic
Cathode Ohmic
Non Electrode Concentration
Electrode Concentration
Tafel
Activation
64.9%
11.6%
8.3%
6.36%
2.69%
6.15%

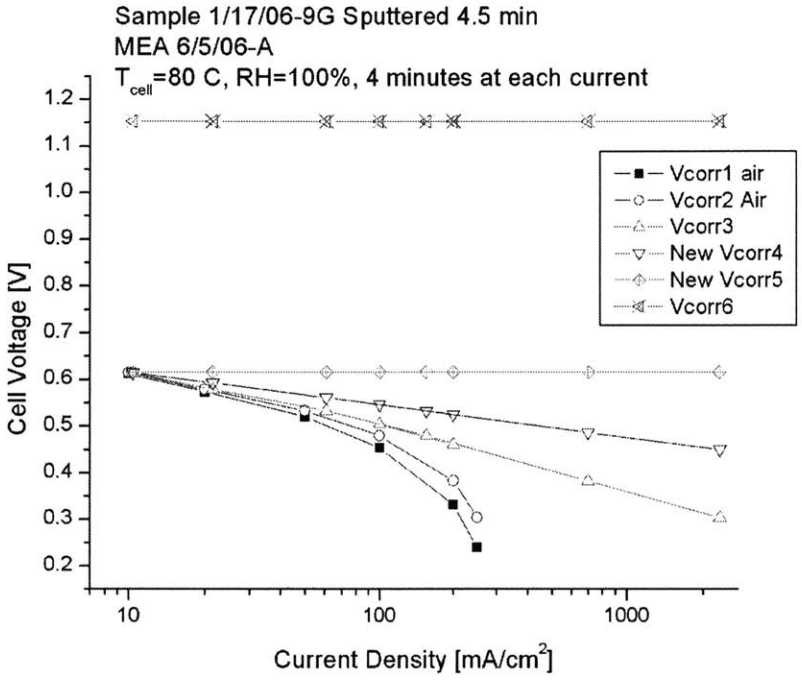
Sample 1/17/06-9G Sputtered 4.5 min
MEA 6/5/06-A
T_{cell}=80 C, RH=100%, 4 minutes at each current
Vcorr1 air
Vcorr2 Air
Vcorr3
New Vcorr4
New Vcorr5
Vcorr6
Cell Voltage [V]
1.2
1.1
1.0
0.9
0.8
0.7
0.6
0.5
0.4
0.3
0.2
10
100
1000
Current Density [mA/cm^2]

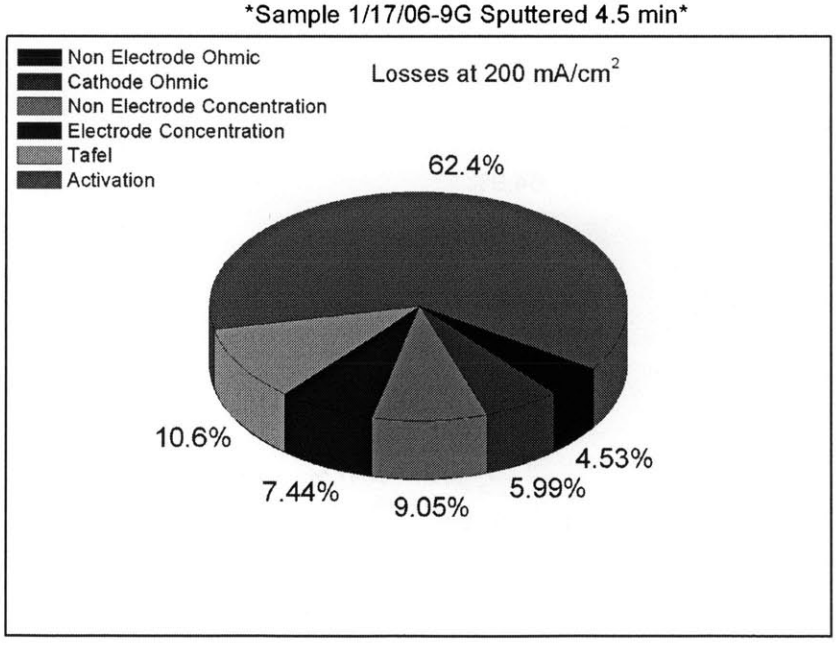
Sample 1/17/06-9G Sputtered 4.5 min
Non Electrode Ohmic
Cathode Ohmic
Non Electrode Concentration
Electrode Concentration
Tafel
Activation
Losses at 200 mA/cm^2
62.4%
10.6%
7.44%
9.05%
5.99%
4.53%

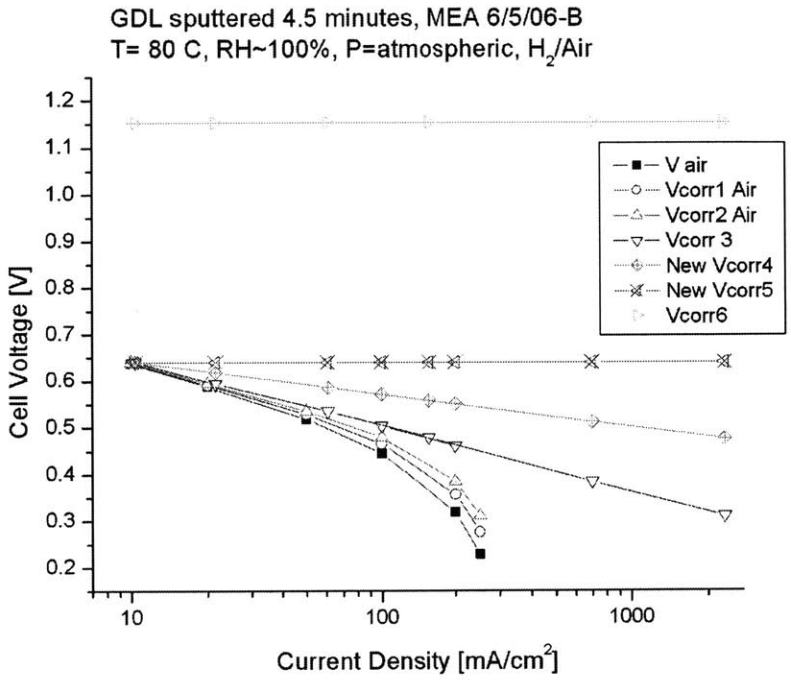
GDL sputtered 4.5 minutes, MEA 6/5/06-B
T= 80 C, RH~100%, P=atmospheric, H2/Air
Cell Voltage [V]
Current Density [mA/cm2]
V air
Vcorr1 Air
Vcorr2 Air
Vcorr 3
New Vcorr4
New Vcorr5
Vcorr6

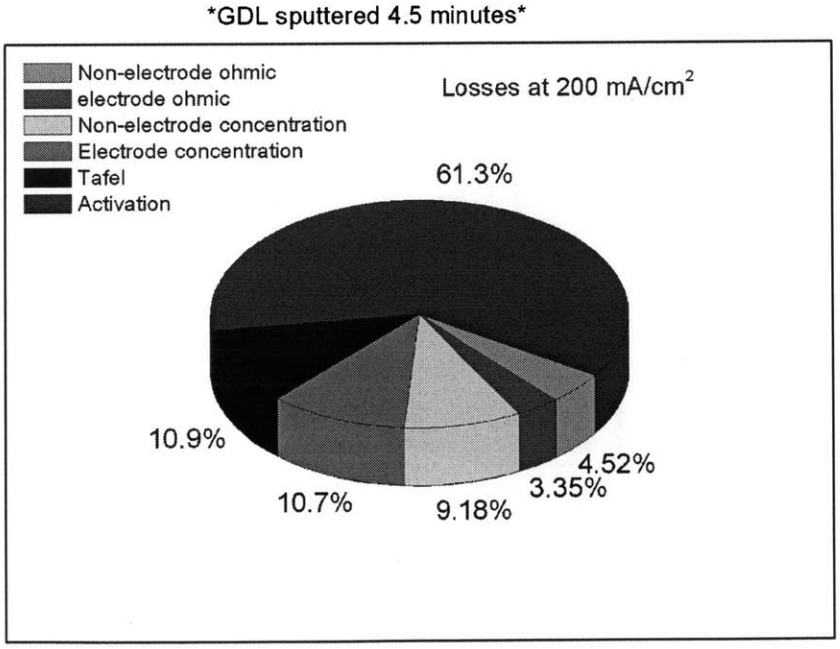
GDL sputtered 4.5 minutes
Non-electrode ohmic
electrode ohmic
Non-electrode concentration
Electrode concentration
Tafel
Activation
Losses at 200 mA/cm2
61.3%
10.9%
10.7%
9.18%
3.35%
4.52%

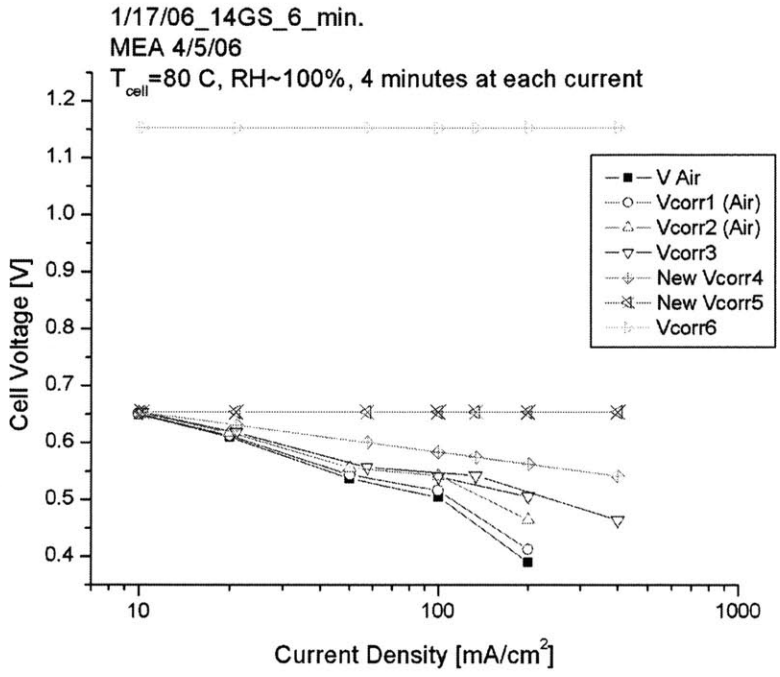
1/17/06_14GS_6_min.
MEA 4/5/06
T_{cell}=80 C, RH~100%, 4 minutes at each current
Cell Voltage [V]
Current Density [mA/cm^2]
V Air
Vcorr1 (Air)
Vcorr2 (Air)
Vcorr3
New Vcorr4
New Vcorr5
Vcorr6

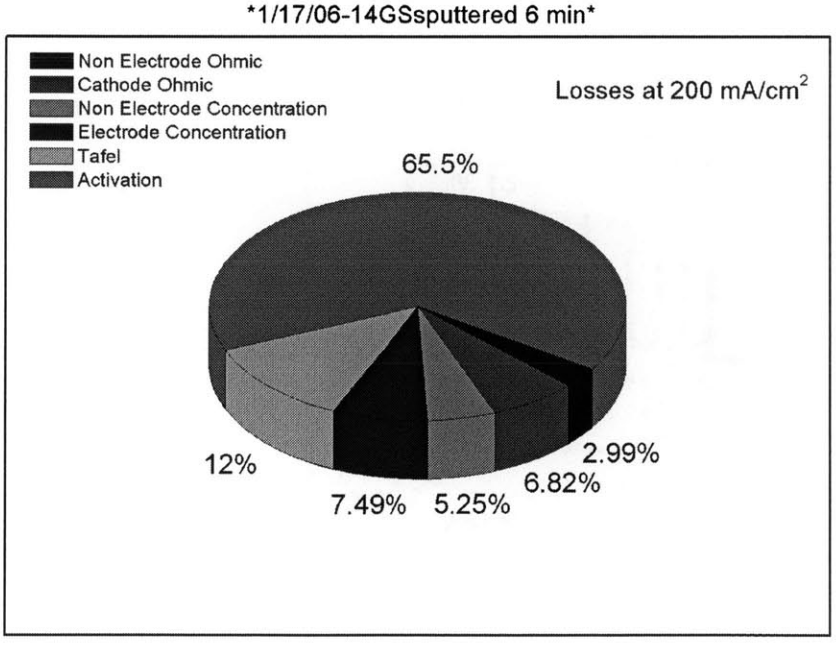
1/17/06-14GSsputtered 6 min
Non Electrode Ohmic
Cathode Ohmic
Non Electrode Concentration
Electrode Concentration
Tafel
Activation
Losses at 200 mA/cm^2
65.5%
12%
7.49%
5.25%
6.82%
2.99%

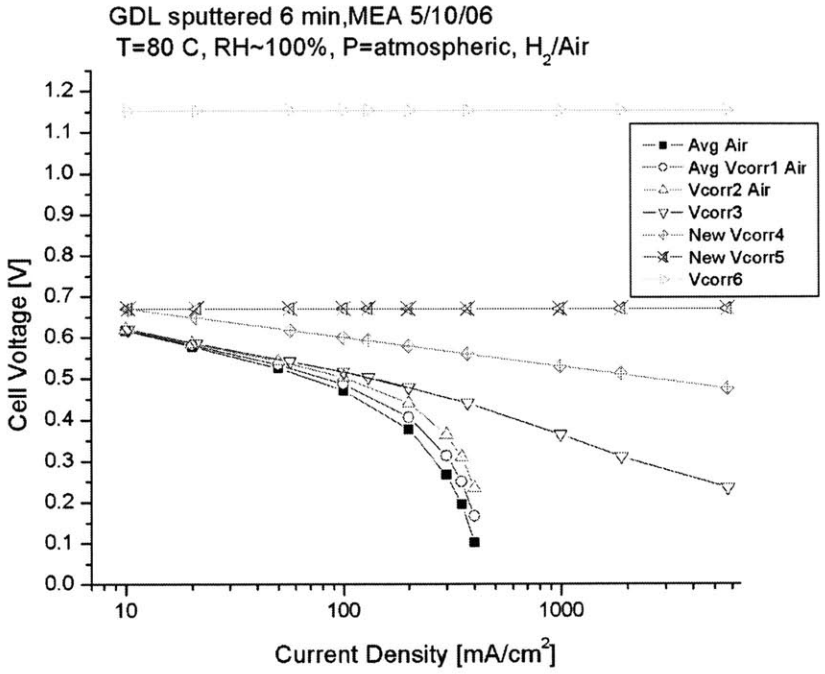

GDL sputtered 6 min.

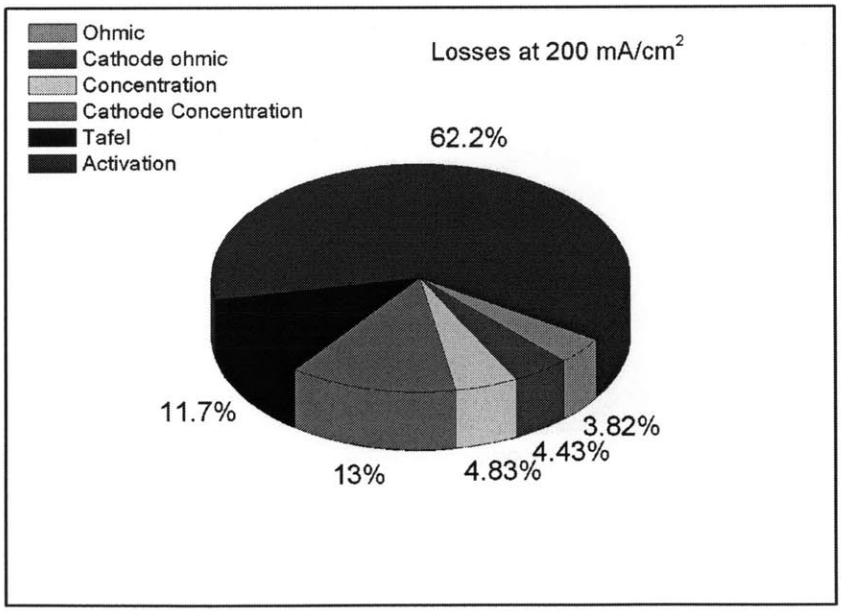

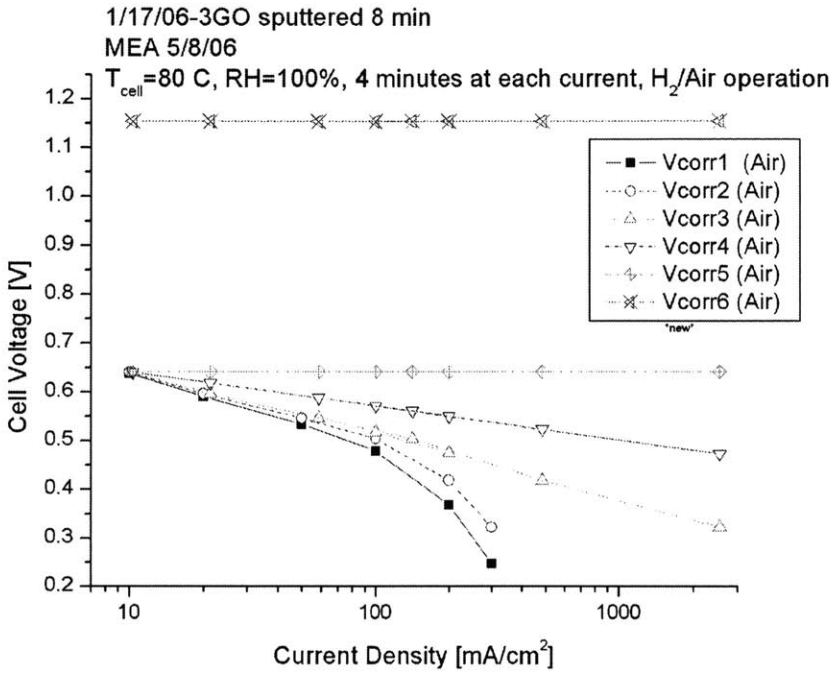
1/17/06-3GO sputtered 8 min
MEA 5/8/06
T_cell=80 C, RH=100%, 4 minutes at each current, H2/Air operation
Vcorr1 (Air)
Vcorr2 (Air)
Vcorr3 (Air)
Vcorr4 (Air)
Vcorr5 (Air)
Vcorr6 (Air)
'new'
Cell Voltage [V]
Current Density [mA/cm2]

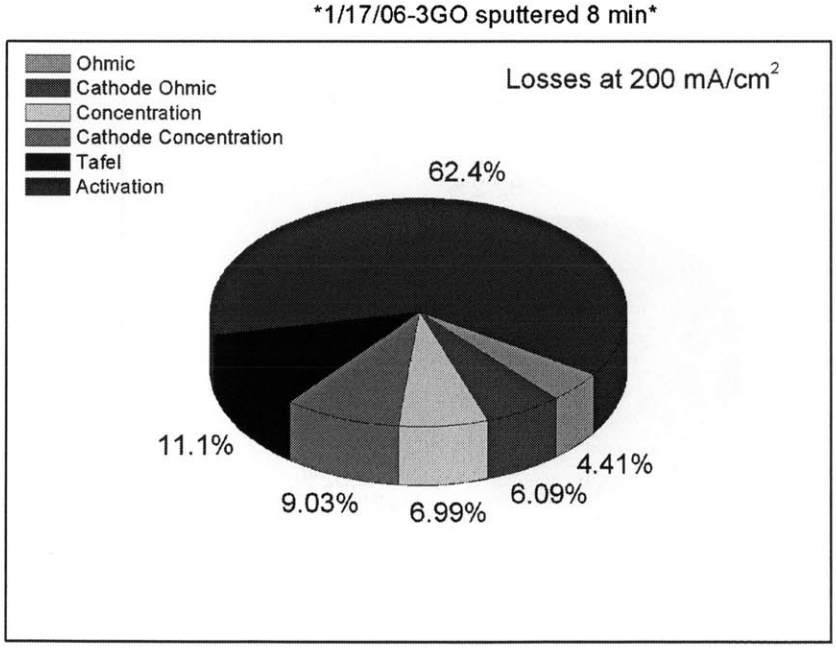
1/17/06-3GO sputtered 8 min
Ohmic
Cathode Ohmic
Concentration
Cathode Concentration
Tafel
Activation
Losses at 200 mA/cm2
62.4%
11.1%
9.03%
6.99%
6.09%
4.41%

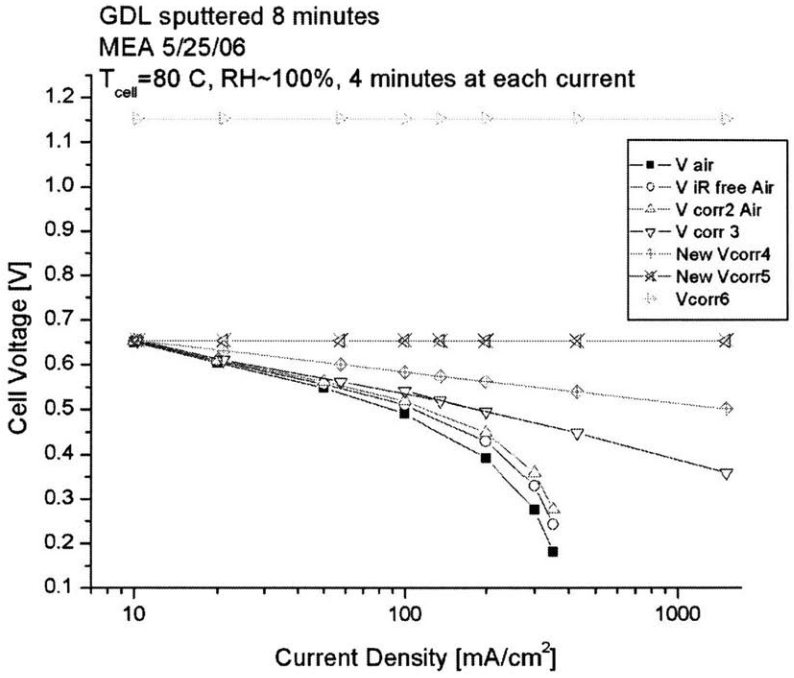

GDL sputtered 8 min.